

Effect of Particle Dynamics On Turbulence Measurements With The Laser Doppler Velocimeter

R. H. Nichols
Directorate of Propulsion
Turbine Engine Analysis

December 1986

Final Report for Period 30 June 1984 – 30 December 1985

Approved for public release; distribution is unlimited.

**ARNOLD ENGINEERING DEVELOPMENT CENTER
ARNOLD AIR FORCE STATION, TENNESSEE
AIR FORCE SYSTEMS COMMAND
UNITED STATES AIR FORCE**

NOTICES

When U. S. Government drawings, specifications, or other data are used for any purpose other than a definitely related Government procurement operation, the Government thereby incurs no responsibility nor any obligation whatsoever, and the fact that the Government may have formulated, furnished, or in any way supplied the said drawings, specifications, or other data, is not to be regarded by implication or otherwise, or in any manner licensing the holder or any other person or corporation, or conveying any rights or permission to manufacture, use, or sell any patented invention that may in any way be related thereto.

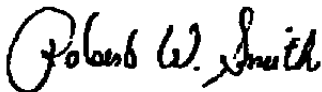
Qualified users may obtain copies of this report from the Defense Technical Information Center.

References to named commercial products in this report are not to be considered in any sense as an endorsement of the product by the United States Air Force or the Government.

This report has been reviewed by the Office of Public Affairs (PA) and is releasable to the National Technical Information Service (NTIS). At NTIS, it will be available to the general public, including foreign nations.

APPROVAL STATEMENT

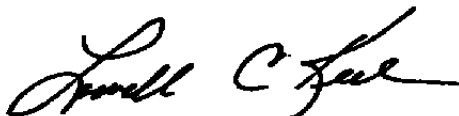
This report has been reviewed and approved.



ROBERT W. SMITH
Directorate of Technology
Deputy for Operations

Approved for publication:

FOR THE COMMANDER



LOWELL C. KEEL, Colonel, USAF
Director of Technology
Deputy for Operations

UNCLASSIFIED

SECURITY CLASSIFICATION OF THIS PAGE

REPORT DOCUMENTATION PAGE

1a REPORT SECURITY CLASSIFICATION UNCLASSIFIED		1b. RESTRICTIVE MARKINGS	
2a SECURITY CLASSIFICATION AUTHORITY		3 DISTRIBUTION/AVAILABILITY OF REPORT	
2b DECLASSIFICATION/DOWNGRADING SCHEDULE		Approved for public release; distribution is unlimited.	
4. PERFORMING ORGANIZATION REPORT NUMBER(S) AEDC-TR-86-41		5. MONITORING ORGANIZATION REPORT NUMBER(S)	
6a. NAME OF PERFORMING ORGANIZATION Arnold Engineering Development Center	6b. OFFICE SYMBOL (if applicable) DOT	7a NAME OF MONITORING ORGANIZATION	
6c. ADDRESS (City, State and ZIP Code) Air Force Systems Command Arnold Air Force Station, TN 37389-5000		7b. ADDRESS (City, State and ZIP Code)	
8a. NAME OF FUNDING/SPONSORING ORGANIZATION	8b. OFFICE SYMBOL (if applicable)	9. PROCUREMENT INSTRUMENT IDENTIFICATION NUMBER	
8c ADDRESS (City, State and ZIP Code)		10 SOURCE OF FUNDING NOS	
		PROGRAM ELEMENT NO	PROJECT NO
		TASK NO.	WORK UNIT NO
11 TITLE (Include Security Classification) SEE REVERSE OF THIS PAGE		65807F	
12. PERSONAL AUTHOR(S) Nichols, R. H., Directorate of Propulsion, Turbine Engine Analysis			
13a. TYPE OF REPORT Final	13b TIME COVERED FROM 6/30/84 TO 12/30/84	14 DATE OF REPORT (Yr., Mo., Day) December 1986	15 PAGE COUNT 96
16. SUPPLEMENTARY NOTATION Available in Defense Technical Information Center (DTIC)			
17. COSATI CODES		18. SUBJECT TERMS (Continue on reverse if necessary and identify by block number)	
FIELD	GROUP	SUB. GR	
20	04	velocity data turbulence measurements computer code laser velocimeter	
19. ABSTRACT (Continue on reverse if necessary and identify by block number) A numerical model for evaluating seed particle requirements for accurate turbulence measurements with the LV has been developed. A Monte Carlo turbulence model was developed which included an elementary description of the internal structure of an eddy. The model was applied to two simple turbulent flows, grid-generated turbulence and a subsonic axisymmetric jet, to evaluate particle response and to establish particle size requirements for accurate LV measurements in these flows. Large monodisperse particles were found to cause the turbulence quantities to be underestimated, leading to a requirement for very small particles for meaningful turbulence measurements with the LV. "Rule of thumb" criteria for particle size selection are developed.			
20. DISTRIBUTION/AVAILABILITY OF ABSTRACT UNCLASSIFIED/UNLIMITED <input type="checkbox"/> SAME AS RPT <input checked="" type="checkbox"/> DTIC USERS <input type="checkbox"/>		21 ABSTRACT SECURITY CLASSIFICATION UNCLASSIFIED	
22a. NAME OF RESPONSIBLE INDIVIDUAL W. O. Cole		22b TELEPHONE NUMBER (Include Area Code) (615) 454-7813	22c OFFICE SYMBOL DOS

UNCLASSIFIED

SECURITY CLASSIFICATION OF THIS PAGE

11. TITLE

Effect of Particle Dynamics on Turbulence Measurements with the Laser Doppler
Velocimeter

UNCLASSIFIED

SECURITY CLASSIFICATION OF THIS PAGE

PREFACE

The work reported was done at the Arnold Engineering Development Center (AEDC), Air Force Systems Command (AFSC), Arnold Air Force Station, Tennessee. The results were first published as a thesis by the author in fulfillment of requirements for a Doctor of Philosophy degree with a major in Aerospace Engineering from the University of Tennessee, Knoxville, Tennessee. The work was conducted during the period from June 30, 1984 to December 30, 1985, and the manuscript was submitted for publication October 16, 1986.

The author wishes to thank the United States Air Force for the opportunity to perform the work reported herein. Thanks are due to Dr. Keith Kushman, the author's supervisor, for his support and encouragement in the work and to Mr. Bob Bauer, Mr. Fred Heltsley, and Dr. Les Crosswy for their technical assistance and support in developing the ideas presented in this study. Appreciation is expressed to Dr. Frank Collins, who assisted in the preparation and review of the dissertation, and to Dr. Walter Frost, Dr. Trevor Moulden, Dr. Carroll Peters, and Dr. K. C. Reddy.

CONTENTS

	<u>Page</u>
1.0 INTRODUCTION	7
2.0 PARTICLE EQUATION OF MOTION	8
2.1 Basic Equation	8
2.2 Basset Term	10
2.3 Extension Beyond Stokes Flow	14
2.4 Numerical Solution of the Equation of Motion	18
3.0 PARTICLE SIZE DISTRIBUTION EFFECTS	20
3.1 Normal Shocks	21
3.2 Oblique Shocks	21
3.3 Laminar Supersonic Boundary Layer	22
3.4 Mean Flow Particle Size Requirements	22
4.0 TURBULENCE MODEL	23
5.0 PARTICLE RESPONSE TO TURBULENT FLOW FIELDS	27
5.1 Grid-Generated Turbulence	27
5.2 Subsonic Axisymmetric Jet	30
5.3 Multimodal Turbulence	33
6.0 APPROXIMATIONS FOR PARTICLE RESPONSE TO TURBULENCE	34
6.1 Spectral Cutoff Frequency Approximation	34
6.2 Simple Turbulence Model Approximation	35
6.3 Applications of the Approximation Techniques	36
7.0 SUMMARY	36
REFERENCES	38

ILLUSTRATIONS

<u>Figure</u>	<u>Page</u>
1. Particle Response to a Step Change in Fluid Velocity	41
2. Particle Response to a Sinusoidal Oscillation for $S = 1000$	45
3. Particle Response to a Sinusoidal Fluid Oscillation for $S = 2.65$	46
4. Standard Incompressible Drag Curve for a Sphere	47
5. Correction to Stokes Law for High Relative Reynolds Numbers	48
6. Empirical Correction for Subsonic Compressibility Effects	49

<u>Figure</u>	<u>Page</u>
7. Empirical Correction for Rarefaction Effects	50
8. Drag Coefficients for Nonspherical Particles	51
9. Variation of Sphere Drag Coefficient with Wall Temperature for $M_R = 2.0$	00
10. Increase in Stiffness of the Particle Equation of Motion with Decreasing Particle Diameter	00
11. Typical Velocity Correlogram for the LV	00
12. Theoretical Olive Oil Particle Response to a Cylinder Bow Shock at $M_\infty = 4.0$ and $Re_D = 10^5$	00
13. Measured LV Velocity Probability Distributions for a Cylinder Bow Shock at $M_\infty = 4.0$ and $Re_D = 10^5$	00
14. Particle Size Distribution for Olive Oil in a Collision Atomizer Measured with an ASAS-X® Aerosol Sampling Unit	00
15. Particle Relaxation Behind an Oblique Shock at $M_\infty = 2.2$ and $Re = 4.4 \times 10^6/M$	00
16. Particle Response to an Oblique Shock for $M_1 = 2.2$, $\theta = 40$ deg, $\delta = 14$ deg, and $Re = 4.4 \times 10^6/M$	00
17. Calculated Particle Velocities and Measured LV Velocity Distributions in the Laminar Boundary Layer on a 7-deg Half-Angle Cone at $M = 4$	00
18. Eulerian Representation of Turbulence	00
19. Lagrangian Turbulence Representation	00
20. Particle Interaction with a Turbulent Eddy - Effects of Time and Length Scales	00
21. Hot-Wire Measurements of Turbulent Energy Decay for the Experiment of Snyder and Lumley (Ref. 25)	00
22. Length Scales for the Experiment of Snyder and Lumley (Ref. 25)	00
23. Assumed Lagrangian Integral Time Scale for the Experiment of Snyder and Lumley (Ref. 25)	00
24. Experimental and Predicted Particle Dispersion for the Experiment of Snyder and Lumley (Ref. 25)	00
25. Experimental and Predicted Particle Turbulent Velocity Decay for the Experiment of Snyder and Lumley (Ref. 25)	00
26. Predicted Particle Response to Grid-Generated Turbulence	00
27. Product of the Stokes Number and the Turbulence Time Scale for Grid-Generated Turbulence for x/M of 80 and 124	00

<u>Figure</u>	<u>Page</u>
28. Flow Structure for a Simple Subsonic Jet	00
29. Decay of Centerline Axial Velocity for a Subsonic Jet	00
30. Radial Distribution of Axial Velocity	00
31. Radial Distribution of Radial Velocity	00
32. Radial Distribution of Turbulent Stresses	00
33. Centerline Distribution of Jet Turbulence Length Scales	00
34. Centerline Distribution of Jet Turbulence Integral Time Scale	00
35. Measured and Predicted Particle Velocities on the Jet Centerline for 20- μ m Fly-ash Particles	00
36. Measured and Predicted Particle Diffusivity on the Jet Centerline for 20- μ m Fly-ash Particles	00
37. Predicted Particle Response to Turbulence in a Subsonic Axisymmetric Jet	00
38. Velocity Correlograms for Water Particles in a Subsonic Axisymmetric Jet at $x/D = 12.0$, $r/D = 0.375$	00
39. Product of the Stokes Number and the Turbulence Time Scale for a Subsonic Axisymmetric Jet for x/D of 8.57 and 12.0	00
40. Approximations and Theoretical Particle Response for Grid-Generated Turbulence	00
41. Approximations and Theoretical Particle Response for a Subsonic Jet	00
 NOMENCLATURE	 00

1.0 INTRODUCTION

The evolution of nonintrusive flow diagnostic methods in the last few years has created powerful tools for gathering meaningful flow-field data in extremely complex flow fields. But, as with any measurement technique, care must be taken in defining the limitations and critical requirements for these techniques. This is especially true in the case of these nonintrusive techniques since there are often no means to verify measurements in the complex flow fields in which the techniques are being applied.

One of the most promising of these techniques is laser velocimetry (LV). The LV measures the velocity of small particles entrained in the flow field of interest. The fluid velocity and turbulent velocity correlations are then inferred from statistical analysis of these particle velocity measurements under the assumption that the particles exactly reproduce the motion of the fluid. This assumption needs to be carefully evaluated since it is fundamental to the application of the laser velocimeter.

Early development of the velocimeter seemed to have centered on the electronics and optics of the instrument. Particle dynamics was generally assumed to be a minor problem compared with the task of acquiring any data at all. Simple low-speed flow fields were used to verify the LV principle, and calculations using simple particle drag laws and simplified particle equations of motion were used to dispel concerns about particle dynamics effects. As the LV was graduated to more complex and higher speed flows, it became obvious that the assumed small particles were not following the fluid. This can be seen in the exit of a supersonic jet as described in Ref. 1. Results such as these have led to a more thorough evaluation of particle dynamics and particle generation in the LV community.

Most of the current particle dynamics studies are directed to the problem of determining an accurate mean flow velocity measurement. Very little has been or is being done to investigate particle response to the velocity fluctuations of a turbulent flow field. Hjelmfelt and Mockros (Ref. 2) performed a fairly simple analysis of particle response to a sinusoidally oscillating flow field. The solution is only of academic interest since turbulence consists of finite random eddies rather than continuously varying velocity oscillations. The solution is based on the questionable assumption that the solid particle always follows the same fluid particles; that is, there are no trajectory crossing effects. Sheun et al. in Ref. 3 modeled the turbulent field more accurately by using a Monte Carlo approach to reconstruct the randomness of turbulence and included trajectory crossing effects. This technique is adequate for large, heavy particles but lacks the detail in the turbulence model and in the particle equation of motion to adequately predict the motion of the small particles of interest in velocimetry applications. Ormancey and Martinon (Ref. 4) followed a similar approach to Shuen but included a more complete

model of a turbulent eddy and an improved equation of motion. This method fails to predict the motion of small, light particles in a turbulent flow, which possibly indicates some problems exist with his turbulence model. Since small, light particles that nearly reproduce the motion of the turbulent fluid are of principal interest in LV applications, improvements to these models are necessary before they are useful in evaluating particle dynamics limitation for LV measurements.

The objective of this effort is to develop the models necessary to determine particle requirements for obtaining turbulence measurements with the LV and to apply these models to some simple flow fields to evaluate particle response. The particle equation of motion is carefully evaluated in Section 2.0, and a computer code is developed to solve this equation. Using this code, the broadening of the velocity distribution attributable to a particle size distribution in the presence of a velocity gradient is discussed in Section 3.0. A Monte Carlo turbulence model is developed and coupled with the particle equation-of-motion solver from Section 2.0 in Section 4.0. This code is applied to two simple turbulent flow fields in Section 5.0 to evaluate the particle size requirements for turbulence measurements in these flows. Simple "rule of thumb" techniques for estimating particle size requirements for turbulence measurements with the LV are outlined in Section 6.0. Conclusions and recommendations are presented in Section 7.0.

2.0 PARTICLE EQUATION OF MOTION

There are a number of forms of the equation of motion of a small particle in a nonuniform flow field in the literature. All these equations are based on the equation of motion for a small sphere accelerating in a fluid at rest developed independently by Basset (Ref. 5), Boussinesq (Ref. 6), and Oseen (Ref. 7). Tchen (Ref. 8) generalized the solution for unsteady Stokes flow in a uniform fluid. Tchen then attempted, through heuristic argument, to extend the solution to nonuniform flows. It is assumed in all these equations that the particle is small enough to not disturb the flow field in which it is contained. This leads to the requirement that the particle loading be extremely low.

2.1 BASIC EQUATION

Tchen's equation may be written as

$$m_p \frac{dv_i}{dt} = -3\pi\mu d(v_i - u_i) + m_f \frac{Du_i}{Dt} - \frac{1}{2} m_f \frac{d}{dt} (v_i - u_i)$$

$$\begin{aligned}
& - \frac{3d^2}{2} \sqrt{\pi \rho_f \mu} \int_0^t \left[\frac{\frac{d}{d\tau} (v_i - u_i)}{\sqrt{t - \tau}} \right] d\tau \\
& - g_i (m_p - m_f)
\end{aligned} \tag{1}$$

where

$$\frac{Du_i}{Dt} = \frac{\partial u_i}{\partial t} + u_j \frac{\partial u_i}{\partial x_j} \tag{2}$$

and

$$\frac{du_i}{dt} = \frac{\partial u_i}{\partial t} + v_j \frac{\partial u_i}{\partial x_j} \tag{3}$$

and $v_i = v_i(t)$, $u_i = u_i(t)$. The terms on the right-hand side are the Stokes drag term, resultant pressure term, apparent mass, Basset history integral, and the gravitational force. The terms in Eqs. (2) and (3), which were not rigorously derived, are a source of controversy with this equation.

Several authors have attempted to improve upon Tchen's equation of motion for a sphere in a nonuniform Stokes flow, including Corrsin and Lumley (Ref. 9), Buevich (Ref. 10), Soo (Ref. 11), and Gitterman and Steinberg (Ref. 12). In a more recent effort by Maxey and Riley (Ref. 13), the equation of motion is derived using matched asymptotic expansion of the inner disturbance flow and the outer undisturbed flow. Their derivation also included the effects of velocity curvature on sphere drag. Maxey and Riley's equation may be written as

$$\begin{aligned}
& m_p \frac{dv_i}{dt} = -3\pi\mu d \left[v_i - u_i - \frac{d^2}{24} \nabla^2 u_i \mid \vec{Y}(t) \right] \\
& + m_f \frac{Du_i}{Dt} - \frac{m_f}{2} \frac{d}{dt} \left[v_i - u_i - \frac{d^2}{40} \nabla^2 u_i \mid \vec{Y}(t) \right] \\
& - \frac{3d^2}{2} \pi\mu \int_0^t \left\{ \frac{\frac{d}{d\tau} \left[v_i - u_i - \frac{d^2}{24} \nabla^2 u_i \mid \vec{Y}(t) \right]}{\sqrt{\pi\nu(t - \tau)}} \right\} d\tau
\end{aligned}$$

$$+ (m_p - m_f) g_i \quad (4)$$

where

$$\frac{Du_i}{dt} = \left(\frac{\partial u_i}{\partial t} + u_j \frac{\partial u_i}{\partial x_j} \right) \Big|_{\vec{x} = \vec{Y}(t)} \quad (5)$$

and

$$\frac{du_i}{dt} = \left(\frac{\partial u_i}{\partial t} + v_j \frac{\partial u_i}{\partial x_j} \right) \Big|_{\vec{x} = \vec{Y}(t)} \quad (6)$$

and $v_i = v_i(t)$, $u_i = [\vec{Y}(t), t]$. $\vec{Y}(t)$ is the particle position as a function of time in an inertial reference frame. Crudely evaluating the order-of-magnitude of the term in Eq. (1) or Eq. (4) relative to the left hand of the equation we have

Drag Force	$\sim 0 \left[\frac{18\nu}{d^2} \frac{\rho_f}{\rho_p} \right]$
Gravitational Force	$\sim 0 [1 - \rho_f/\rho_p]$
Pressure Force	$\sim [\rho_f/\rho_p]$
Apparent Mass Force	$\sim 0 [\rho_f/2\rho_p]$
Basset History Integral	$\sim 0 \left[\frac{3}{d} \frac{\rho_f}{\rho_p} \sqrt{\nu} \right]$

For the small and relatively heavy particles of interest in velocimetry, the drag term clearly dominates the equation of motion. As the density ratio decreases, other terms in the equation will become more important.

2.2 BASSET TERM

The Basset term is frequently omitted from solution schemes for the particle equation of motion, because it is not easy to deal with numerically. Order-of-magnitude analyses similar to those in the previous section are usually used to justify the omission of this term. These analyses fail to consider the magnitude of the integral term and should be viewed with caution if the magnitude of the integral is not known. The Basset term is essentially the time integral of the relative acceleration of the particle weighted by the square root of the time difference between the present time and the time at which the acceleration occurred. It is significant

when the particle relative acceleration is large compared to the particle relative velocity. It also becomes more significant as the particle density approaches, or is less than, the fluid density. Tchen's solution of the particle equation of motion, though not entirely accurate, offers the opportunity to evaluate when the Basset term becomes important. Two simple examples using Stokes drag law follow.

The solution to Tchen's equation of motion, including all terms, for a step change in fluid velocity from $u = b_0$ to $u = a_0$ is

$$v = e^{-kt} (b_0 - a_0) \left(\cos \omega t + \frac{k}{\omega} \sin \omega t \right) + a_0 \quad (7)$$

where

$$\omega^2 = \alpha^2 - k^2 = \alpha^2 \left(3\beta + \frac{9\beta^2}{4} \right) \quad (8)$$

$$k = \alpha(1 - 3/2 \beta) \quad (9)$$

$$\alpha = \frac{12\nu}{d^2} \beta \quad (10)$$

$$\beta = 3(2 \rho_p/\rho_f + 1)^{-1} \quad (11)$$

If the Basset term is ignored, the solution becomes

$$V = (b_0 - a_0)e^{-\alpha t} + a_0 \quad (12)$$

Solutions of these equations for density ratios S of 1000, 5, 1.75, and 1.0 are shown in Fig. 1. Fig. 1a shows that the Basset term is not negligible for $S = 1000$, which roughly corresponds to water particles in air. As S decreases, the solution becomes an exponentially damped oscillation (Fig. 1b), until $S = 1.75$ ($\beta = 0.6667$) at which time the damping disappears (Fig. 1c). As S is further decreased, the solution becomes an exponentially increasing oscillation (Fig. 1d).

In this example the Stokes drag law is used even though the particle relative Reynolds number greatly exceeds one. With Stokes law the drag is essentially zero for large particle Reynolds numbers. Because the drag is essentially zero, the Basset term dominates the equation of motion. In actuality the particle drag is not zero in the region with high particle relative Reynolds numbers when compressibility and inertia effects are included and when the effect of the Basset

term is reduced. Forney et al. (Ref. 14) demonstrated that the Basset term has little effect near the step but causes the particle velocity to relax more slowly away from the step, greatly increasing the particle relaxation distance. This example indicates that the Basset term cannot be arbitrarily ignored in flows with large velocity gradients even when fairly dense particles are considered.

A second example of the importance of various terms in Tchen's equation of motion can be seen in the solution given by Hjelmfelt and Mockros (Ref. 2) for a particle responding to a uniformly sinusoidally oscillating fluid flow field. Their results for amplitude ratio and phase angle of the particle velocity in terms of the fluid velocity, for various approximations of the equation of motion, are

$$\frac{v}{u} = \sqrt{(1 + f_1)^2 + f_2^2} \quad (13)$$

and

$$\phi = \tan^{-1} \left(\frac{f_2}{1 + f_1} \right) \quad (14)$$

where

1. General solution

$$f_1 = \frac{\left[1 + \frac{9 N_f}{\sqrt{2} (S + 1/2)} \right] \left[\frac{1 - S}{S + 1/2} \right]}{\frac{81}{(S + 1/2)^2} \left[2N_f^2 + \frac{N_f}{\sqrt{2}} \right]^2 + \left[1 + \frac{9 N_f}{\sqrt{2} (S + 1/2)} \right]^2} \quad (15)$$

$$f_2 = \frac{\frac{9 (1 - S)}{(S + 1/2)^2} \left[2 N_f^2 + \frac{N_f}{\sqrt{2}} \right]}{\frac{81}{(S + 1/2)^2} \left[2N_f^2 + \frac{N_f}{\sqrt{2}} \right]^2 + \left[1 + \frac{9 N_f}{\sqrt{2} (S + 1/2)} \right]^2} \quad (16)$$

where

$$S = e_p/e_f \quad (17)$$

and

$$N_f = \sqrt{\frac{\nu}{\omega d^2}} \quad (18)$$

2. Type I approximation, neglecting the history term,

$$f_1 = \frac{\frac{(1 - S)}{(S + 1/2)}}{\left[\frac{18N_f^2}{(S + 1/2)} \right]^2 + 1} \quad (19)$$

$$f_2 = \frac{18 N_f^2 \frac{(1 - S)}{(S + 1/2)^2}}{\left[\frac{18N_f^2}{(S + 1/2)} \right]^2 + 1} \quad (20)$$

3. Type II approximation, neglecting the history and apparent mass terms,

$$f_1 = \frac{(1 - S)/S}{\left[\frac{18N_f^2}{(S + 1/2)} \right]^2 + 1} \quad (21)$$

$$f_2 = \frac{18N_f^2 (1 - S)/S^2}{\left[\frac{18N_f^2}{(S + 1/2)} \right]^2 + 1} \quad (22)$$

4. Type III approximation, neglecting the pressure, history, and apparent mass terms,

$$f_1 = \frac{-1}{\left[\frac{18N_f^2}{S} \right]^2 + 1} \quad (23)$$

$$f_2 = \frac{-18N_f^2/S}{\left[\frac{18N_f^2}{S} \right]^2 + 1} \quad (24)$$

Figure 2a shows the amplitude ratio as a function of nondimensional frequency for a density ratio, S , of 1000, which approximately represents water particles in air. This indicates that

for high frequencies or for large particles (small N_f), the history term becomes significant, whereas the apparent mass and pressure terms are insignificant. The phase angle, Fig. 2b, is slightly more sensitive to the additional terms. This example corresponds to the case where the relative velocity is nearly zero, and the relative acceleration remains finite. As the density ratio decreases, as indicated in Figs. 3a and b for $S = 2.65$, the higher-order terms become more significant.

These examples indicate that the Basset term cannot be ignored in a general sense because of order-of-magnitude analysis involving only the coefficient of the term, as is usually done. The term must be evaluated on a case-by-case basis to ensure that the physics of the particle/fluid interaction are properly modeled. This is especially true for the small, light particles of interest to velocimetry since the inertia term can be quite small, and the Basset term is still finite.

2.3 EXTENSION BEYOND STOKES FLOW

The repercussions of the Stokes flow assumption that underlie the derivation of Eqs. (1) and (4) should be noted. The assumption is that the convective terms of the Navier Stokes equation are negligible. This assumption limits the equation to very low Reynolds numbers and thus to cases of very small particle lag. Another consequence of the Stokes flow assumption, as noted by Ho (Ref. 15), is that the possibility of any transverse (lift) forces on the particle is eliminated. Saffman (Ref. 16) derived the lift force on a spherical particle in a uniform shear flow as

$$F_L = 1.6125 d^2 \sqrt{\rho_f \mu} \left| \frac{\partial u}{\partial y} \right|^{1/2} (v - u) \quad (25)$$

Evaluating the order-of-magnitude of this force relative to the left-hand side of Eq. (4),

$$\text{Lift Force} \quad \sim 0 \left[\frac{3}{d} \frac{\rho_f}{\rho_p} \nu \right]$$

The lift force is then of the same magnitude as the Basset history integral for a particle in a shear. Unfortunately, there is no general expression for the lift force on a sphere in an unsteady nonuniform flow field, and hence this force is usually ignored. Fortunately, the lift force, like drag, is proportional to the relative velocity and is usually negligible when compared to the drag force.

The general procedure for extending this equation to higher Reynolds numbers has been to multiply various terms by empirically determined coefficients. Odar and Hamilton (Ref. 17) performed an elaborate experimental study and concluded that empirical constants were

required on the drag, Basset, and apparent mass terms. Later work by Karanfilian and Kotas (Ref. 18) indicated that, at least for heavy particles in sinusoidally oscillating flows, the drag term required empirical modification, and the other terms could be neglected. In this work the empirical constants of Odar and Hamilton (Ref. 17) will be employed because of the more general validation and more thorough scrutiny they have been given. The drag term in the equation of motion then becomes

$$\text{Drag Term} = \frac{3m_f}{4d} C_d w_i |w_i| \quad (26)$$

where

$$w_i = v_i - u_i - \frac{d^2}{24} \nabla^2 u_i \quad (27)$$

and

$$|w_i| = \sqrt{\sum_i w_i^2} \quad (28)$$

The empirical coefficient for the Basset term is taken from Ref. 14 as

$$\Delta_H = 0.48 + \frac{0.52 A_n^3}{(1 + A_n)^3} \quad (29)$$

where

$$A_n = \frac{d}{|w_i|^2} \frac{d|w_i|}{dt} \quad (30)$$

A number of empirical drag coefficients are available to extend the particle equation of motion beyond the Stokes regime. The simplest extensions of Stokes drag law attempt to model the incompressible sphere drag coefficient curve (Fig. 4) at higher Reynolds numbers. The more complex laws add corrections for compressibility, rarefaction, heat-transfer, and shape effects. Donald O. Barnett of the University of Alabama presents a drag coefficient based on the experiments of Bailey and Hiatt (Ref. 19) of the form

$$C_d = C_{do} \sum_{i=1}^4 F_i \quad (31)$$

where

$$C_{do} = \text{Stokes drag} = 24/\text{Re}_R$$

$$F_1 = \text{Inertial (Re) effect}$$

$$F_2 = \text{Compressibility (M) effect}$$

$$F_3 = \text{Rarefaction (Kn) effect}$$

$$F_4 = \text{Particle shape effects.}$$

Barnett expresses the inertial influence coefficient as

$$F_1 (\text{Re}_R) = 1 + 0.197 \text{Re}_R^{0.63} + 0.00026 \text{Re}_R^{1.38} \quad (32)$$

The effect of increasing Reynolds number is to increase the drag above that which is predicted for Stokes flow, as seen in Fig. 5. Compressibility effects are modeled by

$$F_2 (M_R) = 1 + 2/3 (M_R - 0.15)^2 \quad (33)$$

for $M > 0.15$. As shown in Fig. 6, the effect of compressibility is to increase the drag above Stokes drag. The rarefaction influence coefficient is given as

$$F_3 (\text{Kn}) = (1 + \text{Kn} (1 + A e^{-B/\text{Kn}}))^{-1} \quad (34)$$

where $A = 1.34285$ and $B = 0.277$ for $\text{Kn} < 0.85$, and $A = 1.2243$ and $B = 0.18$ for $\text{Kn} > 0.85$. As shown in Fig. 7, the effect of rarefaction is to decrease the Stokes drag. The particle shape is accounted for by

$$F_4 (\psi) = 1 + 4.065 (1 - \psi) \text{Re}_s^{0.238} \quad (35)$$

where ψ is the shape factor defined by

$$\psi = \frac{\pi D_{ES}^2}{A_p} \quad (36)$$

and

$$D_{ES} = \left(\frac{6 v_p}{\pi} \right)^{1/3} \quad (37)$$

A_p and v_p are the surface area and volume of the particle. Re_s is the particle Reynolds number based on the equivalent spherical diameter from Eq. (37). As the particle becomes less spherical (or as ψ decreases from 1), the drag increases as shown in Fig. 8. Heat-transfer effects may be added to Barnett's drag law by calculating the effective viscosity for calculating the Reynolds number as recommended by Golovin and Fominysk (Ref. 20). This is done by calculating an effective temperature that is the geometric mean of the fluid and particle temperatures. The effective viscosity is calculated based on this effective temperature. As shown in Fig. 9, the effect of increasing the temperature of the particle relative to the temperature of the fluid is to increase sphere drag.

Barnett's drag law is limited to particle relative Mach number (M_R) of less than 0.8, because the transonic drag rise and subsequent supersonic drag of a sphere is not modeled. Barnett's drag law is useful for evaluating the effects of various parameters on particle motion but must be used with caution in regions of large particle lag, such as the region downstream of a strong shock. In such regions the drag is better represented by the drag law of Crowe (Ref. 21).

$$C_d = (C_{d1} - 2) \exp [-3.07 \gamma^{1/2} M_R / Re_R] G(Re_R) \quad (38)$$

$$+ [h(M_R) / \gamma^{1/2} M_R] \exp [-Re_R / (2M_R)] + 2$$

where

$$C_{d1} = (24 / Re_R) (1 + 0.158 Re_R^{2/3}) \quad (39)$$

and

$$\log_{10} G(Re_R) = 1.25 [1 + \tanh (0.77 \log_{10} Re_R - 1.92)] \quad (40)$$

and

$$h(M_R) = (2.3 + 1.7 (T_p / T_f)^{1/2}) - 2.3 \tanh (1.17 \log_{10} M_R) \quad (41)$$

Crowe's drag law includes inertia, compressibility, rarefaction, and heat-transfer effects. Although Crowe's drag law is valid over a wider range of particle conditions than Barnett's, it makes simple parametric studies of the various correction terms more difficult.

2.4 NUMERICAL SOLUTION OF THE EQUATION OF MOTION

Equation (4) can be put into the following form to facilitate numerical solution:

$$\begin{aligned}
 \frac{dv_i}{dt} = & - \frac{3C_d}{4d} \frac{m_f}{(m_p + 1/2 m_f)} w_i |w| + \frac{(m_p - m_f)}{(m_p + 1/2 m_f)} g_i \\
 & + \frac{m_f}{(m_p + 1/2 m_f)} \frac{Du_i}{Dt} + \frac{m_f}{2(m_p + 1/2 m_f)} \frac{d}{dt} \left\{ u_i [\vec{Y}(t), t] \right. \\
 & \left. + \frac{d^2}{40} \nabla^2 u_i | \vec{Y}(t) \right\} - \Delta_H \frac{3\pi d^2 \mu}{2(m_p + 1/2 m_f)} \left\{ \frac{d}{d\tau} \frac{w_i [\vec{Y}(\tau), \tau]}{\sqrt{\pi\nu(t - \tau)}} \right\} d\tau
 \end{aligned} \tag{42}$$

This can be interpreted as a nonlinear first-order differential equation of the form

$$\frac{dv_i}{dt} = f_i \tag{43}$$

A few comments on the stability of Eq. (42) are in order. If we assume that the drag is given by Stokes law for simplicity, and we ignore the lower terms, f_i can be written

$$f_i = \frac{18\mu}{d^2 (e_p + 1/2 e_f)} w_i \tag{44}$$

The Jacobian is then given by

$$J = N_s \begin{bmatrix} 1 & 0 & 0 \\ 0 & 1 & 0 \\ 0 & 0 & 1 \end{bmatrix} \tag{45}$$

where

$$N_s = \frac{18\mu}{d^2 (e_p + 1/2 e_f)} \tag{46}$$

The system of equations is quite stable and easy to solve for large particles. As the particle diameter becomes small, N_S becomes quite large as shown in Fig. 10, and the system of equations becomes stiff. Physically, as the particle diameter approaches zero, the relative velocity also approaches zero. Numerically this is not always the case, and hence small time steps are required to maintain the stability of the system. This problem can be circumvented by arbitrarily setting the particle velocity to the fluid velocity for particle sizes below a given size or for particle relative Reynolds numbers below a specified value. Since interest in this effort is in the response of very small particles to turbulence, a limiting value of particle Reynolds number of 10^{-12} was chosen to be compatible with the convergence criteria used in numerically solving the particle equation of motion.

The Basset term contains an apparent singularity at the upper limit of integration ($\tau = t$). This must be considered in the numerical solution of the particle of motion. Setting

$$f(\tau) = \frac{dw_i}{d\tau} \frac{1}{\sqrt{\pi\nu}} \quad (47)$$

the integral is

$$\int_0^t \frac{f(\tau) d\tau}{\sqrt{t-\tau}} \quad (48)$$

Integrating by parts, this becomes

$$2\sqrt{t} f(0) + 2 \int_0^t \sqrt{t-\tau} \frac{df}{d\tau} d\tau \quad (49)$$

When the integral in Eq. (49) is evaluated numerically, the contribution to the sum by the point τ is zero. Thus this point is not a singularity. Physically, this is consistent with the proper interpretation by the Basset history term since the contribution of the present time to the history of the particle should be negligible. This simplifies the numerical solution of the particle equation of motion since numerical calculation of the integral term does not require a knowledge of the velocities at the present time step.

A computer code was written to solve Eq. (42). The code uses a fourth-order forward marching Adam's predictor-corrector technique to integrate for the particle velocity at a given time step. The corrector term was iterated until the desired convergence was obtained. The convergence criteria were

$$\frac{v^i - v^{i-1}}{u^i} \leq 1 \times 10^{-6} \quad (50)$$

where i was the iteration index. Each component of the velocity was required to converge independently. These criteria, though somewhat restrictive, were found to guarantee converged solutions for any case to which they were applied. The same numerical technique was used to integrate the particle velocity to obtain particle position. The integral term was evaluated using a trapezoidal rule integration, and the required fluid derivatives were evaluated using simple backward differencing. The Adam's method does suffer occasional numerical instability because of the stiffness of the equation of motion. To overcome this problem, a fourth-order Runge-Kutta solver was used to start the solution and to restart the solution when the Adam's method diverged. The Adam's method is preferred to the Runge-Kutta, because it is much faster and allows simple testing for convergence to a desired accuracy.

3.0 PARTICLE SIZE DISTRIBUTION EFFECTS

A commonly occurring and often ignored phenomenon in laser velocimetry is the broadening of measured velocity distributions attributable to a particle size distribution in the presence of a velocity gradient. This broadening is often interpreted as an increase in turbulence intensity when it actually has nothing to do with the turbulence level of the fluid. Three simple examples frequently found in high-speed LV applications are given here.

Before proceeding to a discussion of particle size distribution effects on turbulence measurements with the LV, a brief outline of the interpretation of velocimeter data will be given. The discussion will be limited to two-dimensional data for simplicity, although extension to three dimensions is straightforward.

A sample velocity correlogram is given in Fig. 11. For typical velocity distributions, the probability distribution takes the form of an ellipse when plotted in velocity space. The turbulence intensity in the x and y directions is given by the variance of the velocity distribution in each direction and may be interpreted as the square of half the projected ellipse length on each axis. The Reynolds shear is calculated from the cross correlation of the simultaneously measured u_x and u_y velocity components and may be interpreted as the angular rotation of the correlogram relative to the coordinate system of interest.

The determination of the principle turbulence intensities, or those where the Reynolds shear is zero, is given by the following relations in two dimensions:

$$\overline{u_{10}'^2} = \overline{u_1'^2} \cos^2\theta + \overline{u_1'u_2'} \sin 2\theta + \overline{u_2'^2} \sin^2\theta \quad (51)$$

$$\overline{u_{20}'^2} = \overline{u_1'^2} \sin^2\theta - \overline{u_1'u_2'} \sin 2\theta + \overline{u_2'^2} \cos^2\theta \quad (52)$$

where

$$\theta = \frac{1}{2} \tan^{-1} \left[\frac{2 \overline{u_1' u_2'}}{\overline{u_1'^2} + \overline{u_2'^2}} \right] \quad (53)$$

and $\overline{u_{10}'^2}$ and $\overline{u_{20}'^2}$ are the principle stresses and $\overline{u_1'^2}$, $\overline{u_2'^2}$, and $\overline{u_1' u_2'}$ are the stresses in the measurement coordinate system.

3.1 NORMAL SHOCKS

A very simple example of how particle dynamics can affect turbulence measurements with the LV is a normal shock. The momentum of a particle cannot be dissipated in the few mean free paths comprising the shock thickness. Theoretical particle response to a bow shock in front of a cylinder at a Mach number of four is shown in Fig. 12 for olive oil particles of various sizes. The different particle sizes respond to the shock at different rates. The velocity distribution measured using a polydispersed particle size distribution would initially be tight (the variance would be small) in the free stream ahead of the shock. The distribution rapidly spreads as the particles relax at different rates behind the shock. Finally, as the particles begin to relax to the velocity behind the shock, the distribution forms a peak at the low velocity end with a tail to the higher velocities. As the larger particles relax to the fluid velocity, this tail begins to disappear, and the low velocity peak grows.

Experimental results for this case are shown in Fig. 13. The flow was seeded with olive oil using a Collison atomizer, which produces a broad size range of particles as shown in Fig. 14. The velocity distributions correspond to what one would expect from a particle dynamics point of view. There is a strong peak upstream of the shock in the free stream, a very broad velocity distribution behind the shock, and a velocity peak that begins to develop at the lower velocities as the cylinder is approached. The actual fluid turbulence values are masked by the spread in the velocity distribution attributable to the particle size distribution present in the experiment.

3.2 OBLIQUE SHOCKS

The previous example can be extended to two-dimensional flows by examining the simple case of an oblique shock. Calculations for a 40-deg oblique shock with an upstream Mach number of 2.2 are shown in Figs. 15 and 16. X_s is the distance from the shock measured perpendicular to the shock. The calculations show a behavior for each velocity component similar to that seen for the case of the normal shock. The velocity distribution is tight and near the upstream velocity near the shock, then spreads dramatically, and finally develops

a tight peak at the downstream velocity with an associated tail of lagging particles.

Figures 16a to 16e, presented in velocity space, indicate that a particle size distribution will also affect the Reynolds shear measurement. As mentioned in the introduction to this section, the orientation of the turbulence ellipse in velocity space is an indication of the Reynolds shear. These figures indicate that the ellipse would be rotated as though a strong negative Reynolds shear were present. This particle-induced velocity correlation could well hide the actual turbulence-induced velocity correlation.

3.3 LAMINAR SUPERSONIC BOUNDARY LAYER

The previous two cases indicate that particle dynamics can greatly affect turbulence measurements with the LV in the presence of strong velocity gradients, such as the gradients associated with shocks. The present example illustrates that this effect can also be seen in flows with milder gradients, such as in the laminar boundary layer on a 7-deg half-angle cone at a Mach number of four.

Figure 17 shows calculated particle response and actual LV data taken in a laminar boundary layer on a cone with a similar seed particle size distribution as shown in Fig. 14. The calculated results in Fig. 17 indicate that the apparent increase in turbulence in the center of the boundary layer, noted by the broadening of the velocity distribution, is actually attributable to the broad particle size distribution present and is not a feature of the flow.

3.4 MEAN FLOW PARTICLE SIZE REQUIREMENTS

These three examples point out the care that must be taken in acquiring and interpreting LV data. Particle dynamics effects must be considered and seed particle size distributions must be minimized if meaningful results are to be acquired with the LV. It also points out that the LV may not be the instrument of choice for making turbulence measurements in shock interaction regions, an application of velocimetry many seem to make. In these regions care must be taken to identify the actual particle size distribution the LV is "seeing" and to assure that measurements are made outside of the relaxation region for these particles. These examples do not indicate what size particle is required to obtain meaningful turbulence measurements since, to this point, only mean flow particle lag has been considered.

A simple expression for estimating mean flow particle lag can be derived from the particle equation of motion, assuming that only the drag term is important. This yields the following equation:

$$\frac{u_i}{v_i} = 1 + \frac{C_{d0}}{C_d} \frac{1}{N_s v_i} \frac{dv_i}{dt} \quad (54)$$

where the derivative can be expressed

$$\frac{dv_i}{dt} = v_j \frac{\partial v_i}{\partial x_j} \quad (55)$$

and C_{d0} is the Stokes drag. This equation is not considered accurate enough for data correction but is valuable for identifying areas in the flow in which particle lag may be present. The equation demonstrates the importance of maximizing the Stokes number in regions of the flow where large velocity gradients are present.

4.0 TURBULENCE MODEL

In order to further study the effects of particle size on their response to turbulence, a model of the turbulent flow must be constructed. There are basically two ways to visualize turbulence in a flow field, either from an Eulerian or a Lagrangian reference frame. If we were to visualize turbulence as a finite number of discrete eddies, each with its own random fluid characteristics convected with mean velocity \bar{u} , then in one dimension the turbulence may be represented as in Fig. 18a. As these eddies are convected past a probe, the velocity measured would be as shown in Fig. 18b. This could easily be represented as a Fourier series and could be simulated using white noise Monte Carlo techniques. Thus, in an Eulerian reference frame, the turbulence appears to be the superposition of random frequency sine waves. If the probe were given a velocity relative to the turbulence, the frequency domain of the Eulerian turbulence spectra would change, producing an apparent higher frequency if the probe relative velocity is of opposite sign to the mean fluid velocity \bar{u} . Hence, the Eulerian representation of turbulence is a function of the rate of convection of eddies past the probe and the individual eddy characteristics.

Particles interact with turbulence from a Lagrangian point of view. Figure 19a is an example of how the eddies appear to the particle. At time t the particles and the eddy are both centered at point c with a relative velocity of \bar{w}_1 . As time increases, the particle exits the eddy and enters a second eddy with a relative velocity \bar{w}_2 . In the Lagrangian reference frame, the turbulence appears more as a randomly spaced set of velocity discontinuities as the particle moves from one eddy to the next, as shown in Fig. 19b. The number of these discontinuities encountered by the particle is a function of the time and length scales of the turbulence as well as the size and density of the particle. If a particle is small and light enough, it may remain in the same eddy throughout the eddy's lifetime and see very few discontinuities as

it passes through the flow field. If a particle is large and heavy, it will "bust through" the eddies and not have time to respond to any of the velocity discontinuities it encounters.

For the large, heavy particles that fail to respond to the turbulence, modeling of the time scale and the internal structure of the turbulent eddy are unimportant, because the particle will generally encounter a new eddy at each time step. Several simple turbulence-particle interaction models take advantage of this fact since it simplifies the calculation of particle response. As the particles become smaller and lighter, the internal structure of the eddy and the time and length scales become more important. Since information on these length scales and on the internal eddy structure is difficult to come by, the proper simulation of the particle response for the small particles of interest to velocimetry becomes more difficult.

The turbulence model used in this effort assumes that the turbulence is multinormal with the off-diagonal correlation functions given by the Reynolds shear values. The mean fluid velocities, fluid properties, turbulence intensities, and Reynolds shears are assumed to be given functions of position in the flow field, determined from experimental data or from calculations.

Information on time scales and eddy internal structure is often more difficult to come by. For wake flows or free shear flows, empirical relationships are available from Shuen (Ref. 3) and Tennekes and Lumley (Ref. 22). The time scale is defined by

$$T_{Ei} = \int_0^{\infty} \frac{\overline{u_i(\tau)u_i(t - \tau)}}{\overline{u_i'^2}} d\tau \quad (56)$$

and the length scale is defined by

$$L_{ii} = \int_0^{\infty} \frac{(u_{ri}) \vec{x} = A (u_{ri}) x = B}{\overline{u_i'^2}} dr \quad (57)$$

The Taylor microscale is defined as

$$\lambda_i = \frac{1}{3} \frac{U}{(\partial u_i / \partial x_i)^2}$$

These can be approximated by

$$\lambda_i = 86.06 \frac{\nu}{\sqrt{U}} \quad (59)$$

$$L_{11} = 0.077 A \frac{\lambda_1^2 \sqrt{U}}{\nu} \quad (60)$$

$$L_{22} = L_{33} = \frac{1}{2} L_{11} \quad (61)$$

$$T_{E1} = \frac{2}{\sqrt{3}} \frac{L_{11}}{\sqrt{U}} \quad (62)$$

where

$$U = \sum_{i=1}^3 \overline{u_i'^2} \quad (63)$$

and A is a constant of order one. These scales can be approximated from eddy viscosity or mixing length information using the following relation from Tennekes and Lumley (Ref. 22):

$$L_{11} = \frac{1}{2} \ell \quad (64)$$

where L_{11} is assumed to be the direction aligned with the mean flow vector, and ℓ is Prandtl's mixing length. With scales defined as above, the turbulent eddies are modeled as follows. The random duration of the eddy is modeled by assuming that the autocorrelation is given by the Poisson from $e^{-t/T_{E1}}$. The spatial distribution of the turbulence must also be modeled since the solid particle will not exactly follow any single fluid particle. The spatial distribution is assumed to be given by Frenkiel's analytical form (Ref. 23),

$$\overline{u_{ic}' u_{jx}'} = \sqrt{\overline{u_{ic}'^2}} \sqrt{\overline{u_{jx}'^2}} \exp \left[\frac{-r}{(n+1)L_{ij}} \right] \cos \left[\frac{nr}{(n^2+1)L_{ij}} \right] \quad (65)$$

where r is the distance between the fluid particle at point c and the solid particle at point x . Currently n is set to zero. The velocity components at points c and x are assumed to be governed by a multinormal distribution with a covariance matrix of

$$\begin{bmatrix} \overline{u_{c1}' u_{c1}'} & \overline{u_{c1}' u_{c2}'} & \overline{u_{c1}' u_{x1}'} & \overline{u_{c1}' u_{x2}'} \\ \overline{u_{c2}' u_{c1}'} & \overline{u_{c2}' u_{c2}'} & \overline{u_{c2}' u_{x1}'} & \overline{u_{c2}' u_{x2}'} \\ \overline{u_{x1}' u_{c1}'} & \overline{u_{x1}' u_{c2}'} & \overline{u_{x1}' u_{x1}'} & \overline{u_{x1}' u_{x2}'} \\ \overline{u_{x2}' u_{c1}'} & \overline{u_{x2}' u_{c2}'} & \overline{u_{x2}' u_{x1}'} & \overline{u_{x2}' u_{x2}'} \end{bmatrix} \quad (66)$$

The turbulent intensities and Reynolds shear at point x are assumed to be the same as those at point c because of the small size of the eddy relative to the scale of the mean flow. The cross terms between points x and c are assumed to be given by Eq. (65). The random fluid velocities at points x and c are generated by the multinormal form outlined by Rubinstein (Ref. 24),

$$\begin{bmatrix} u_{1c}' \\ u_{2c}' \\ u_{1x}' \\ u_{2x}'' \end{bmatrix} = c_{ij} R_{zi} \quad (67)$$

where

$$C_{ij} = \frac{\overline{u_i' u_j'}}{\left(\overline{u_j'^2} - \sum_{k=1}^{j-1} C_{jk}^2 \right)^{1/2}} \quad (68)$$

R_{zi} are randomly generated one-dimensional normal variates. The correlation given by Eq. (64) begins to lose meaning at large values of r , and the random velocities at point x become independent of the velocities at point c . To avoid losing this model of the internal structure of the turbulence, the code changes from following the fluid particle at point c to following the fluid particle at point x if r is greater than the Taylor microscale λ_1 .

The variates R_{z1} and R_{z2} are generated when an eddy is created, and they remain constant for the lifetime of the eddy. The variates R_{z3} and R_{z4} are generated at each time step. If the eddy's random lifetime is exceeded, then new random variates R_{z1} and R_{z2} are generated, and the model begins to follow the fluid particle located at point x . If the distance r between points x and c exceeds the dissipation length scale λ , then the model changes from following the fluid particle at point c to the fluid particle at point x . This is accomplished by calculating new random variates R_{z1} and R_{z2} from the fluid velocity at point x from

$$R_{z1} = \frac{u_{1x}'}{C_{11}} \quad (69)$$

$$R_{z2} = \frac{u_{2x}' - c_{12} R_{z1}}{C_{22}} \quad (70)$$

These variates remain constant until the length or time scales of the eddy are exceeded.

Figure 20 graphically describes the process the model uses in following a particle through a turbulent flow field. In Fig. 20a, the particle begins at the center of a fluid eddy. The minimum radius of this eddy is the Taylor microscale λ_1 . As time progresses, the particle remains in this eddy until the eddy's random life, governed by a Poisson distribution, is exceeded. The process is modeled by drawing a random variate from [0,1] at each time step and comparing it to $\Delta t/T_{E1}$. If the variate is less than $\Delta t/T_{E1}$, new values of u_i' are generated; if not, u_i' remains the same during time interval Δt .

In Fig. 20b, the particle again begins at the center of an eddy of minimum radius λ_1 . As time progresses, the particle exits this eddy. At this point, the code begins to follow the eddy centered at point x. This proceeds until the particle exits the new eddy, or the random duration of the eddy is exceeded.

The turbulence model used in this effort attempts to model the internal structure of the turbulence. For the small, light particles required for accurate velocimetry measurements, it is this structure that the particles must follow. The structure is somewhat simplified by assumptions concerning the probability distributions governing the process. Although it is fully realized that all turbulence velocity distributions are not truly normal, and length and time correlations are not strictly Poisson, these forms should be adequate to describe the particle response within the framework of a simple turbulence model.

5.0 PARTICLE RESPONSE TO TURBULENT FLOW FIELDS

The particle equation-of-motion code developed in Section 2.0 was coupled with the Monte Carlo turbulence model developed in Section 4.0. Individual particles were followed through the randomly varying flow field. One thousand samples were used to calculate the particle and fluid statistics at various stations in the flow. The number 1000 was chosen as a compromise to allow a reasonable confidence band without consuming excessive computational resources.

5.1 GRID-GENERATED TURBULENCE

The code was first applied to the grid-generated turbulence experiment of Snyder and Lumley (Ref. 25). This provided a flow field with near-homogeneous and near-isotropic turbulence with no mean flow velocity gradients. In this experiment particle velocity autocorrelation functions and particle dispersion were measured in a vertical 6.55-m/sec flow behind a 2.54-cm-sq mesh. Fluid turbulence intensities were measured with a hot wire and are shown in Fig. 21. These curves are shown to be adequately represented by

$$\overline{u_1'^2} = \frac{u^2}{42.4 (x/m - 16)} \quad (71)$$

$$\overline{u_2'^2} = \frac{u^2}{39.4 (x/m - 12)} \quad (72)$$

where m is the mesh size. The Lagrangian integral length scale and Taylor microscale were tabulated in Ref. 25. These tabulated values were fitted by

$$L_{11} = 2.19327 + 0.0128493 x/m + 8.582 \times 10^{-6} \left(\frac{x}{m}\right)^2 \quad (73)$$

$$\lambda_1 = 0.00436 x/m + 0.2507 \quad (74)$$

Equations (61) and (62) were used to obtain L_{22} and T_{E1} . The length and time scales are shown in Figs. 22 and 23, respectively.

Experimental results are given in Ref. 25 for the four different particles given in Table 1. The Stokes number, defined as,

$$N_s = \frac{18\mu}{d^2 (\rho_p + 1/2\rho_f)} \quad (75)$$

is given as a parametric indication of particle response. As the Stokes number decreases, particle response to turbulence will also decrease.

Calculations were made for the four different particles in Table 1. The particle calculations were begun at the experimental particle injection point of $x/m = 20$. The particle velocity was assumed equal to the randomly fluctuating fluid velocity at the injection point. The experimental measurements began at $x/m = 41$. Because of the large separation between the injection point and the measurement stations, there was no influence of the assumed particle initial conditions on the calculated particle response at the measured stations.

Comparison of the predicted and measured particle dispersions is shown in Fig. 24. The agreement in all cases is considered good. Even better agreement can be achieved for each case by slightly varying the Lagrangian length and time scales for each different kind of particle. This was not done because such "fine tuning" cannot be done when the code is used to predict the response of the smaller particles of interest to velocimetry. Hence, this example should be representative of the results to be expected from this code for various size and density particles.

Predicted and experimental turbulent velocity decays are shown in Fig. 25. Again there is excellent agreement. The roll off of the copper particle decay predicted by the code is not shown by the experimental data, but Snyder (Ref. 25) indicates he has little faith in the measurements at this point because of his measurement technique and the very low values of particle velocity fluctuations there. For the smaller, lighter particles of interest in this study the code does exceptionally well.

Following the successful validation of the code, calculations were made for various particle sizes and particle densities to investigate what particles were required to properly characterize the turbulence. Results of these calculations are shown in Fig. 26 for two different axial stations. The figure indicates that the particle response is essentially the same for these two locations, which is to be expected because of the small change in turbulent intensities between them (a turbulent intensity of 1.9 percent at x/m of 80 compared with a turbulent intensity of 1.5 percent at x/m of 124). The turbulence is properly reproduced by particles with Stokes numbers greater than 1.3×10^4 , which corresponds to a $5\text{-}\mu\text{m}$ water particle. The mean velocity values are still quite good for particles with Stokes numbers of 12, which corresponds to a $160\text{-}\mu\text{m}$ water particle. The calculations also indicate that the particles respond differently to different components of the turbulence. The particles respond to the turbulence component in the direction of the mean flow vector significantly better than they respond to the component of turbulence normal to the mean flow vector. This difference in response seems to disappear as the particles begin to follow the fluid velocity turbulent excursions. The results indicate that the fluid turbulence properties will be underpredicted when particles that are too large to respond to the flow are used.

Some physical insight into the particle response to turbulence can be gained from the Lagrangian turbulence described in Section 4.0 and shown in Fig. 19. The particle response is indicative of the ratio of the particle relaxation time to the time scale of the turbulence. If the particle relaxation time is of the same order as the time scale of the turbulence, the particle never has an opportunity to relax to the fluid velocity of the eddy in which it is located. As the particle relaxation time decreases, the particle more faithfully reproduces the fluid motion. The Stokes number is an indicator of the time response of a particle and serves as a good parameter for evaluating particle response. Figure 27 indicates that the product of the Stokes number and the integral time scale must be of the order of 1000 for accurate turbulence measurements in this flow field.

5.2 SUBSONIC AXISYMMETRIC JET

The second validation case for the code was the axisymmetric jet experiment of Yuu et al. (Ref. 26). In this experiment, particle diffusivity was measured in a simple self-preserving subsonic jet. This flow offered the opportunity to evaluate the effect of particle dynamics on Reynolds shear measurements and also included the effects of a mean flow velocity gradient.

Yuu presents curve fits of the turbulence intensities and mean flow velocities for this jet based on the experiments of Liepman and Laufer (Ref. 27), Laurence (Ref. 28), Corrsin and Uberoi (Ref. 29), and Wygnanski (Ref. 30). The basic flow structure is shown in Fig. 28. The potential core of the jet is defined by

$$x/D < 6.8 \quad (76)$$

$$r/D < 0.5 - \frac{\bar{x}}{13.6} \quad (77)$$

where D is the nozzle exit diameter. The velocities in this region are given by

$$\frac{\bar{u}_1}{u_o} = 1.0 \quad (78)$$

$$\frac{\bar{u}_2}{u_o} = 0 \quad (79)$$

$$\overline{u_1'^2} = \overline{u_2'^2} = 0 \quad (80)$$

where u_o is the nozzle exit velocity. In the mixing region, defined by

$$x/D < 6.8 \quad (81)$$

$$r/D > 0.5 - \frac{x}{13.60} \quad (82)$$

the velocities are given by

$$\frac{\bar{u}_1}{u_o} = 1 - 92.6 \left(\eta_1 + \frac{1}{13.6} \right)^2 + 340 \left(\eta_1 + \frac{1}{13.6} \right)^3 \quad (83)$$

$$\frac{\bar{u}_2}{u_o} = -4.05 \eta_1^2 - 11.7 \eta_1^3 + 255 \eta_1^4 \quad (84)$$

$$\frac{\overline{u_1'^2}}{u_o^2} = 0.0217 \exp(-200 \eta_1^2) \quad (85)$$

$$\frac{\overline{u_2'^2}}{u_o^2} = 0.0103 \exp(-217 \eta_1^2) \quad (86)$$

where $\eta_1 = (\bar{r} - 0.5)/\bar{x}$. In the main region of the jet, defined by $\bar{x} > 6.8$, the velocities are given by

$$\frac{\bar{u}_1}{u_o} = (6.8 - 630 \eta_2^2 + 2313 \eta_2^3) \bar{x}^{-1} \quad (87)$$

$$\frac{\bar{u}_2}{u_o} = (3.4 \eta_2 - 472 \eta_2^3 + 1851 \eta_2^4) \bar{x}^{-1} \quad (88)$$

$$\frac{\overline{u_1'^2}}{u_o^2} = \frac{1.91}{x^2} \exp(-154 \eta_2^2) \quad (89)$$

$$\frac{\overline{u_2'^2}}{u_o^2} = \frac{2.26}{x^2} \exp(-178 \eta_2^2) \quad (90)$$

where $\eta_2 = \bar{r}/\bar{x}$. The Reynolds shear in the mixing region was taken from Chow (Ref. 31) as

$$\frac{\overline{u_1' u_2'}}{u_o^2} = 0.012 (1 - 204.5 \eta_1^2) \exp[-(30 \eta_1 + 0.2)^2/1.704] \quad (91)$$

The Reynolds shear in the main jet is given by Hinze's expression (Ref. 23) as

$$\frac{\overline{u_1 u_2}}{u_o^2} = \frac{23.12 \eta_2}{\sqrt{2} \bar{x}^2} \left[1 + \frac{\eta_2^2}{0.01568} \right]^{-3} \quad (92)$$

The integral length scale is approximated by (Refs. 26 and 30)

$$\bar{L}_m = L_m/D = 0.0385 \bar{x} \quad (93)$$

$$L_{11/D} = \bar{L}_m \left(\exp \left\{ -100 \left[\bar{r} + 0.45 \right] / \bar{x} \right\}^2 + \exp \left\{ -100 \left[\bar{r} - 0.45 \right] / \bar{x} \right\}^2 \right)^{1/2} \quad (94)$$

for $\bar{x} < 4$,

$$L_{11/D} = \bar{L}_m \exp(-40 \eta_2^2) \quad (95)$$

for $4 < \bar{x} < 10$,

$$L_{11/D} = \bar{L}_m \exp(-50 \eta_2^2) \quad (96)$$

For $\bar{x} > 10$, L_{22} , λ_1 , and T_{E1} are given by (Ref. 30)

$$L_{22} = L_{11}/2.54 \quad (97)$$

$$\lambda_1 = \left(5.113 \sqrt{\frac{\nu L_{11}}{U}} + 1.9855 \times 10^{-3} \right) \sqrt{\frac{164.05}{u_o}} \quad (98)$$

$$T_{E1} = 0.48 \frac{L_{22}}{\sqrt{U}} \quad (99)$$

The above fluid velocity and turbulence scales are graphically represented in Figs. 29 through 34.

Calculations were made for 20- μ m-diam fly-ash particles in a 100-m/sec jet to compare with the experimental results of Yuu (Ref. 26). The calculations were begun with the particle in the potential core region of the jet moving at the jet fluid velocity. Predictions of the mean particle velocity on the nozzle centerline are compared with experimental results in Fig. 35. As shown, the agreement is quite good. Comparisons of predicted and measured particle diffusivities, defined by

$$\epsilon_{pr} = \frac{1}{2} \frac{d}{dt} \overline{(r_p - \bar{r}_p)^2} \quad (100)$$

are shown in Fig. 36. Agreement is again quite good, especially considering that the time derivative of a statistically determined quantity is being compared.

Calculations were then made for particles in the size range of interest for velocimetry. The calculations were made in the near region of the jet ($x/D < 12.0$) to minimize the time step required in the numerical calculation and off centerline in the region of maximum Reynolds shear. Results are shown in Fig. 37. The general trends at all x locations are the same; the mean velocity ratio approaches one first as the Stokes number increases, followed by the ratio of the longitudinal turbulent stresses, the ratio of the lateral turbulent stresses, and finally the ratio of the Reynolds shear. These calculations are for 5.0-, 2.5-, 1.0-, 0.25-, and 0.1- μm water particles in regions of the flow where the turbulence intensity is about 20 percent. The particles are less responsive at $x/D = 8.57$, because the magnitude of the velocity fluctuations is approximately 50 percent higher there.

The effect of particle dynamics can be seen in the velocity correlograms shown in Fig. 38. As the particle size increases, the ellipse begins to shrink and to rotate so that the principle axes align with the mean flow direction. This corresponds to an underprediction of turbulence quantities, which worsens as the particle size increases.

The calculations indicate that a water particle of maximum diameter of 0.25 μm is required to make reasonably accurate turbulence measurements in this flow field (reasonably accurate being defined as the size for which all the turbulence quantity particle to fluid ratios are better than 98 percent), whereas a 2.5- μm water droplet will yield acceptable results for the mean velocity. Figure 39 indicates that the product of the Stokes number and the integral time scale must be greater than 200 for meaningful turbulence measurements in this flow field.

5.3 MULTIMODAL TURBULENCE

The turbulence model developed here is based on an analytical representation of the time-averaged flow field that is consistent with a single normal mode representation of turbulence, but it is not always consistent with actual LV measurements of turbulence. This can be seen in the two stream-mixing measurements made with the LV reported in Ref. 1. The velocity correlogram was shown to be bimodal (dumbbell-shaped) with two distinct velocity modes representing the high-speed and the low-speed streams. The two modes begin to coalesce as the mixing region more fully develops and eventually become one mode far downstream. In

the early region of the mixing zone the maximum Reynolds shear is very large, because the stress ellipse has a very long major axis and a short minor axis. This is true even if the individual components of the dumbbell are isotropic. If the particle lag effects on mean velocity are negligible (as was shown in Ref. 1), then the mean velocity of each component of the dumbbell is accurately determined. As a result both the major axis, u_{10} , and the angle, θ , of the stress ellipse (Fig. 11) are accurately determined. Only the minor axis, u_{20} , of the stress ellipse is sensitive to particle lag and would be underpredicted if the particles were too large to follow the turbulence. The Reynolds shear in the mean flow direction is

$$\overline{u_1 u_2} = \frac{(\overline{u_{10}^2} - \overline{u_{20}^2})}{2} \sin 2\theta \quad (101)$$

and will be overpredicted when particle dynamics effects are present.

The weighting of the individual components of the dumbbell was shown to be a function of the respective individually controlled seed rate present in each stream in Ref. 1. The correct weighting, or intermittency, of the velocity modes cannot be determined from LV data alone. To properly model this flow, an independent measurement of the fluid intermittency would be required.

6.0 APPROXIMATIONS FOR PARTICLE RESPONSE TO TURBULENCE

The previous results indicate that quite small particles may be required to obtain accurate turbulence measurements with the LV in all but very low-speed flows. It would be useful to know what size particle is required for a specific flow field to aid in pretest planning and posttest analysis of LV data. The numerical method described in Sections 4.0 and 5.0 is not a convenient tool for general velocimeter applications since the majority of the required flow-field and turbulence information is not known a priori. Hence, some methods of approximating the particle response to turbulence would be useful in practical application. Two possible techniques will be discussed in this section.

6.1 SPECTRAL CUTOFF FREQUENCY APPROXIMATION

The work of Hjelmfelt and Mockros (Ref. 2) discussed in Section 2.0 offers one method of approximation. This method is based on the ability of a particle to respond to the highest frequency present in a turbulent flow field. The highest frequency in the Eulerian time spectrum can be approximated by (Ref. 22)

$$\omega_o = \left(\frac{U}{3}\right)^{1/2} \eta^{-1} \quad (102)$$

where

$$\eta = (\nu^3/\epsilon)^{1/4} \quad (103)$$

The dissipation, ϵ , can be approximated by (Ref. 3)

$$\epsilon = \frac{(0.09)^{3/2} U^2}{40 \nu} \quad (104)$$

The frequency parameter may be defined as

$$N_{fo} = 4.315 \frac{\nu}{d \sqrt{U}} \quad (105)$$

or, in terms of the Stokes number,

$$N_{fo} = 0.719 \sqrt{\frac{\nu N_s (2S + 1)}{U}} \quad (106)$$

The particle response can then be found from Eq. (13) for various size and weight particles.

6.2 SIMPLE TURBULENCE MODEL APPROXIMATION

Meek and Jones (Ref. 32) present a method of predicting the response of heavy particles to turbulence based on a simple isotropic turbulence. This simple model is valid when the particles are much more dense than the fluid and when the particles are small enough for Stokes law to apply. Their equation is

$$\frac{\overline{v'^2}}{\overline{u'^2}} = \frac{1}{1 + \epsilon_{11}} \quad (107)$$

where

$$\epsilon_{11} = \frac{d^2 (2S + 1)}{180 T_{E1}} = \frac{2}{N_s T_{E1}} \quad (108)$$

Substituting into Eq. (62) for T_{E1} , ϵ_{11} becomes

$$\begin{aligned} \epsilon_{11} &= 8.436 \times 10^{-5} \frac{U d^2 (2S + 1)}{A \nu^2} \\ &= 3.037 \times 10^{-3} \frac{U}{A \nu N_s} \end{aligned} \quad (109)$$

The particle response can then be approximated from Eq. (107) for various size and weight particles. This equation is essentially a form of the product of the integral time scale and the Stokes number, which forms a nondimensional quantity that was shown to correlate the particle response results well in Section 5.0.

6.3 APPLICATIONS OF THE APPROXIMATION TECHNIQUES

Both techniques were applied to the grid-generated turbulence and the axisymmetric jet examples discussed, as described in Section 5.0. Results for the grid turbulence are shown in Fig. 40; jet results are shown in Fig. 41. These results indicate that the method of Meek and Jones better represents the predicted trend of particle response with decreasing Stokes number. The method of Hjelmfelt and Mockros predicts a much greater loss of response with decreasing Stokes number than actually exists. Both methods yield about the same value of Stokes number for turbulent intensity ratios of 0.99. Both methods underpredict the correct minimum value for the grid case, whereas they both predict the correct minimum Stokes number for the jet. For the cases presented, the method of Meek and Jones seems to be adequate for "rule of thumb" approximations of the expected particle response to turbulence and for estimating LV data quality.

7.0 SUMMARY

A numerical model for evaluating seed particle requirements for accurate turbulence measurements with the laser velocimeter has been developed. The particle equation of motion was carefully analyzed and the importance of including the Basset history integral noted. A Monte Carlo turbulence model was developed, which included an elementary description of the internal structure of an eddy. When these models were applied to simple flow fields to evaluate particle dynamics effects on LV turbulence measurements, two important conclusions were reached.

The first conclusion stems from an analysis of a particle size distribution present in a flow field with sufficient mean velocity gradients to cause the particles to lag the fluid velocity. The response of the individual particle sizes will lead to a broadening of the measured velocity distribution. This broadening can affect both the turbulent intensity and Reynolds shear measurements. These particle dynamics effects also point to limitation of the velocimeter for obtaining turbulence information in the region immediately behind shocks or in other flows with large velocity gradients.

Secondly, particles that are capable of tracking the mean flow may not be adequate for measuring turbulence quantities. Large monodisperse particles will cause the turbulence

quantities to be underpredicted. As the particle diameter or density decreases, the fluid mean velocity will be reproduced first, followed by the longitudinal turbulent stress, the lateral turbulent stress, and finally the Reynolds shear. It is anticipated that the higher order the turbulence correlation parameter, the more sensitive the measurement will become to particle dynamics.

Calculations were made for two simple turbulent flows, grid-generated turbulence and a subsonic axisymmetric jet. The Stokes number was shown to be a reasonable correlation parameter for particle diameter and density effects. It was found that the product of the Stokes number and the turbulence integral time scale (which is equivalent to the ratio of the turbulence integral time scale to the particle response time) must be of order 1000 for grid-generated turbulence and 200 for the jet turbulence for meaningful turbulence measurements with the LV. This leads to a requirement for submicron particles for most applications of the LV. Approximation techniques for particle response to turbulence were developed for "rule of thumb" type applications.

It is interesting to note that the particle-induced errors associated with the LV have a cancelling effect. The mean flow particle lag leads to a broadening of the measured velocity distribution when a particle size distribution is present, whereas large particles will under-respond to the actual fluid turbulence. In complex flow fields, both of these effects may be occurring, and care should be taken to assure that measurements that appear reasonable are not the result of a fortuitous interaction between these competing particle dynamics effects.

Several recommendations for future work in this area can be made. There is a very limited data base for particle response to turbulence. Carefully controlled experiments in known, well-documented flow fields with smaller size particles would aid in verifying this code and improving the turbulence model. Numerical improvements in the particle equation-of-motion solver, such as the use of a stiff system equation solver and faster integration techniques in the evaluation of the Basset history integral, would reduce the cost and manual intervention required for solutions with this code.

F. L. Heltsley's study (Ref. 1) included bimodal results in the initial region of a jet/base and a free-stream/base shear layer. The bimodal nature of the velocity distributions is quite pronounced near the jet exit and subsides as the mixing region grows. The separate velocity modes form a "dumbbell" when plotted in velocity space, each mode containing a distinct mean and turbulence level consistent with fluid streams present on either side of the shear layer. The mean velocity and turbulence levels associated with a point in the shear layer are generated by processing the velocity data for both modes, giving a somewhat distorted view of the actual fluid behavior. The relative size of the modes could be controlled by regulating

the amount of seed introduced to each stream individually. This creates a perplexing situation since the mean and turbulence measurements with the LV become a function of the seed rate from the two seeders. Further work is required to assure that the multimodal measurements are real and not particle-induced and to develop data sampling techniques for obtaining LV measurements in such flows.

Finally, there are some other factors not discussed in this work that may also effect turbulence measurements with the LV, including machine (processor) broadening, preferential treatment by the processor, velocity biasing, and spurious noise in the measurement systems. A detailed study of these effects, coupled with this work, would establish the accuracy limits of turbulence measurements with the LV and aid in the interpretation of LV data.

REFERENCES

1. Heltsley, F. L., Walker, Billy J., and Nichols, Robert H. "Transonic Nozzle-Afterbody Flow Field Measurements Using a Laser Doppler Velocimeter." AGARD-CP-348, September 1983.
2. Hjelmfelt, A. T., Jr. and Mockros, L. F. "Motion of Discrete Particles in a Turbulent Fluid." *Applied Scientific Research*, Vol. 16, 1966, pp. 149-161.
3. Shuen, J-S. et al. "A Theoretical and Experimental Study of Turbulent Particle-Laden Jets." NASA CR 168293, November 1983.
4. Ormancey, A. and Martinon, A. "Numerical Simulation of Particle Behavior in a Turbulent Flow." *Research Aerospace*, 1983, pp. 21-30.
5. Basset, A. B. *Treatise on Hydrodynamics*. Deighton Bell, London, 1888.
6. Boussinesq, J. *Theorie Analytique de la Chaleur*. L'Ecole Polytechnique, 1903.
7. Oseen, C. W. *Hydrodynamik*. Leipzig, 1927.
8. Tchen Chan-Mou. *Mean Value and Correlation Problems Connected with the Motion of a Small Particle Suspended in a Turbulent Fluid*. Thesis, Delft, 1947.
9. Corrsin, S. and Lumley, J. "On the Equation of Motion for a Particle in a Turbulent Fluid." *Applied Scientific Research*, Section A, Vol. 6, 1956, pp. 114-116.

10. Beuvich, Y. A. "Motion Resistance of a Particle Suspended in a Turbulent Medium." *Fluid Dynamics*, Vol. 1, No. 6, 1966, p. 119.
11. Soo, S. L. "Equation of Motion of a Solid Particle Suspended in a Fluid." *Physics of Fluids*, Vol. 18, No. 2, February 1975, pp. 263-264.
12. Gitterman, M. and Steinberg, V. "Memory Effects in the Motion of a Suspended Particle in a Turbulent Fluid." *Physics of Fluids*, Vol. 23, No. 11, November 1980, pp. 2154-2160.
13. Maxey, Martin R. and Riley, James J. "Equation of Motion for a Small Rigid Sphere in a Nonuniform Flow." *Physics of Fluids*, Vol. 26, No. 4, April 1983, pp. 883-889.
14. Forney, L. J., Walker, A. E., and McGregor, W. K. "Effect of the Basset Term on Particle Relaxation Behind Normal Shock Waves." AFOSR-TR-84-0747 (AD-A145446), July 1984.
15. Ho, B. P. and Leal, L. G. "Inertial Migration of Rigid Spheres in Two-Dimensional Unidirectional Flows." *Journal of Fluid Mechanics*, Vol. 625, Part 2, August 1974, pp. 365-400.
16. Saffman, P. G. "The Lift on a Small Sphere in a Slow Shear Flow." *Journal of Fluid Mechanics*, Vol. 22, Part 2, June 1965, pp. 385-400.
17. Odar, F. and Hamilton, W. S. "Forces on a Sphere in a Viscous Fluid." *Journal of Fluid Mechanics*. Vol. 18, Part 2, February 1964, pp. 302-314.
18. Karanfilian, S. K. and Kotas, T. J. "Drag on a Sphere in Unsteady Motion in a Liquid at Rest." *Journal of Fluid Mechanics*, Vol. 87. Part 1, July 1978, pp. 85-96.
19. Bailey, A. B. and Hiatt, J. "Sphere Drag Coefficients for a Broad Range of Mach and Reynolds Numbers." *AIAA Journal*, Vol. 10, No. 11, November 1972, pp. 1436-1440.
20. Golovin and Fominysk. "Motion of a Spherical Particle in a Viscous Non-Isothermal Fluid." *Akademiia Nauk SSSR, Ivetiia, Mekhanika Zhidkostii Gaza*, January-February 1983.
21. Crowe, C. T. "Drag Coefficient of Particles in a Rocket Nozzle." *AIAA Journal*, Vol. 5, No. 5, May 1967, p. 1021.
22. Tennekes, H. and Lumley, J. L. *A First Course in Turbulence*. MIT Press, Cambridge, Massachusetts, 1972.

23. Hinze, J. O. *Turbulence*. McGraw-Hill, New York, 1959.
24. Rubinstein, Reuven V. *Simulation and the Monte Carlo Method*. Wiley and Sons, Inc., New York, 1981.
25. Snyder, W. H. and Lumley, J. L. "Some Measurements of Particle Velocity Autocorrelation Functions in a Turbulent Flow. " *Journal of Fluid Mechanics*, Vol. 48, Part 1, July 1971, pp. 41-71.
26. Yuu, Sinichi et al. "Particle Turbulent Diffusion in a Dust Laden Round Jet. " *AICHE Journal*, Vol. 24, No. 3, May 1978, pp. 509-519.
27. Liepmann, H. W. and Laufer, J. "Investigation of Free Turbulent Mixing. " NACA TN 1257, August 1947.
28. Laurence, J. C. "Intensity, Scale, and Spectra of Turbulence in Mixing Region of Free Subsonic Jet. " NACA Report 1292, 1956.
29. Corrsin, S. and Uberoi, M. S. "Further Experiments on the Flow and Heat Transfer in a Heated Turbulent Air Jet. " NACA TN 1865, April 1949.
30. Wygnanski, I. and Fielder, H. "Some Measurements in the Self-Preserving Jet. " *Journal of Fluid Mechanics*, Vol. 38, Part 3, September 1969.
31. Chow, W. L. and Korst, H. H. "On the Flow Structure Within a Constant Pressure Compressible Turbulent Jet Mixing Region. " NASA TND-1894, April 1963.
32. Meek, Charles C. and Jones, Barclay G. "Studies of the Behavior of Heavy Particles in a Turbulent Fluid Flow. " *Journal of Atmospheric Sciences*, Vol. 30, No. 2, March 1973, pp. 239-244.

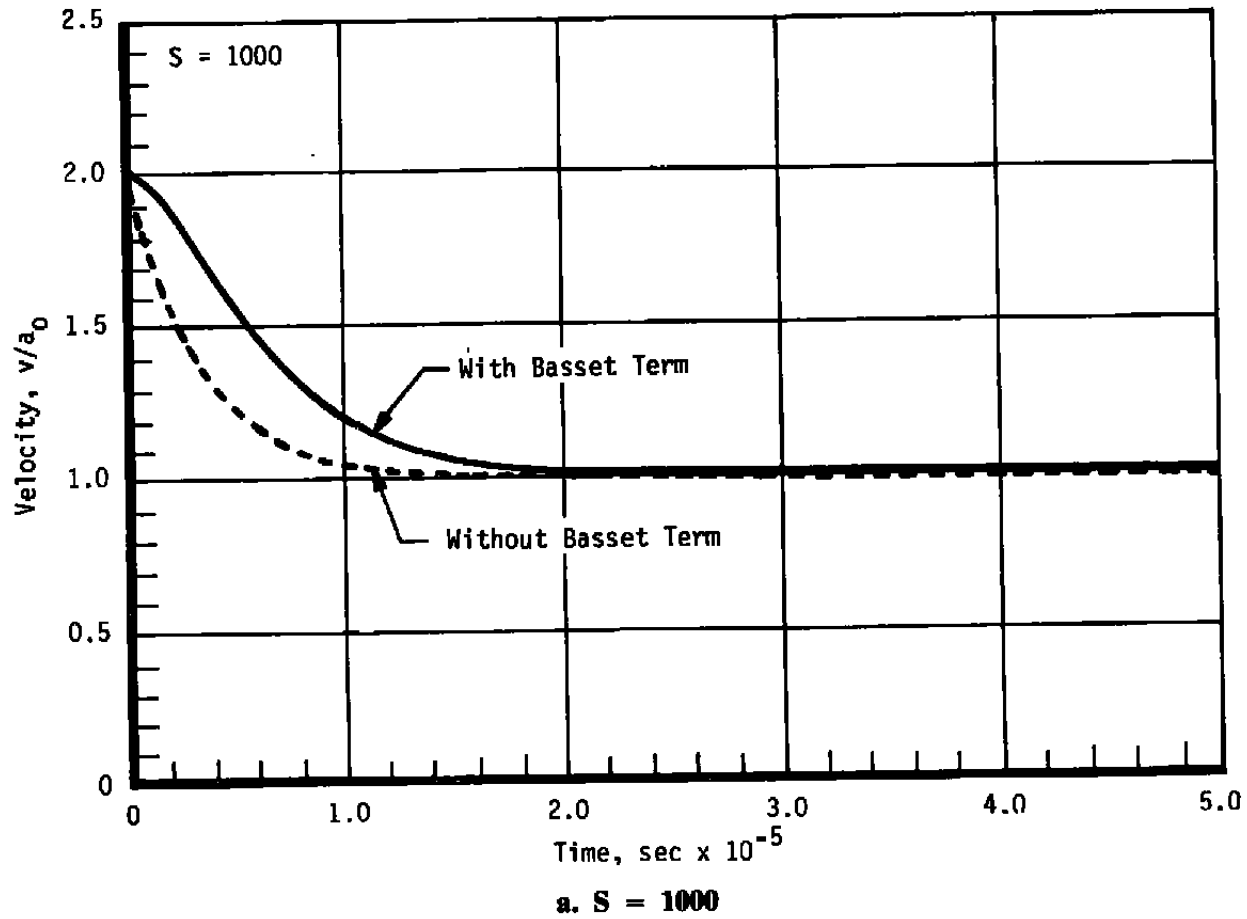
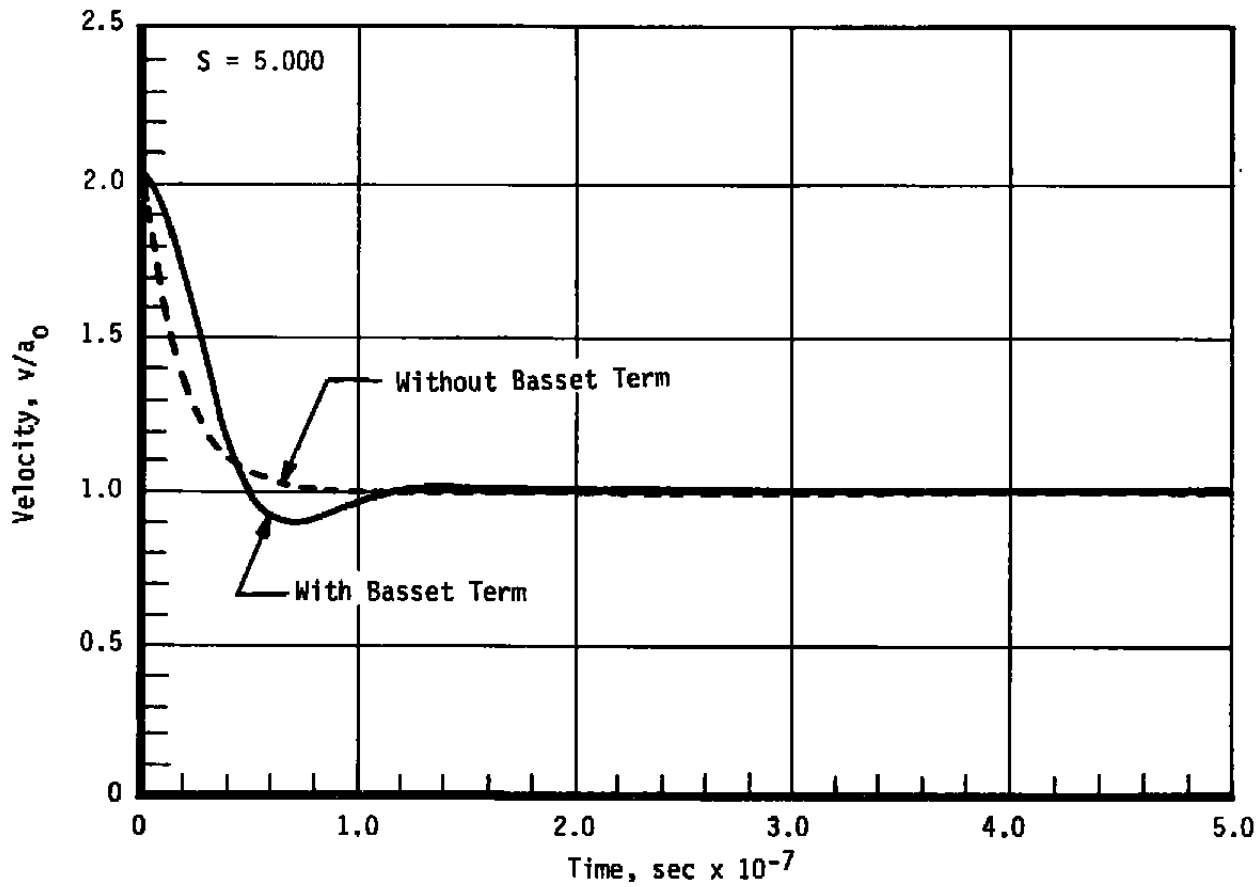
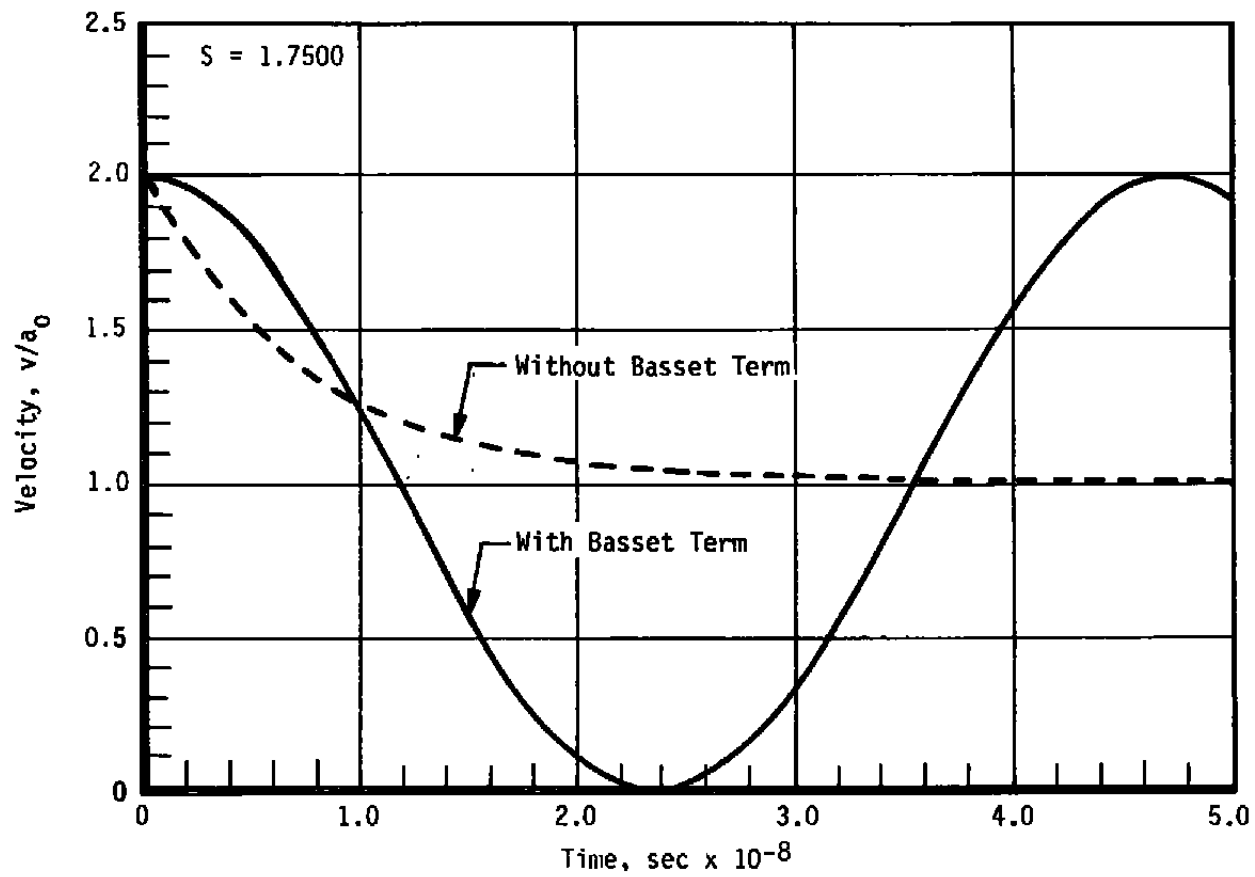


Figure 1. Particle response to a step change in fluid velocity.

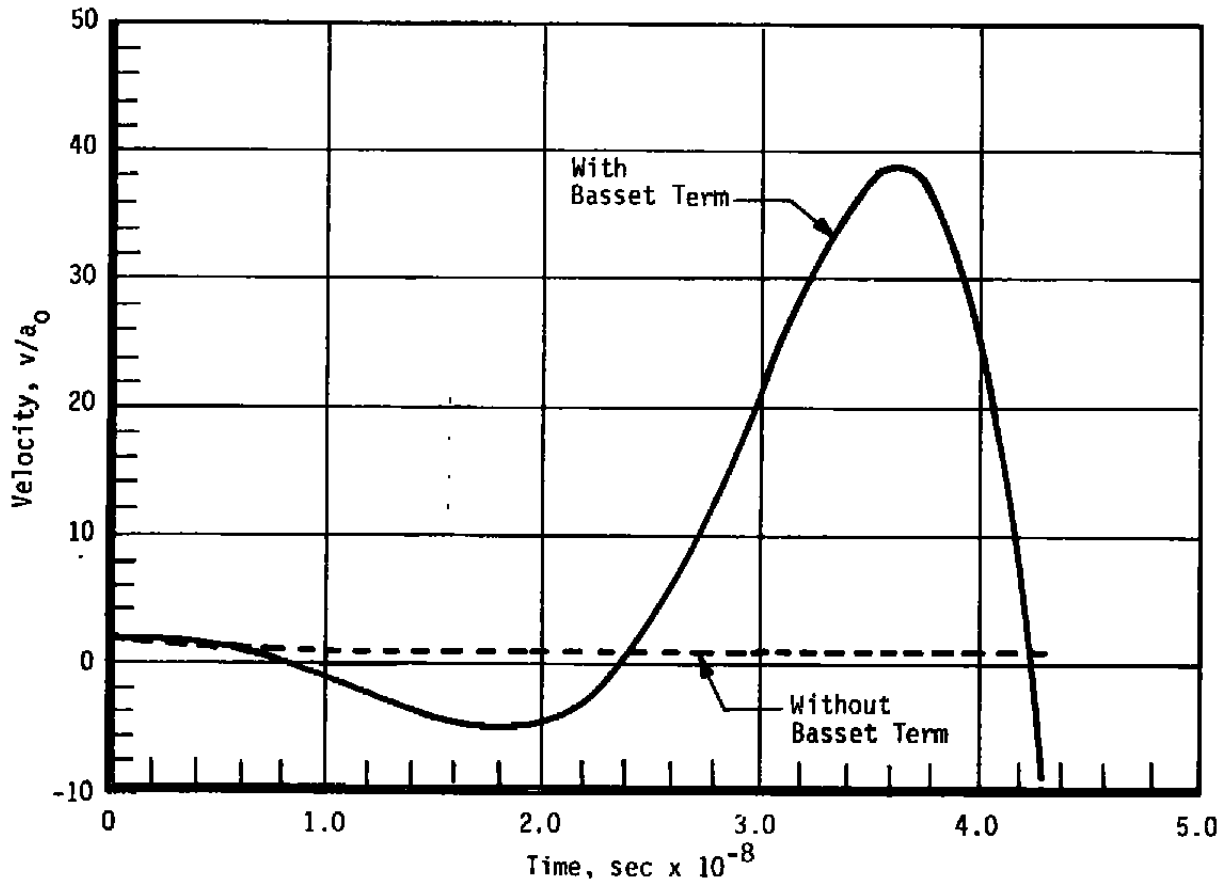


b. $S = 5$
Figure 1. Continued.



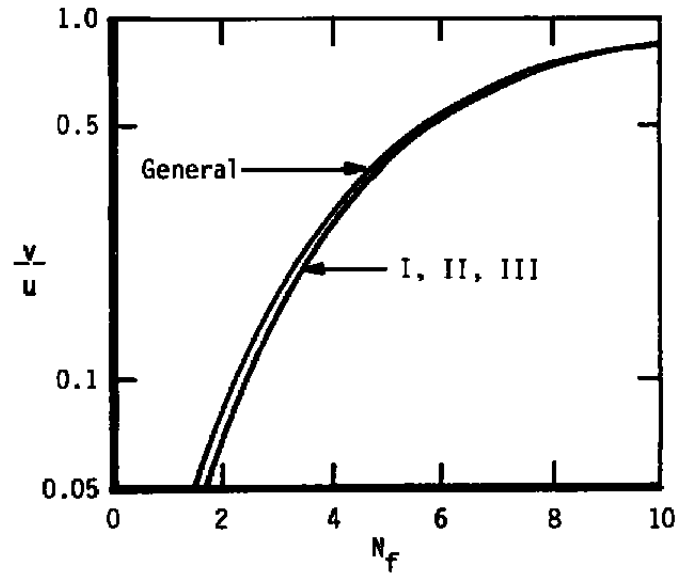
c. $S = 1.75$

Figure 1. Continued.

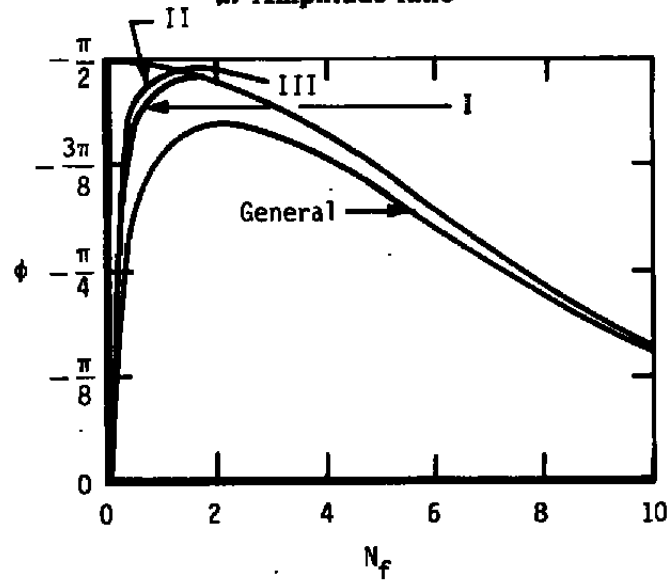


d. S = 1.0

Figure 1. Concluded.

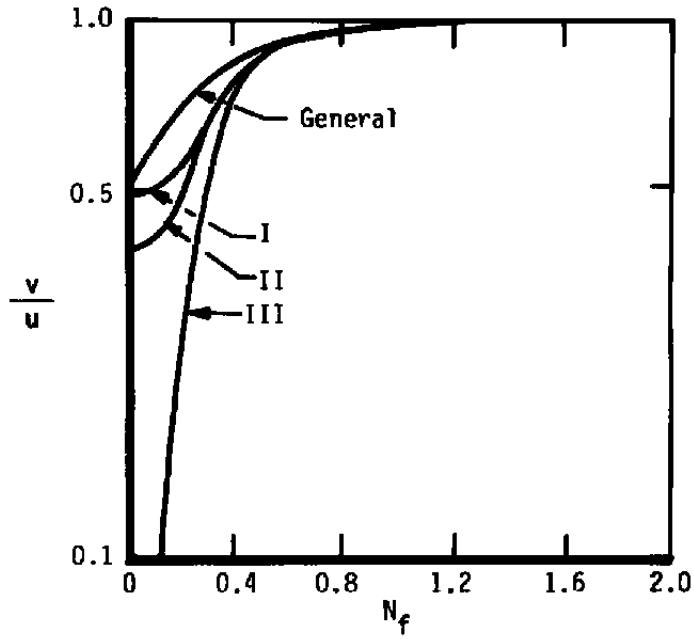


a. Amplitude ratio

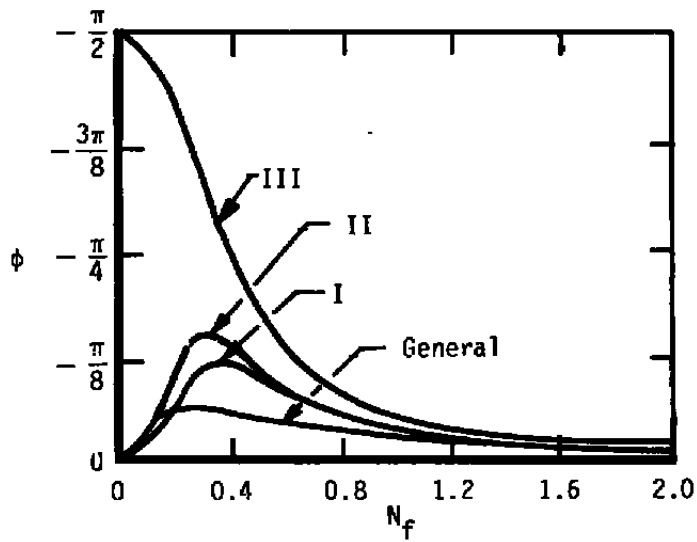


b. Phase angle

Figure 2. Particle response to a sinusoidal oscillation for $S = 1000$.



a. Amplitude ratio



b. Phase angle

Figure 3. Particle response to a sinusoidal fluid oscillation for $S = 2.65$.

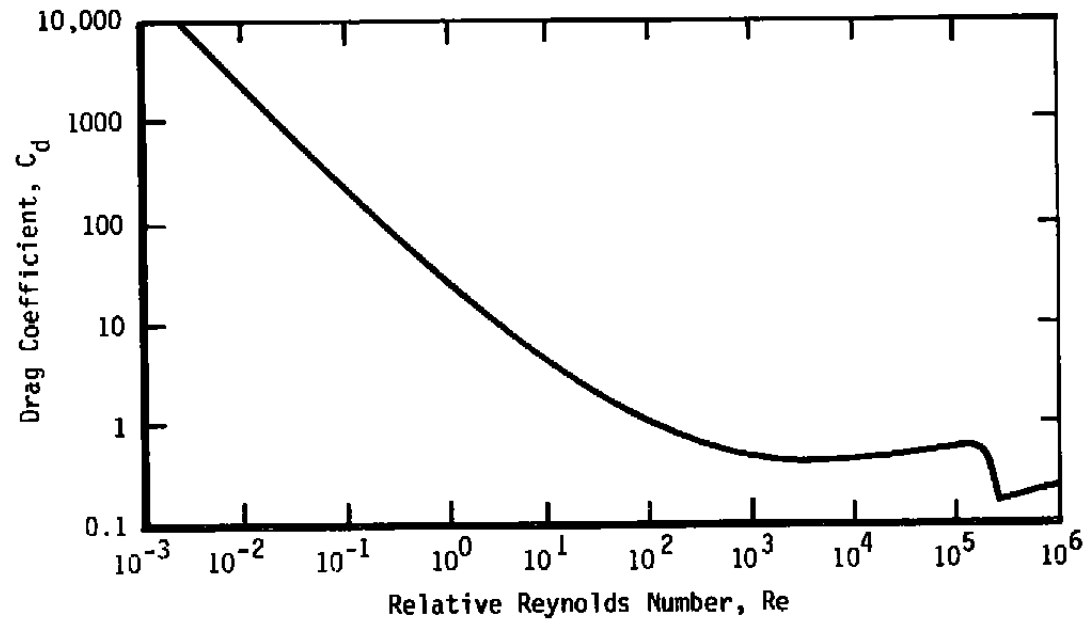


Figure 4. Standard incompressible drag curve for a sphere.

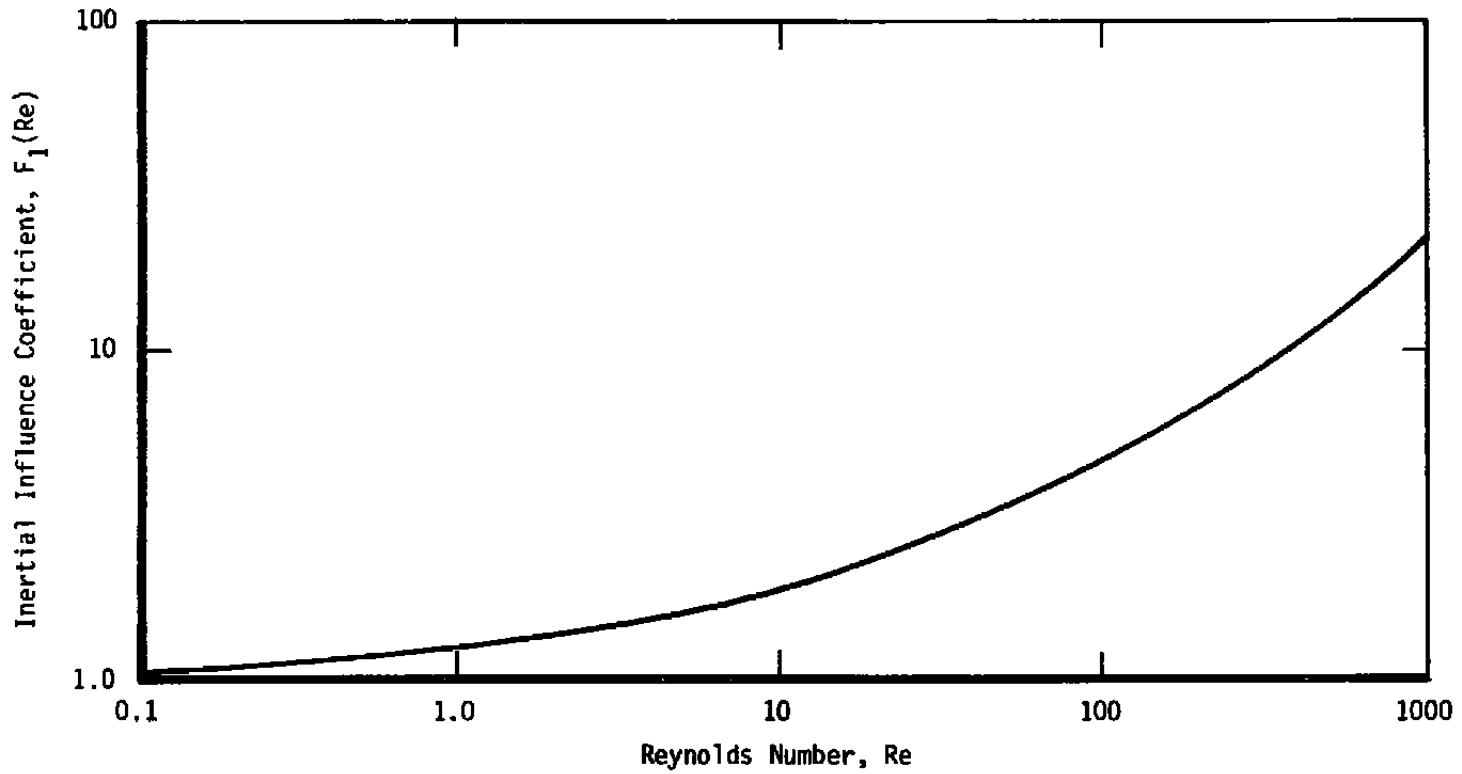


Figure 5. Correction to Stokes law for high relative Reynolds numbers.

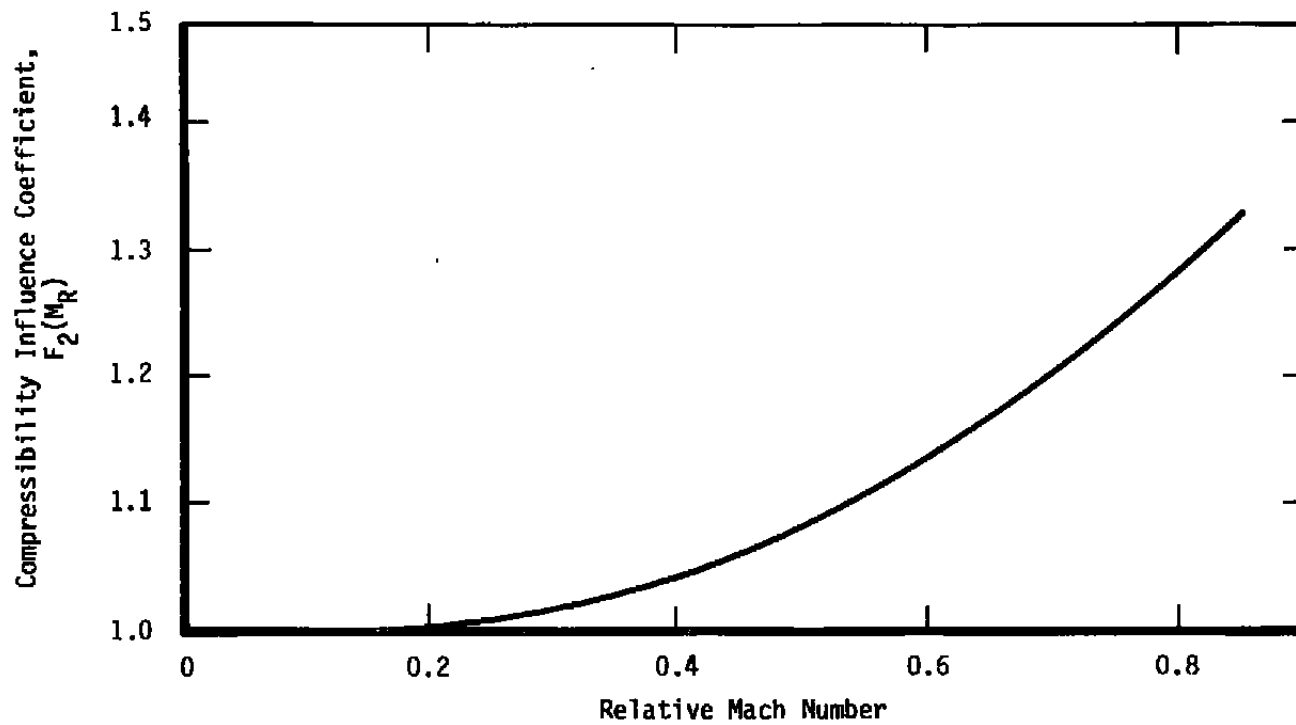


Figure 6. Empirical correction for subsonic compressibility effects.

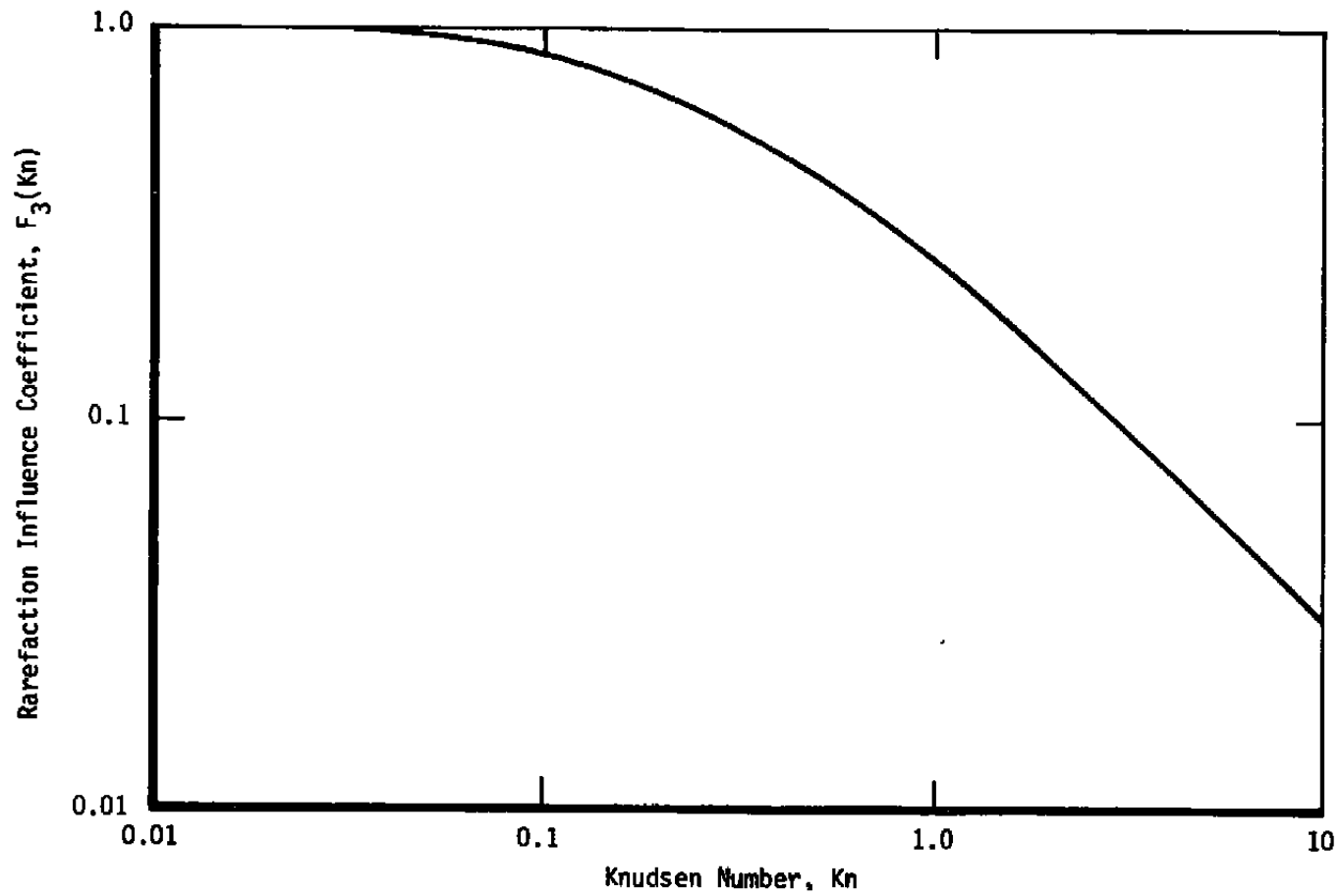


Figure 7. Empirical correction for rarefaction effects.

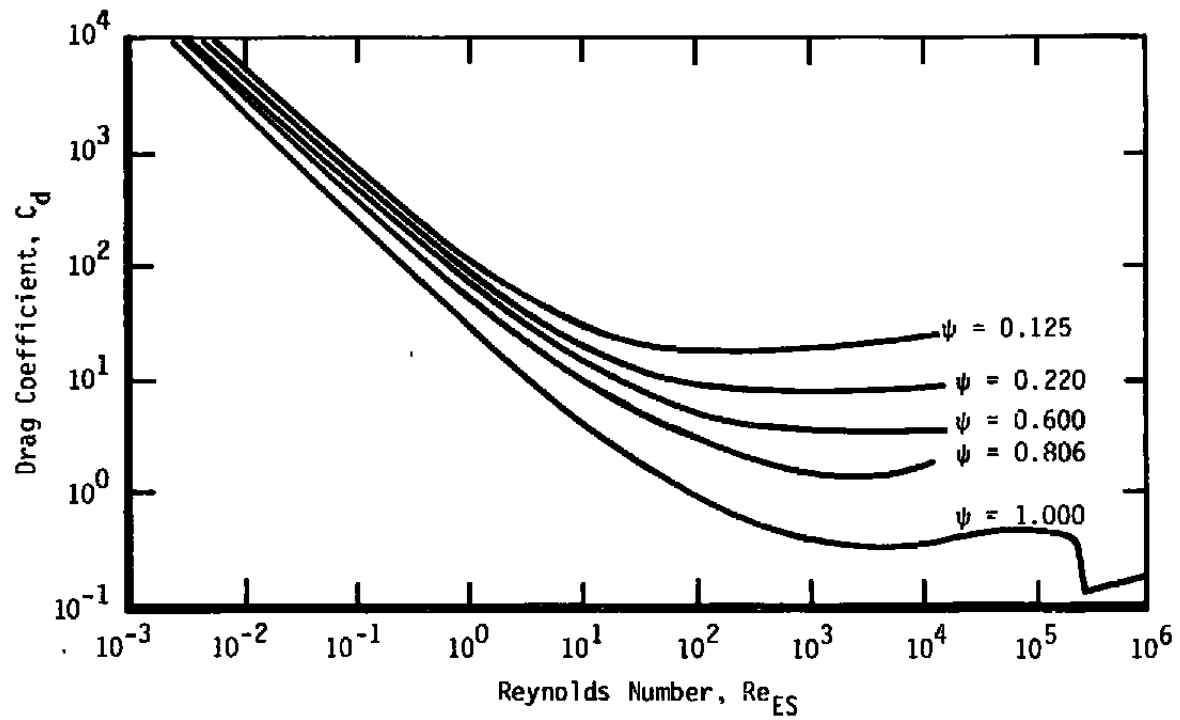


Figure 8. Drag coefficients for nonspherical particles.

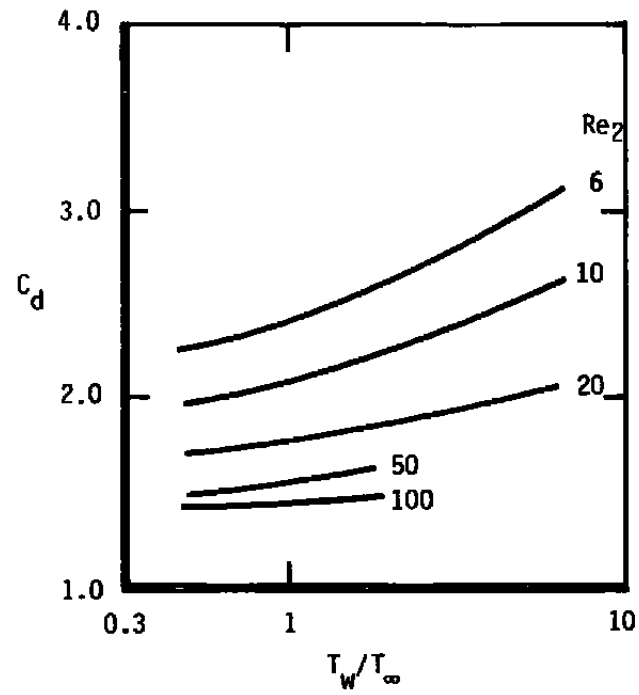


Figure 9. Variation of sphere drag coefficient with wall temperature for $M_R = 2.0$.

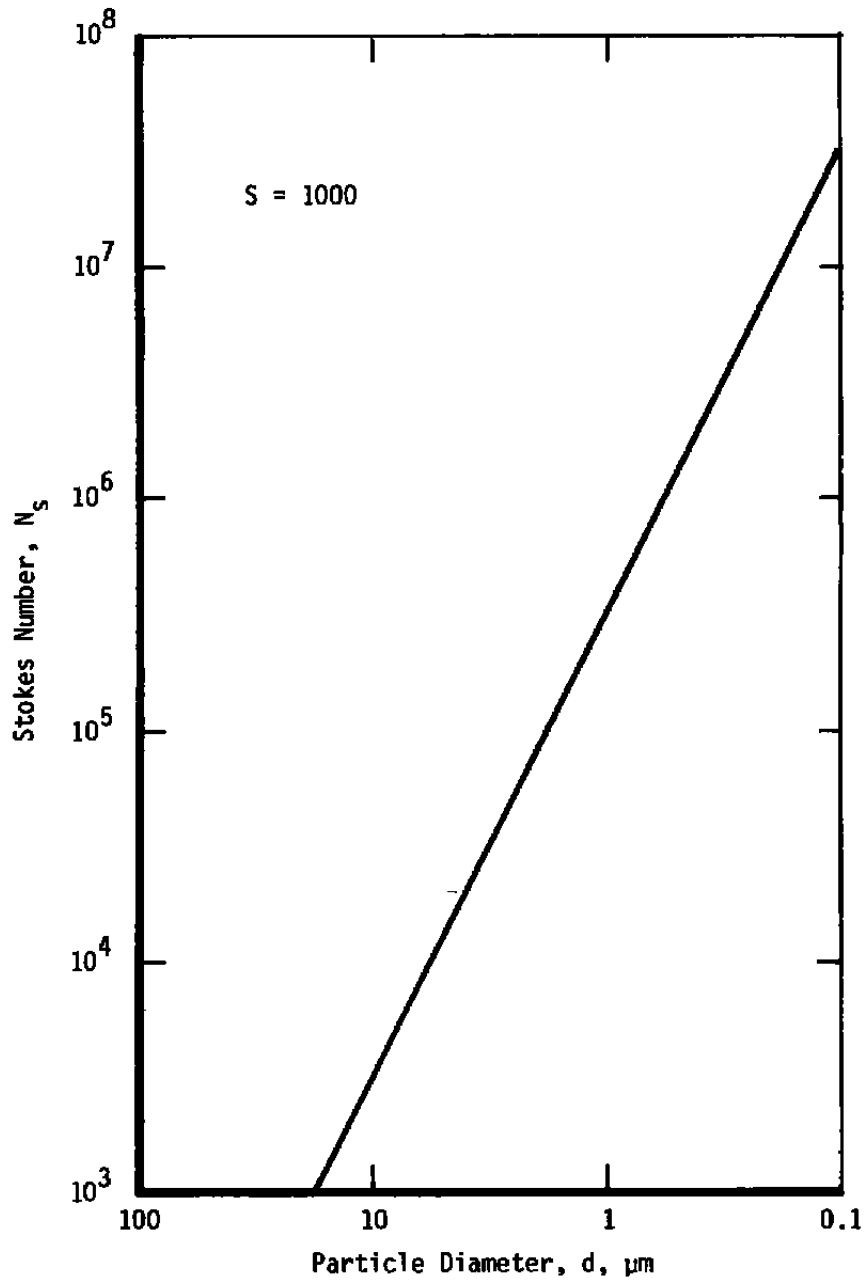


Figure 10. Increase in stiffness of the particle equation of motion with decreasing particle diameter.

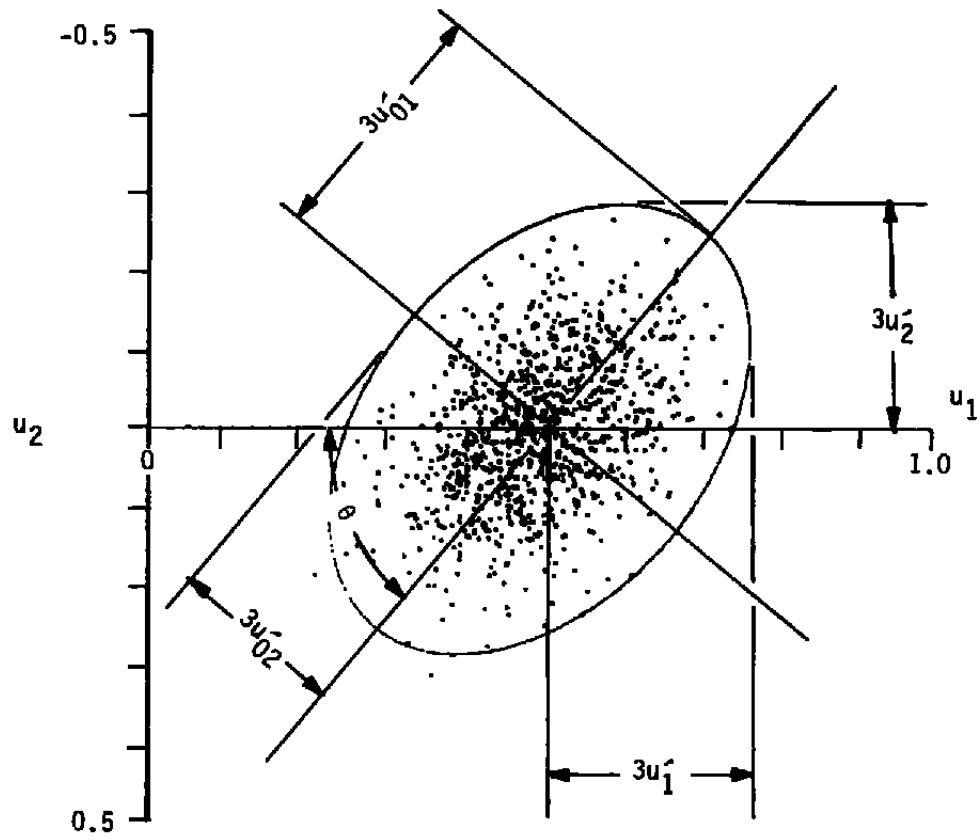


Figure 11. Typical velocity correlogram for the LV.

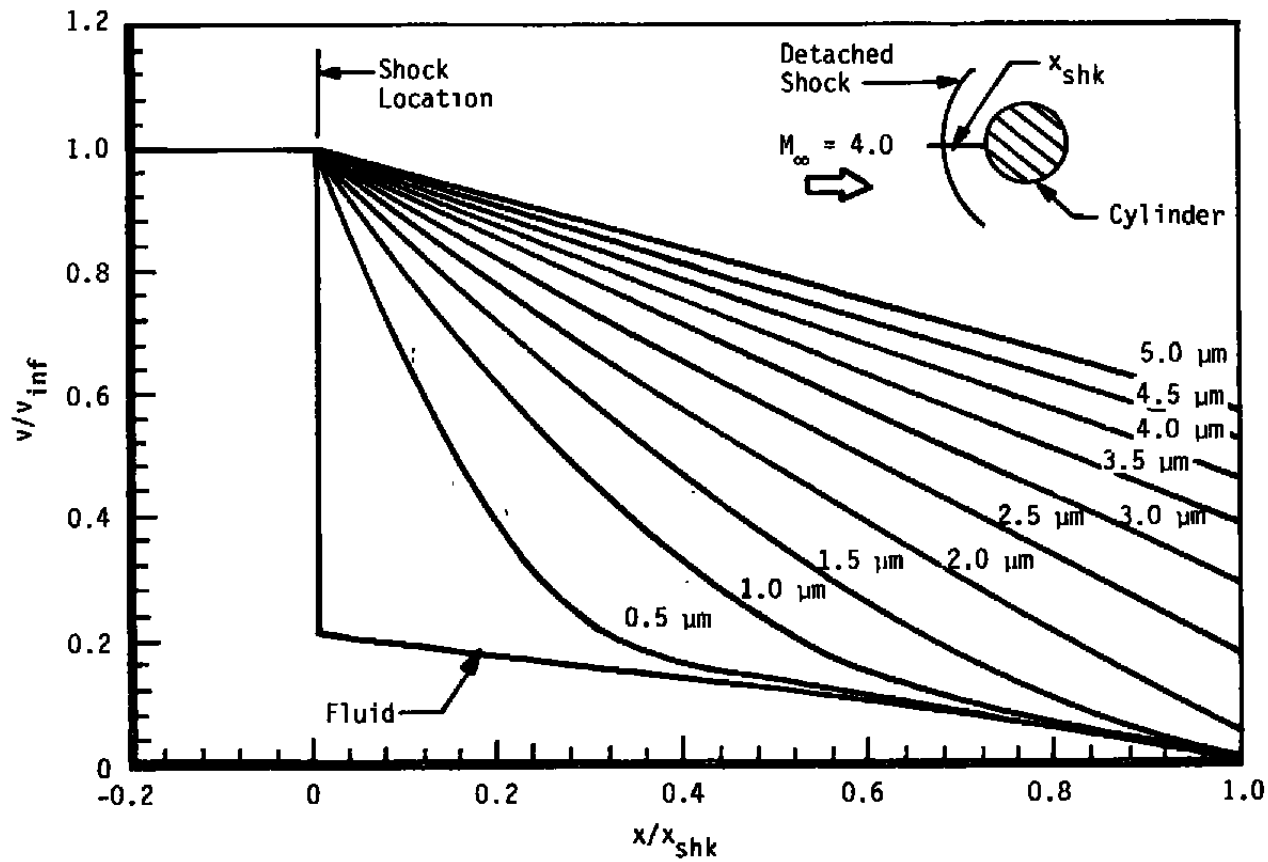


Figure 12. Theoretical olive oil particle response to a cylinder bow shock at $M_{\infty} = 4.0$ and $Re_D = 10^5$.

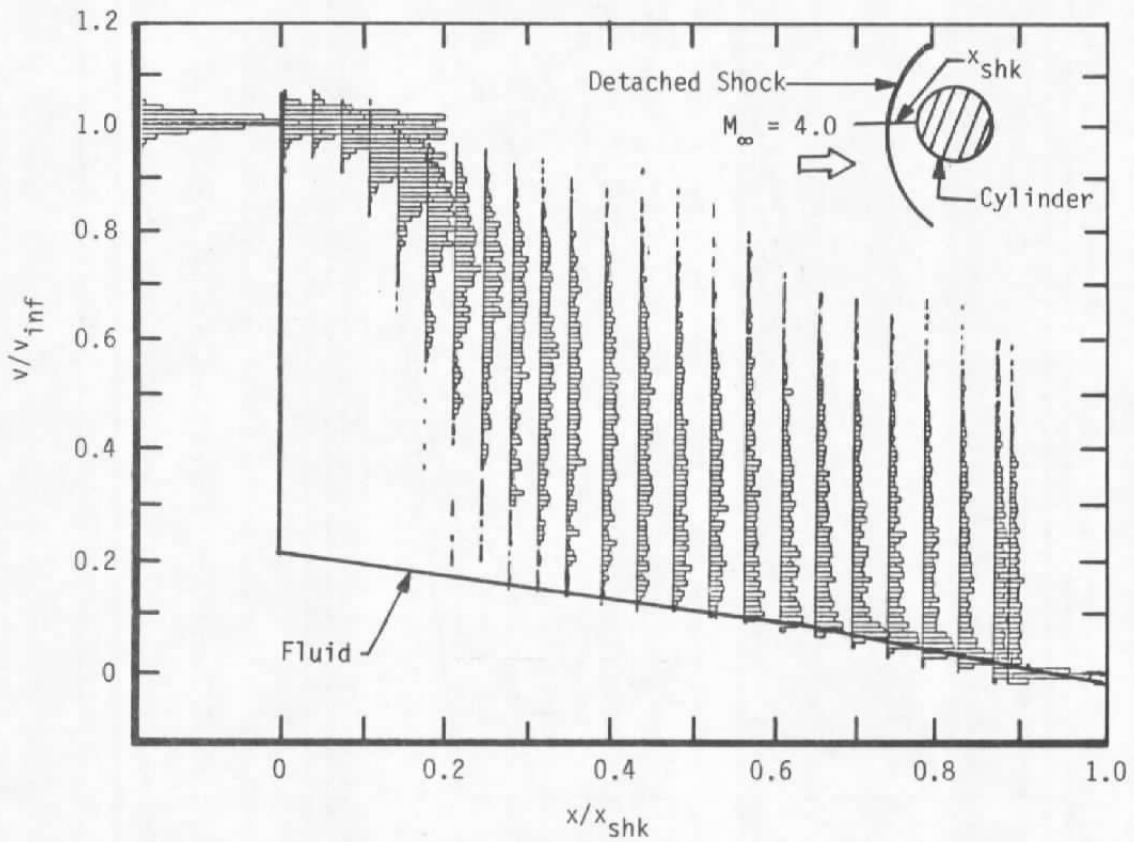


Figure 13. Measured LV velocity probability distributions for a cylinder bow shock at $M_{\infty} = 4.0$ and $Re_D = 10^5$.

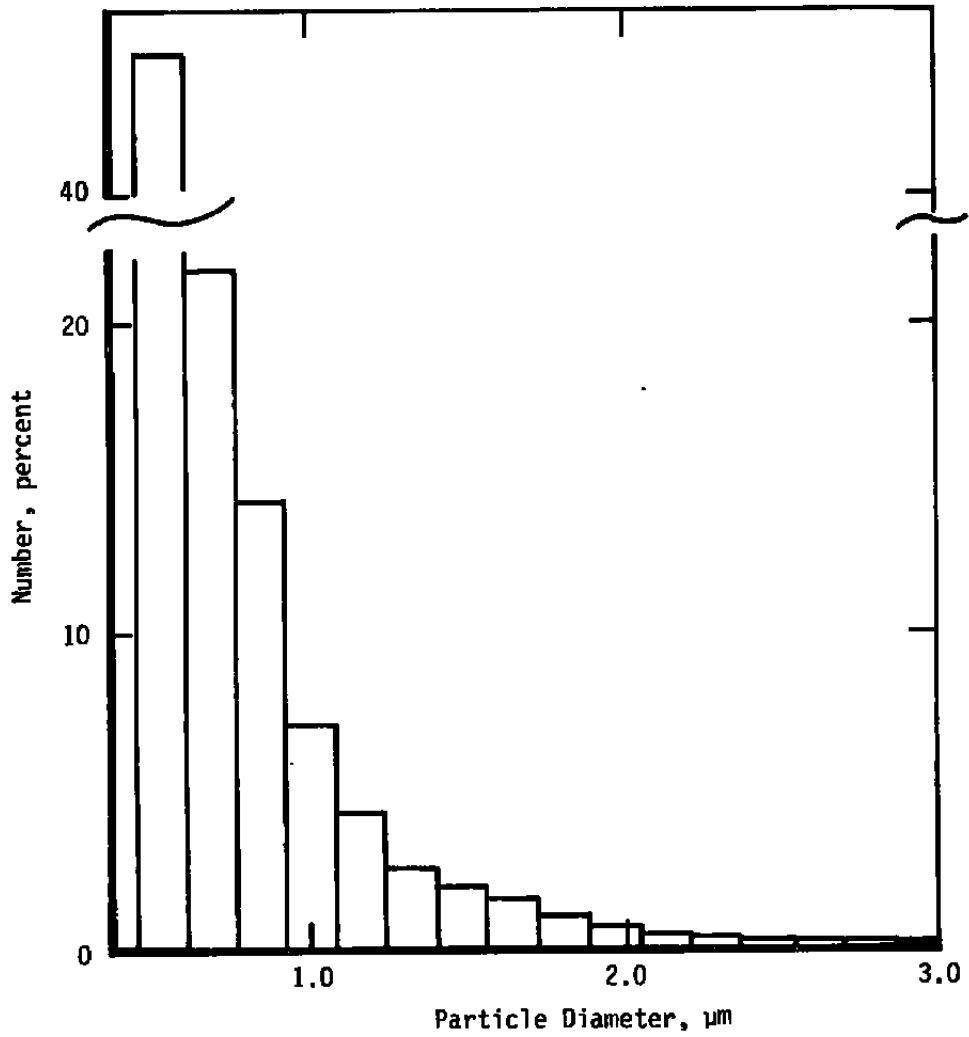
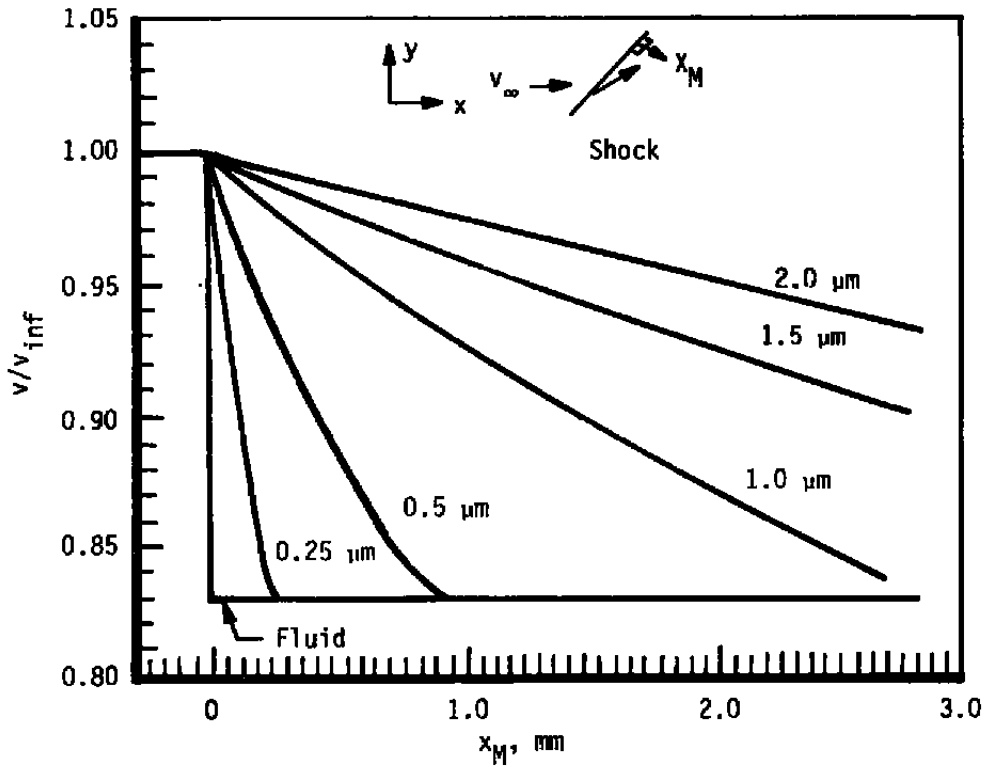
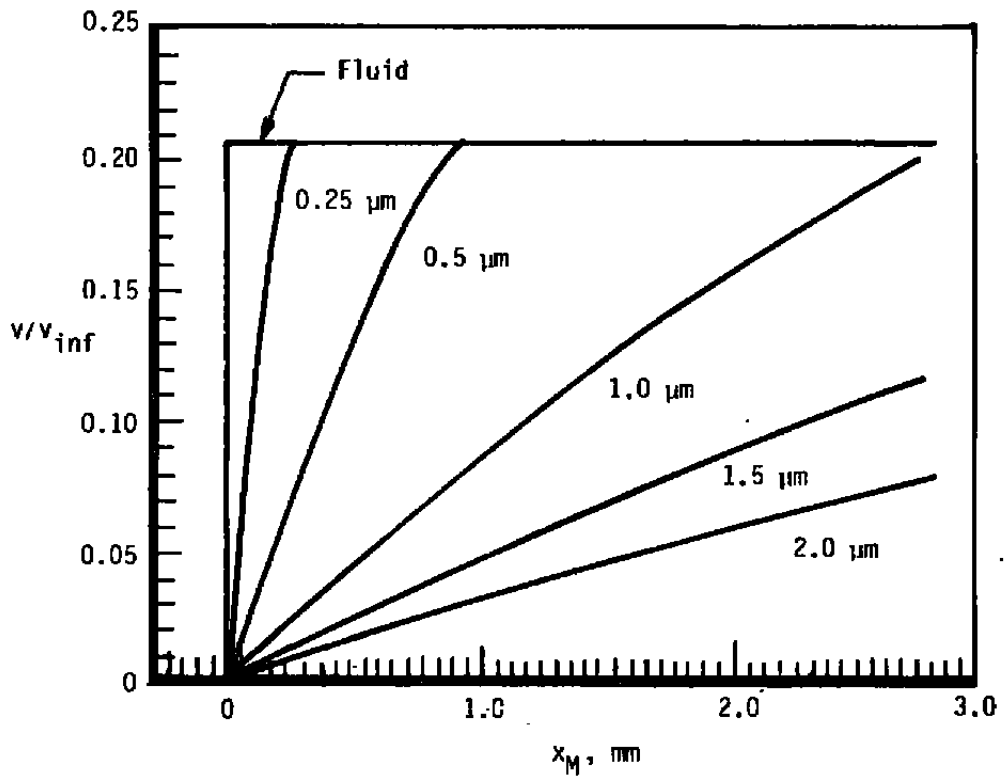


Figure 14. Particle size distribution for olive oil in a Collison Atomizer measured with an ASAS-X[®] Aerosol sampling unit.

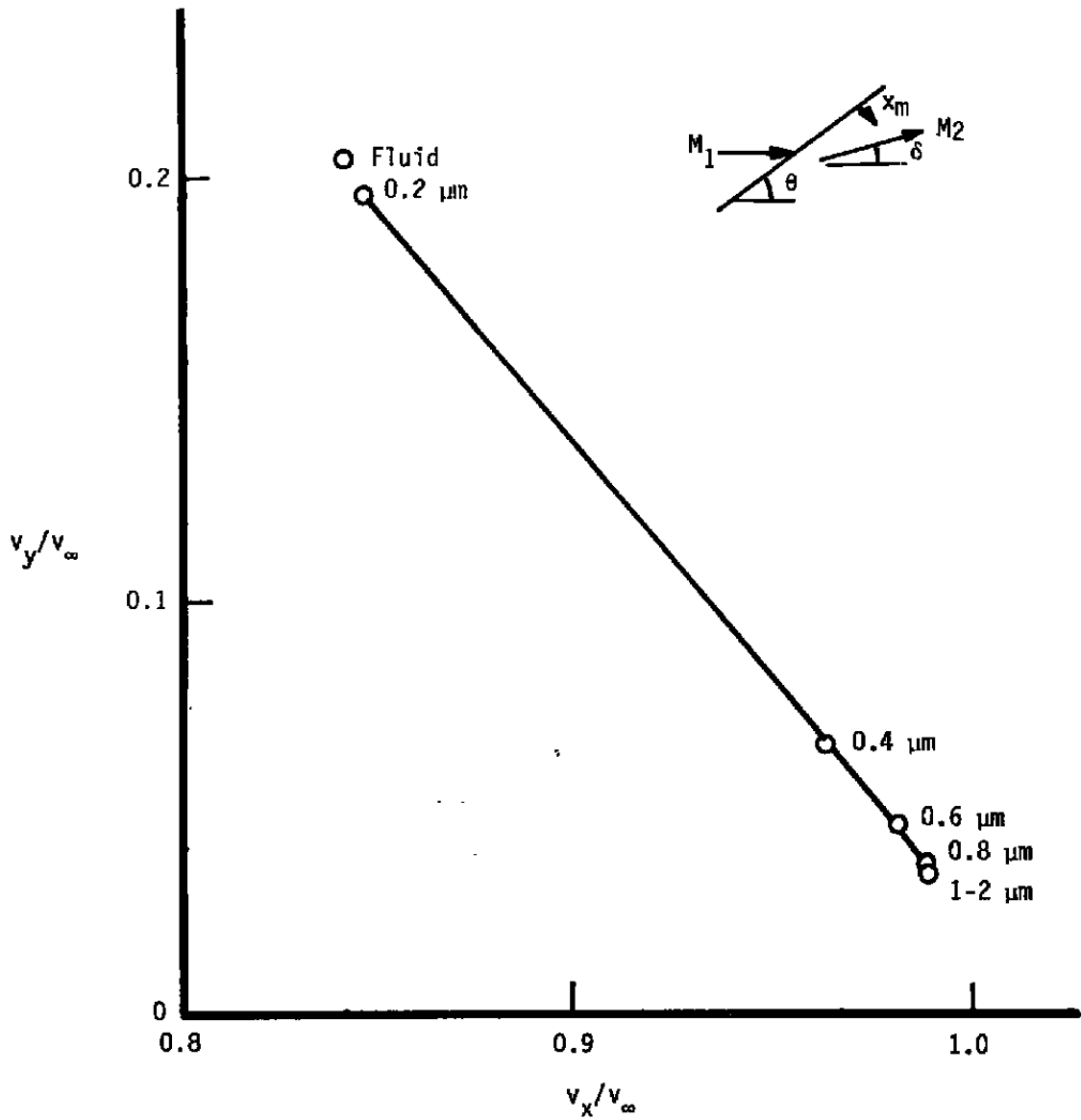


a. x Velocity

Figure 15. Particle relaxation behind an oblique shock at $M_\infty = 2.2$ and $Re = 4.4 \times 10^6/M$.

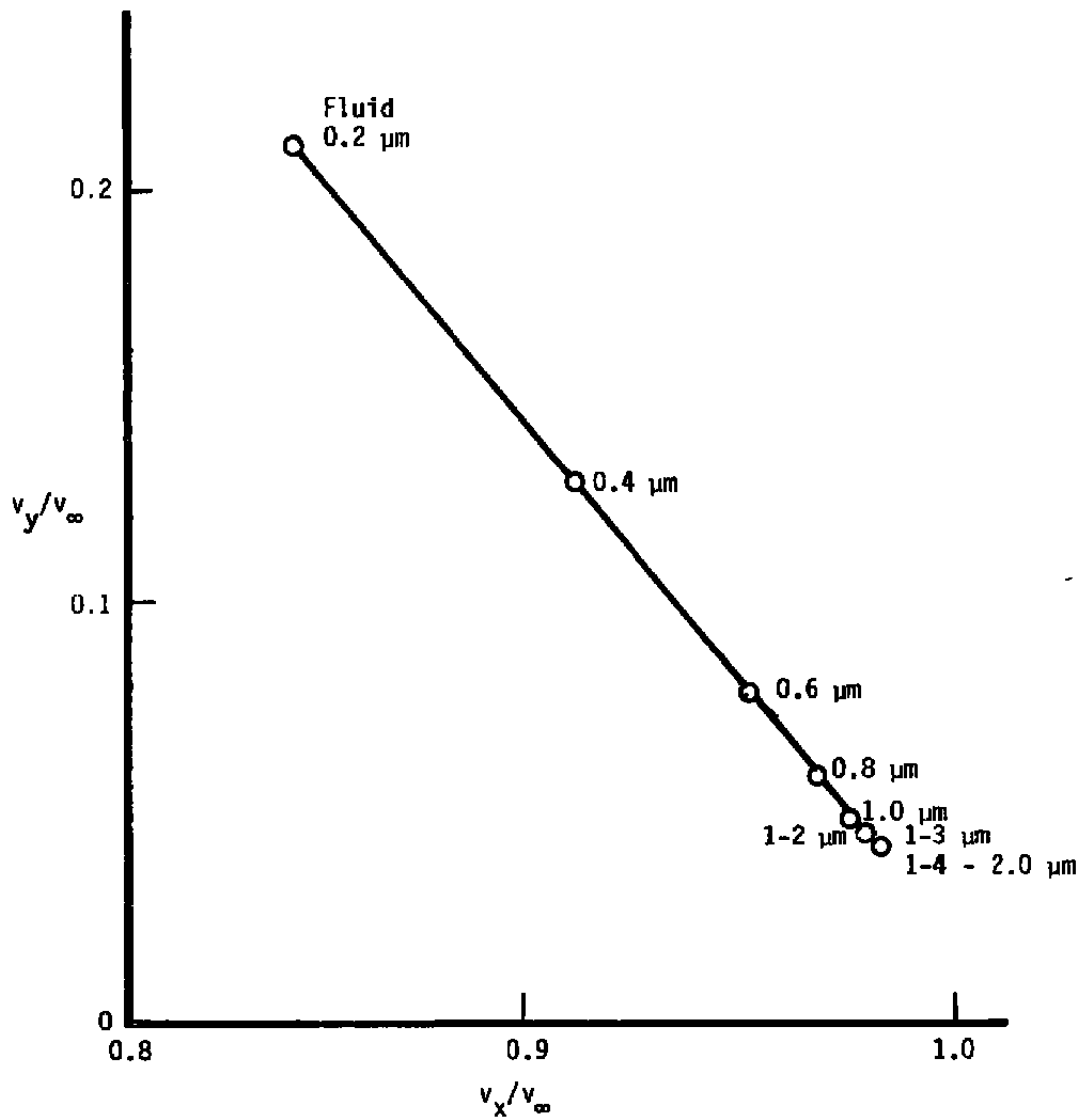


b. y Velocity
Figure 15. Concluded.

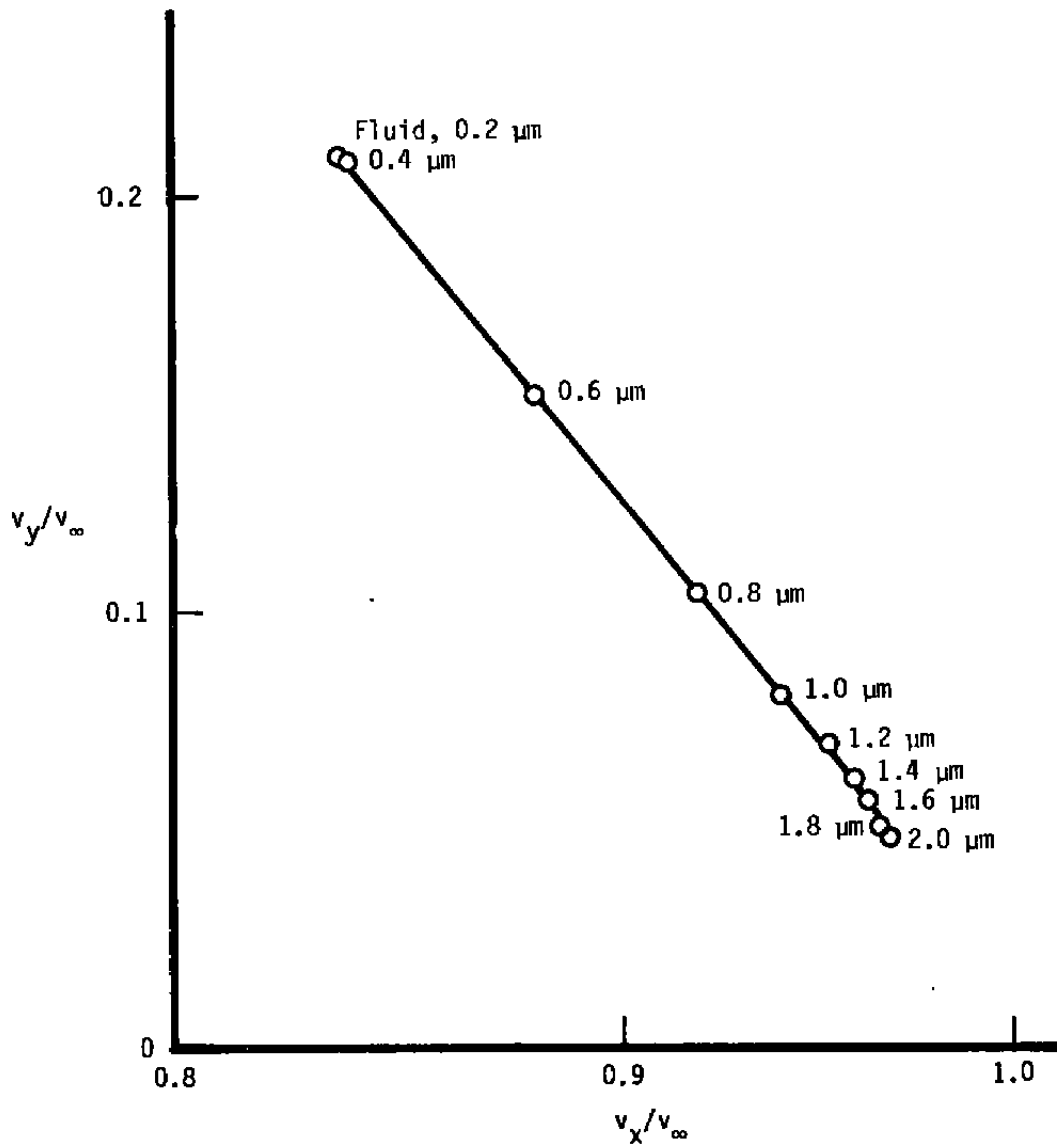


a. $x_M = 0.015 \text{ mm}$

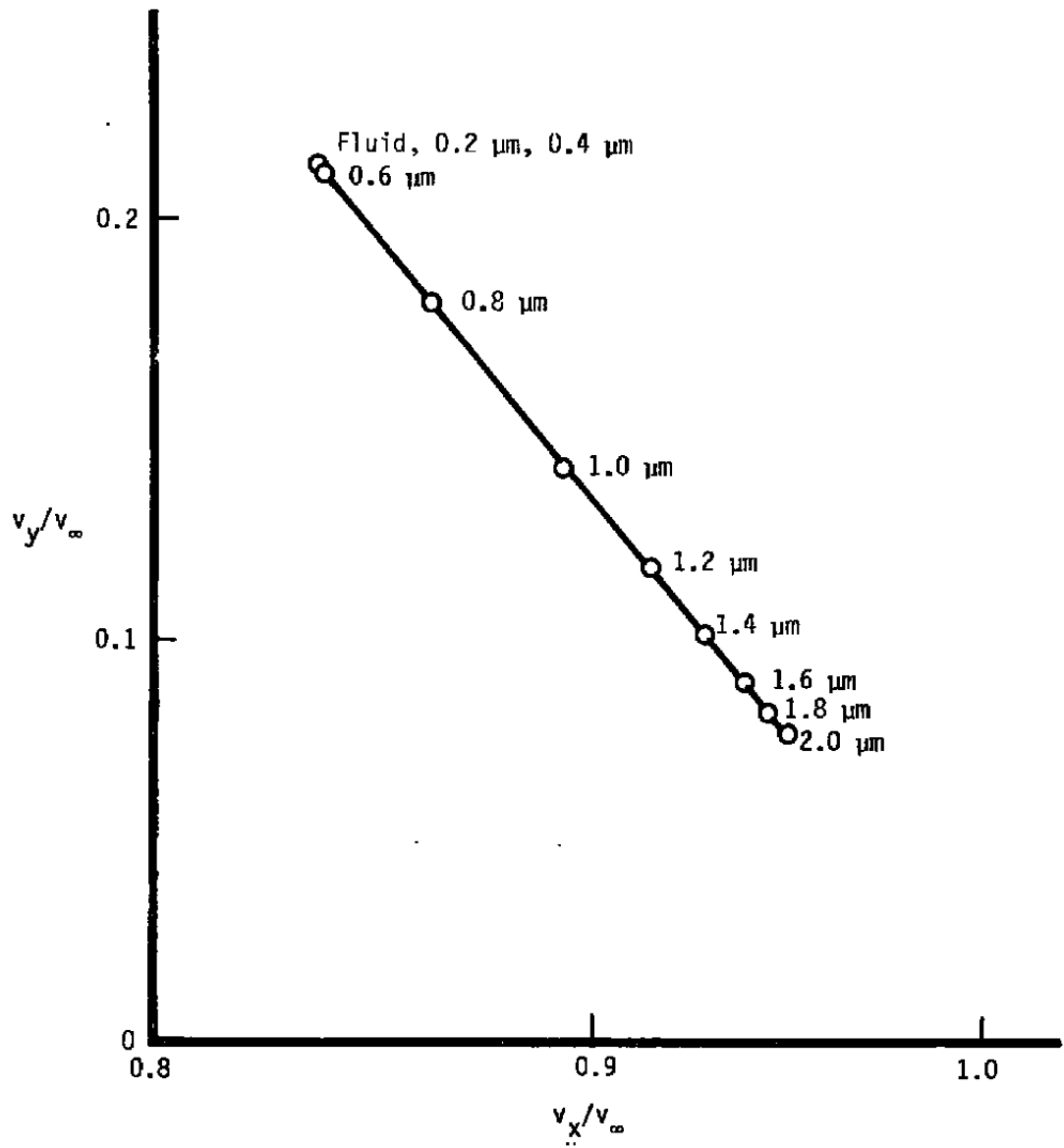
Figure 16. Particle response to an oblique shock for $M_1 = 2.2$, $\theta = 40 \text{ deg}$, $\delta = 14 \text{ deg}$, and $Re = 4.4 \times 10^6/M$.



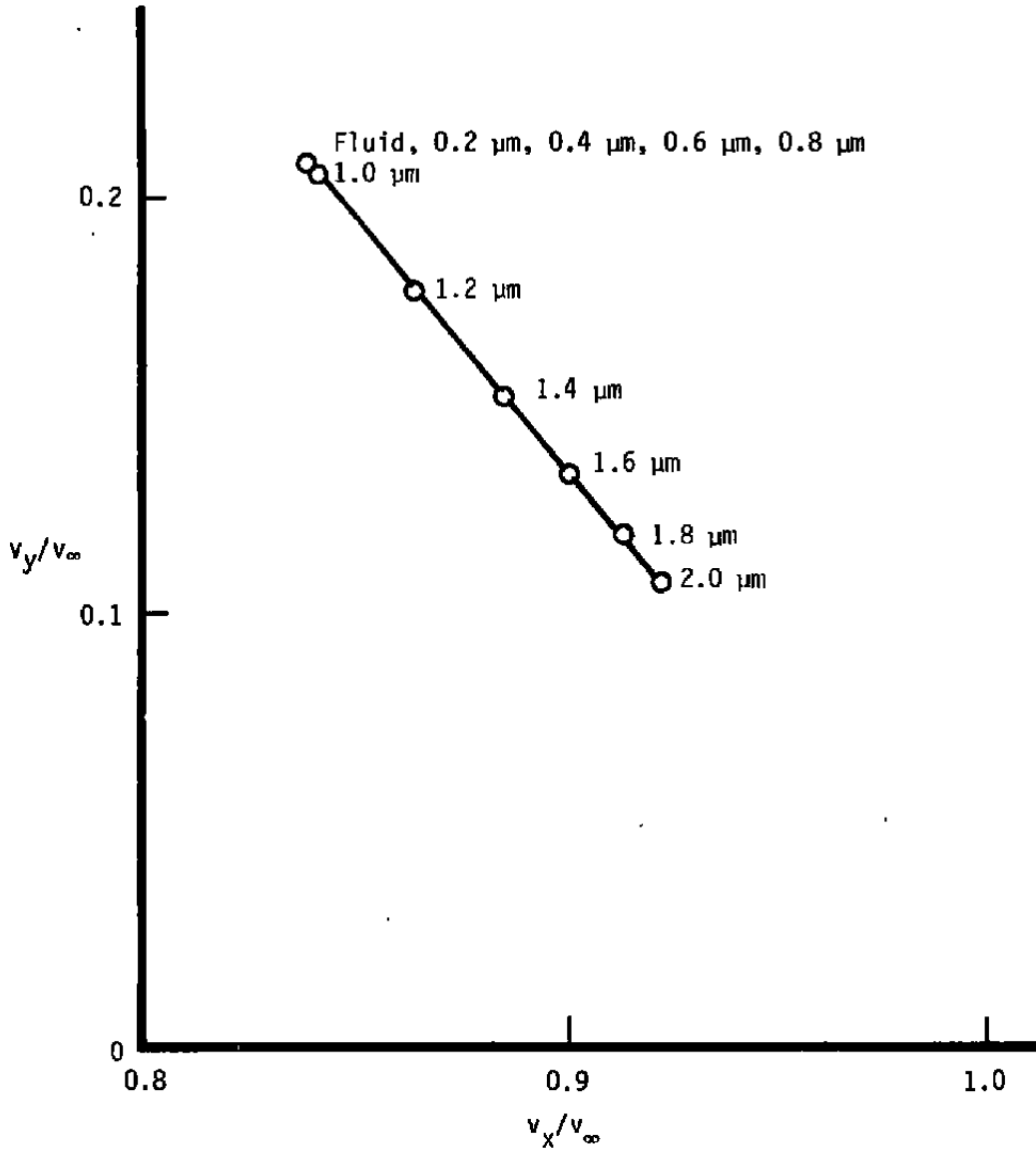
b. $x_M = 0.03 \text{ mm}$
Figure 16. Continued.



c. $x_M = 0.076 \text{ mm}$
Figure 16. Continued.



d. $x_M = 0.15$ mm
Figure 16. Continued.



e. $x_M = 0.3 \text{ mm}$
Figure 16. Concluded.

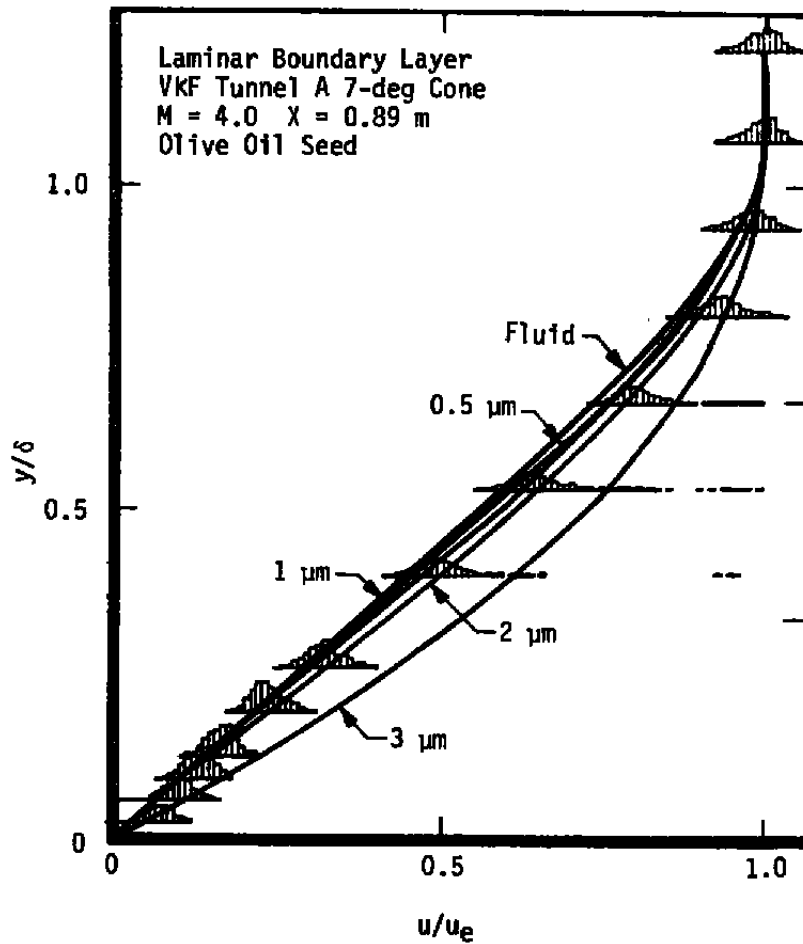
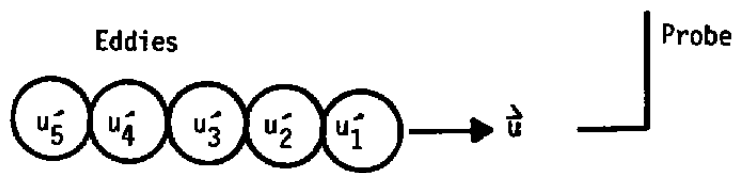


Figure 17. Calculated particle velocities and measured LV velocity distributions in the laminar boundary layer on a 7-deg half-angle cone at M = 4.

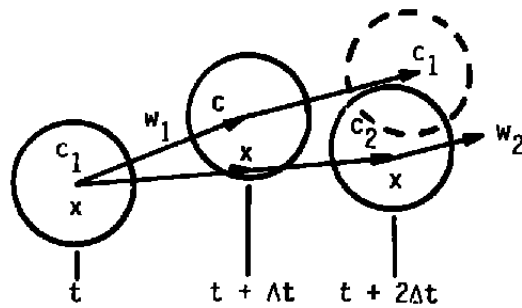


a. ID depiction of turbulence

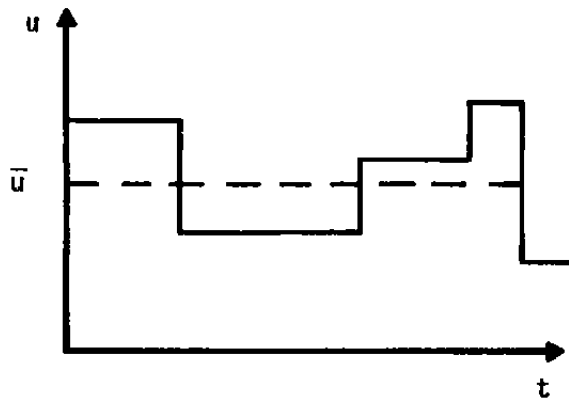


b. Turbulent velocity as seen by a probe

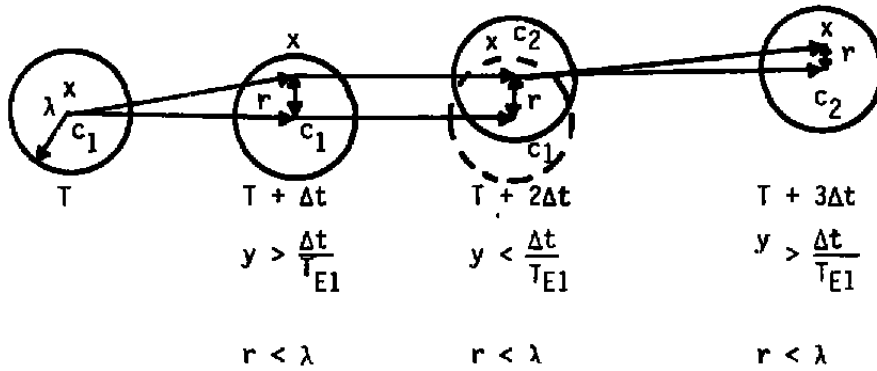
Figure 18. Eulerian representation of turbulence.



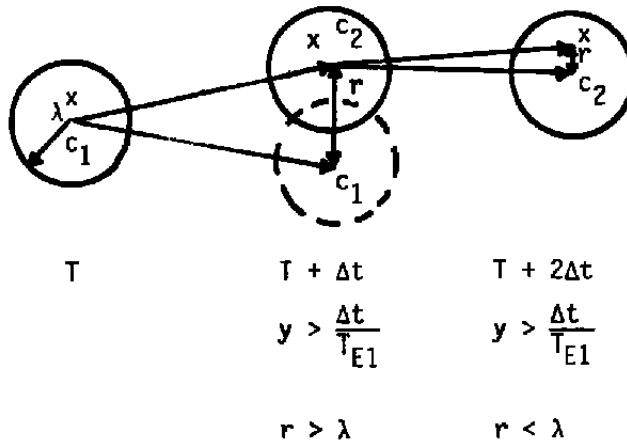
a. Turbulent field as seen by a small particle



b. Turbulent fluid velocity as seen by a small particle
Figure 19. Lagrangian turbulence representation.



a. Time scale effects



b. Length scale effects

Figure 20. Particle interaction with a turbulent eddy - effects of time and length scales.

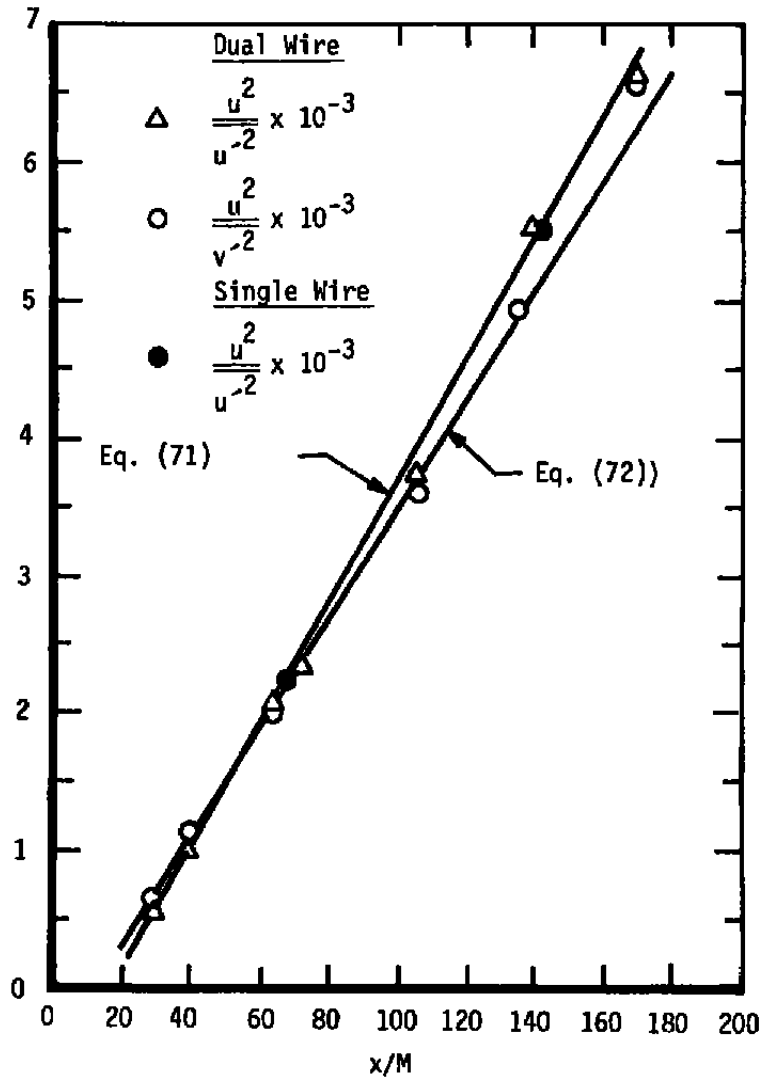


Figure 21. Hot-wire measurements of turbulent energy decay for the experiment of Snyder and Lumley (Ref. 25).

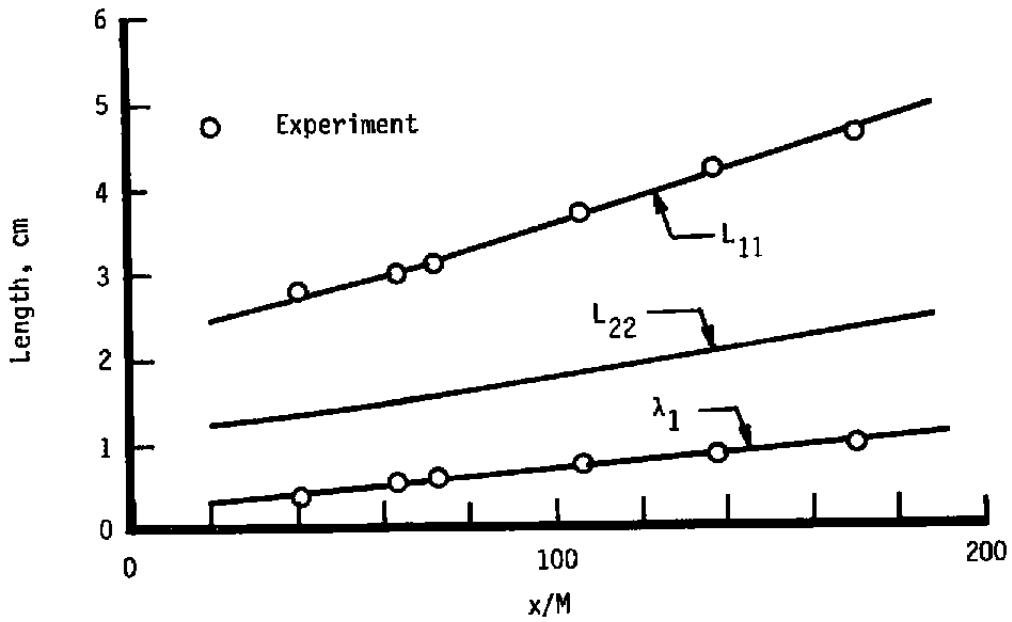


Figure 22. Length scales for the experiment of Snyder and Lumley (Ref. 25).

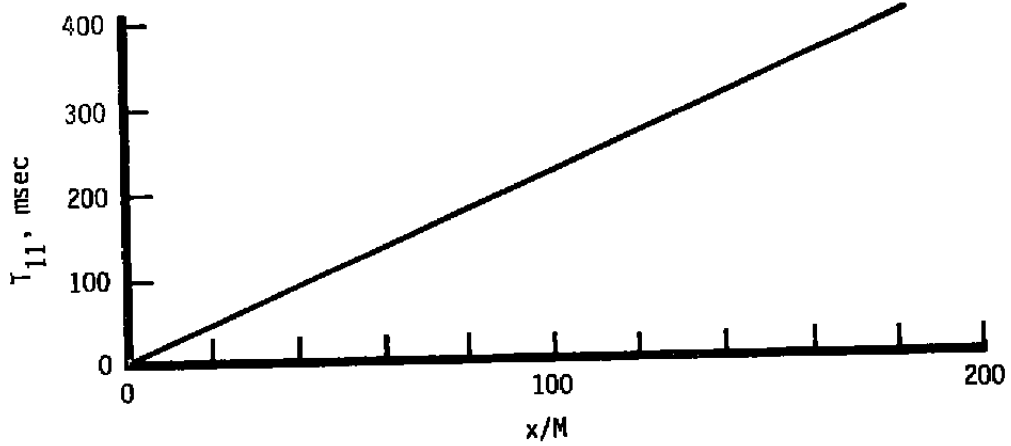


Figure 23. Assumed Lagrangian integral time scale for the experiment of Snyder and Lumley (Ref. 25).

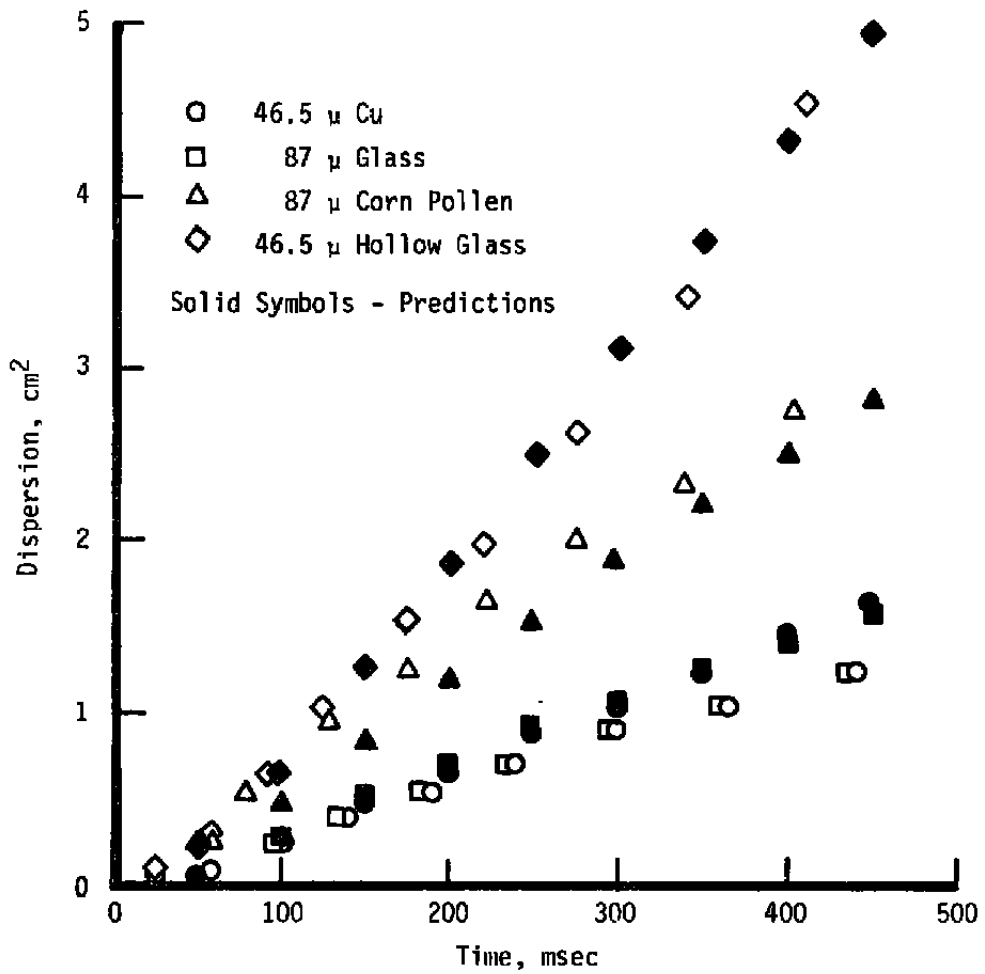


Figure 24. Experimental and predicted particle dispersion for the experiment of Snyder and Lumley (Ref. 25).

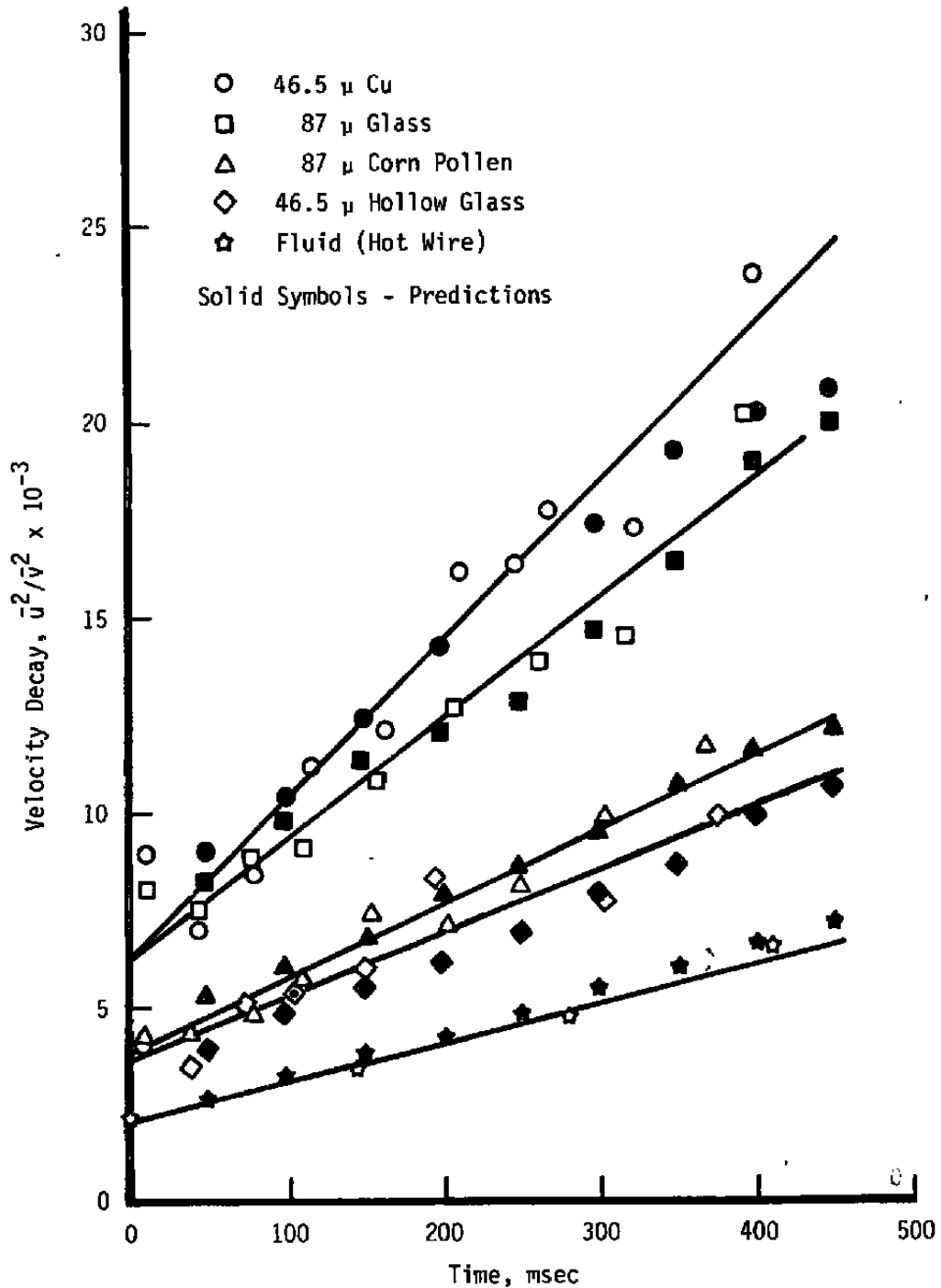


Figure 25. Experimental and predicted particle turbulent velocity decay for the experiment of Snyder and Lumley (Ref. 25).

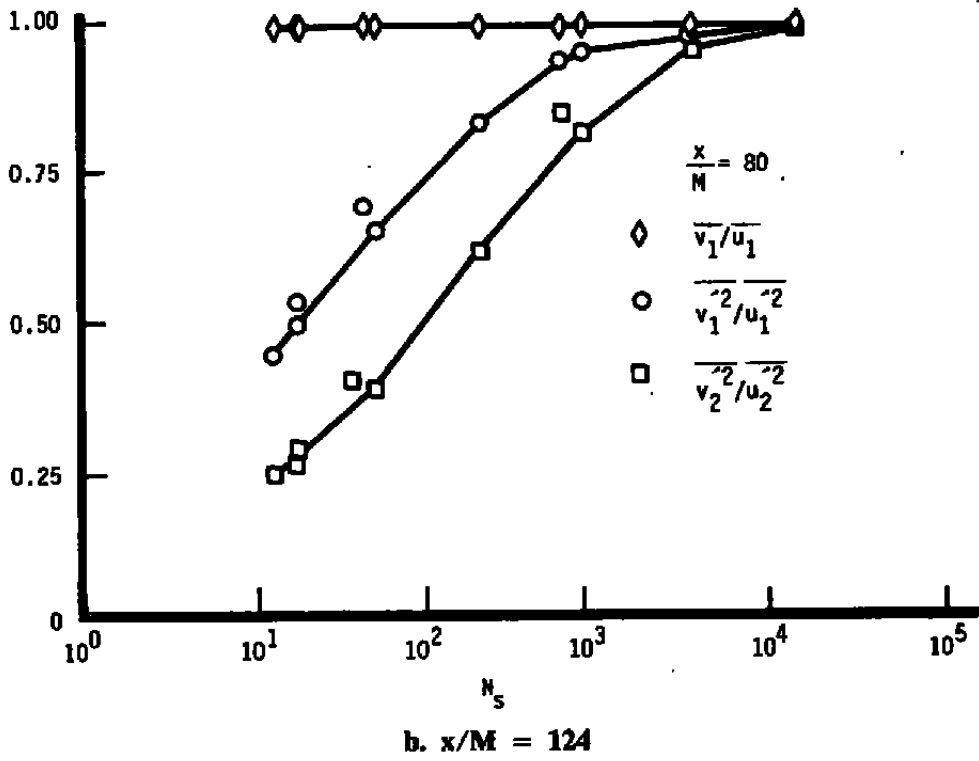
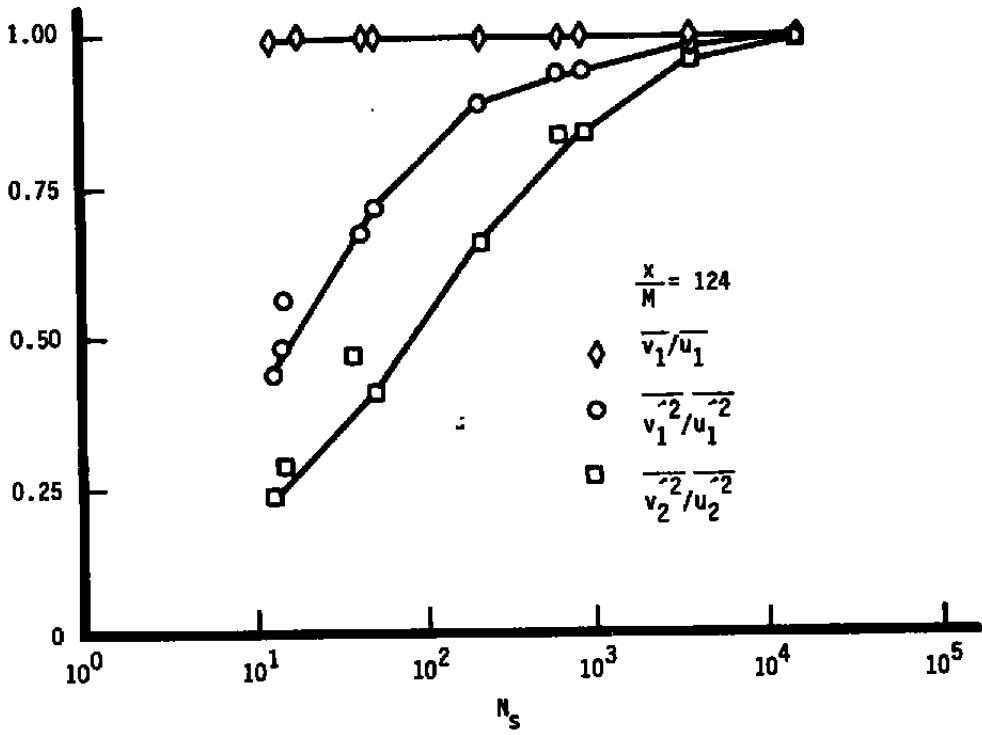


Figure 26. Predicted particle response to grid-generated turbulence.

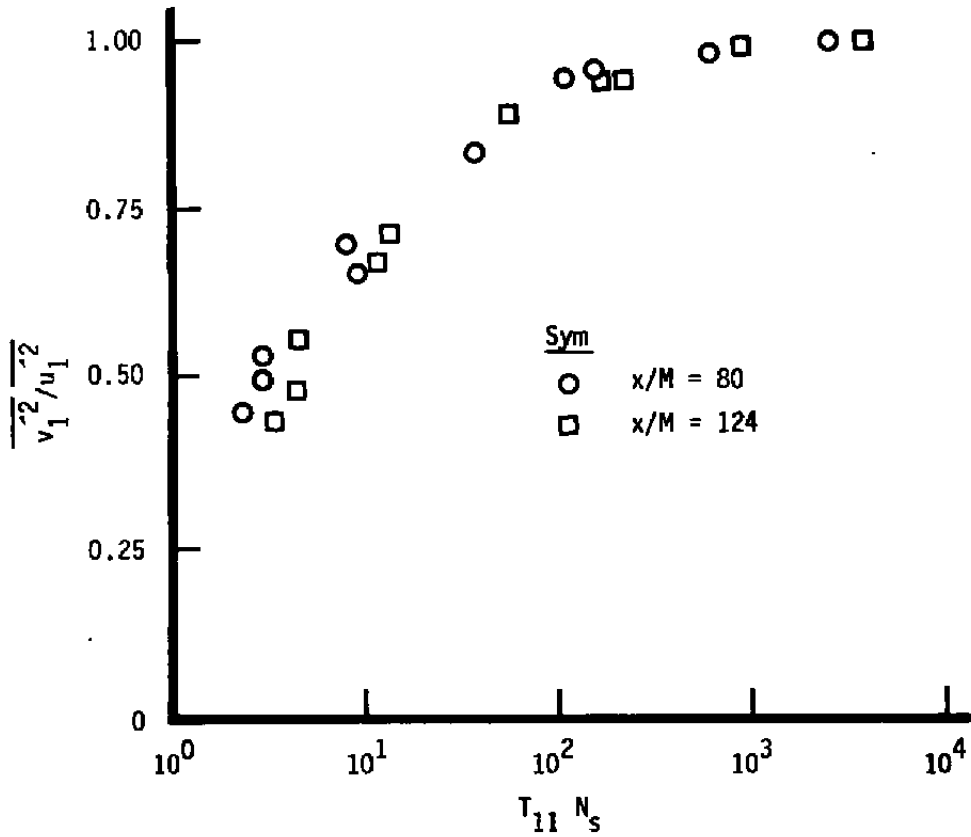
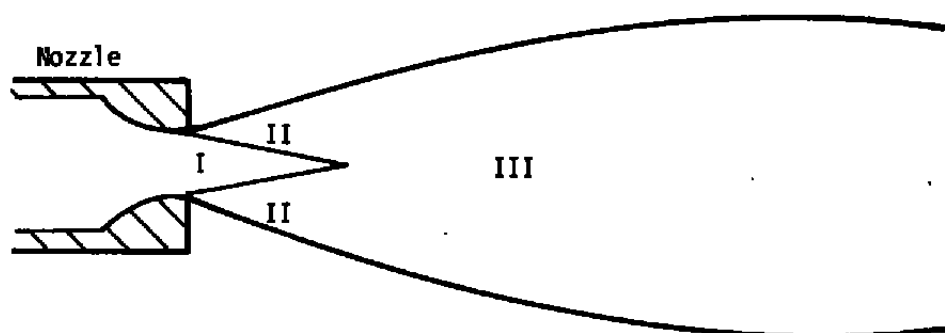


Figure 27. Product of the Stokes number and the turbulence time scale for grid-generated turbulence for x/M of 80 and 124.



Region
I Potential Core
II Mixing Layer
III Main Region

Figure 28. Flow structure for a simple subsonic jet.

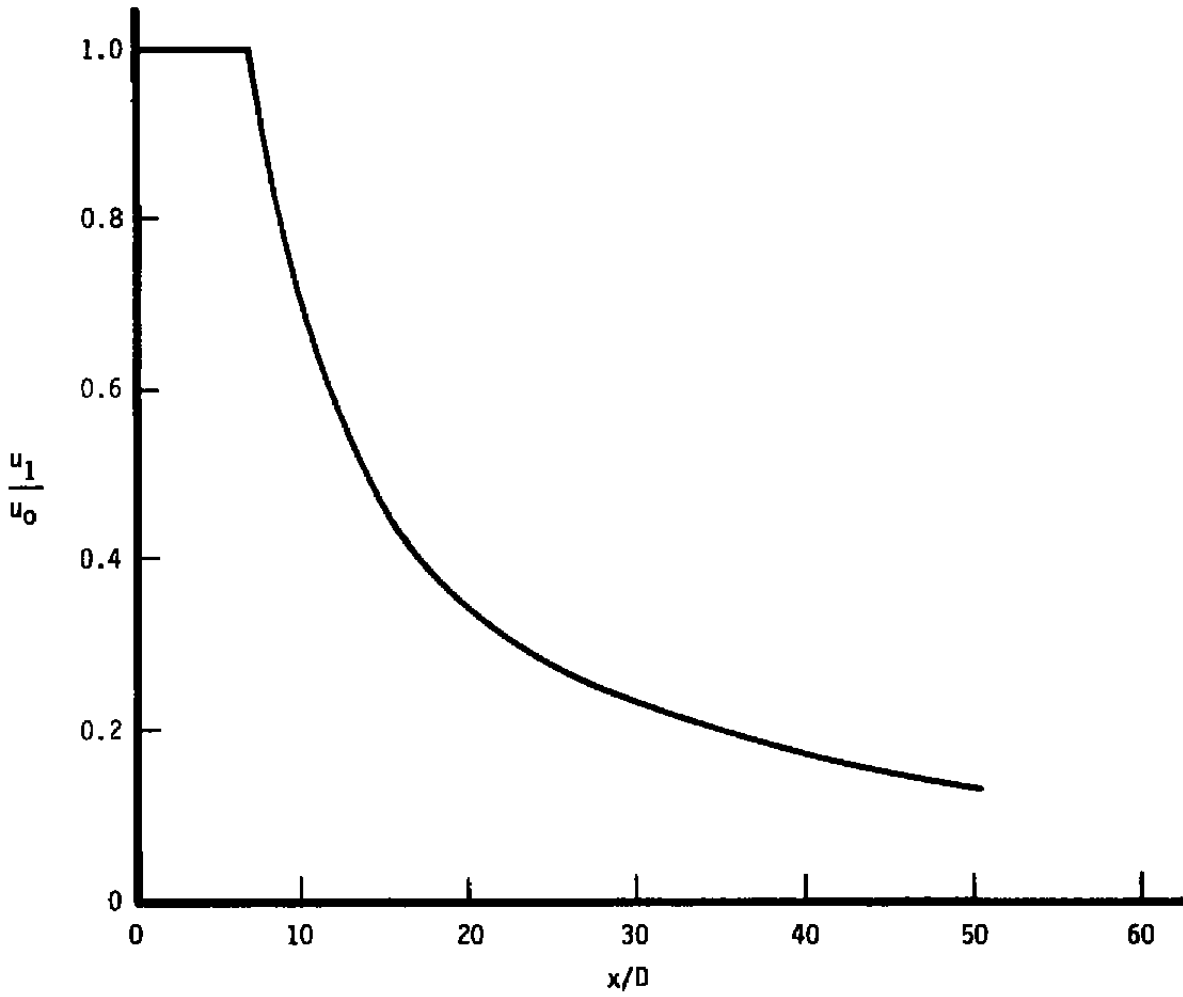
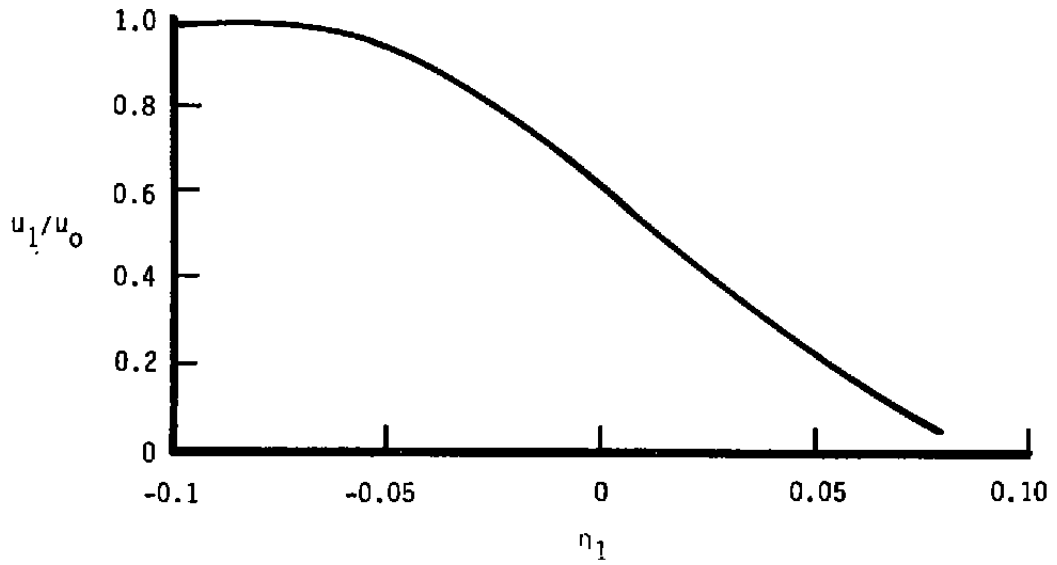
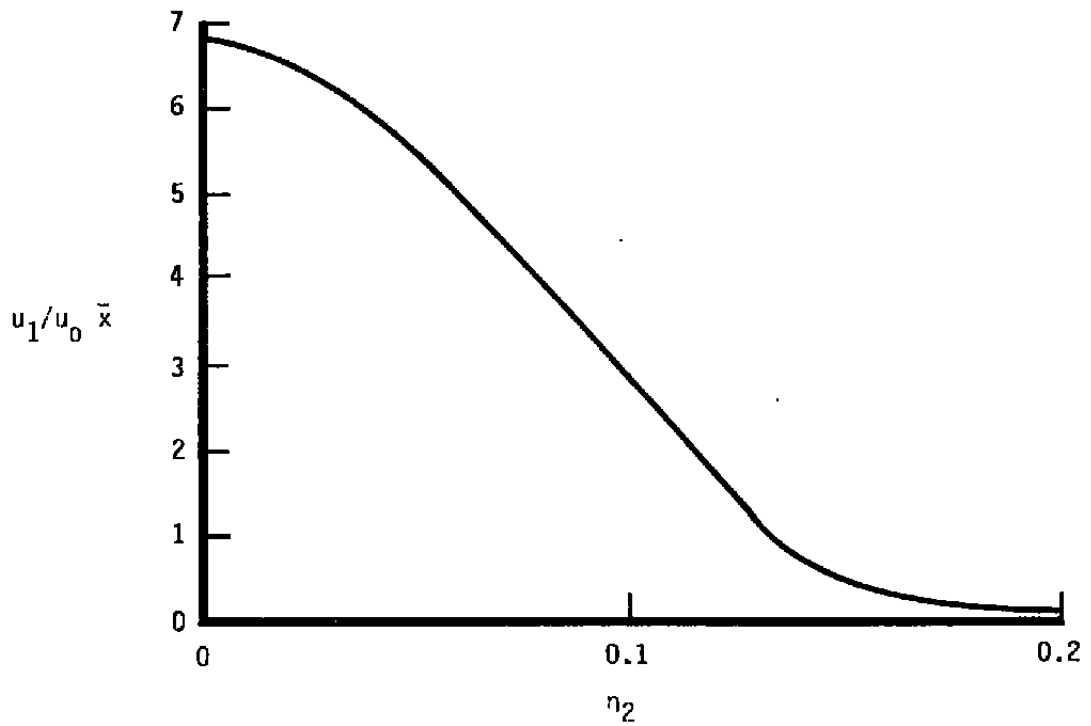


Figure 29. Decay of centerline axial velocity for a subsonic jet.

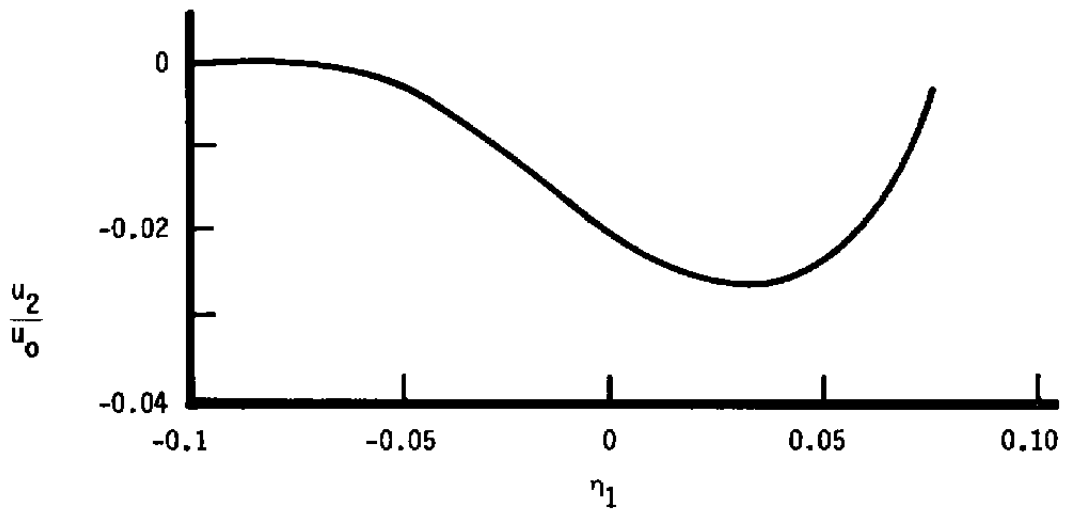


a. Mixing region

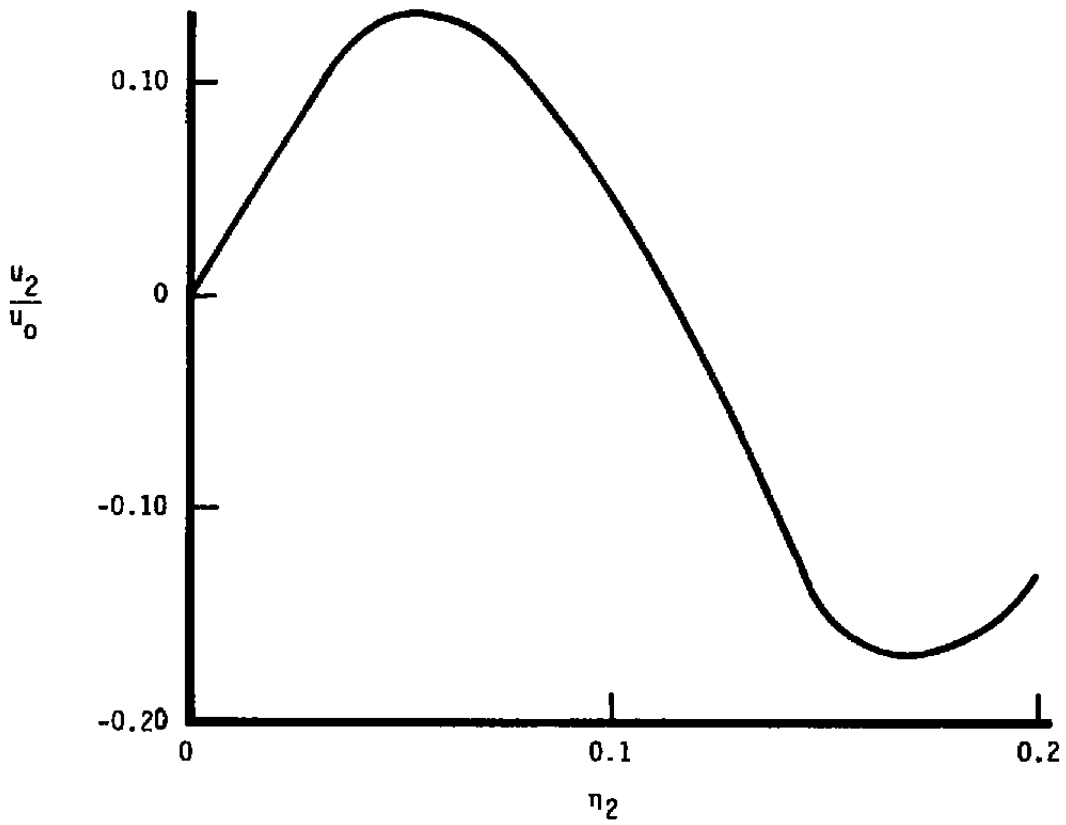


b. Main region

Figure 30. Radial distribution of axial velocity.

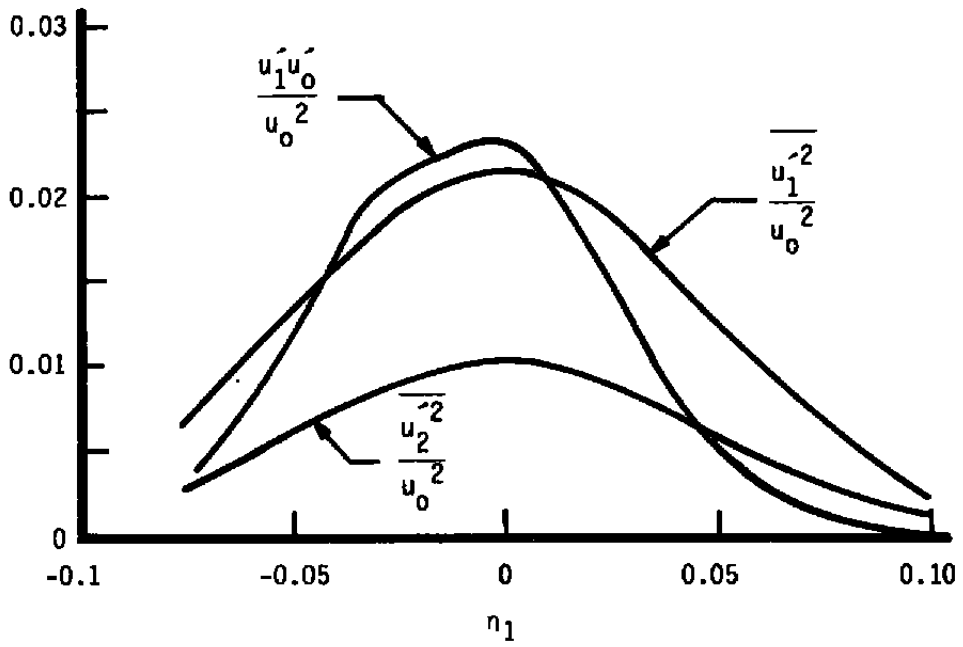


a. Mixing region

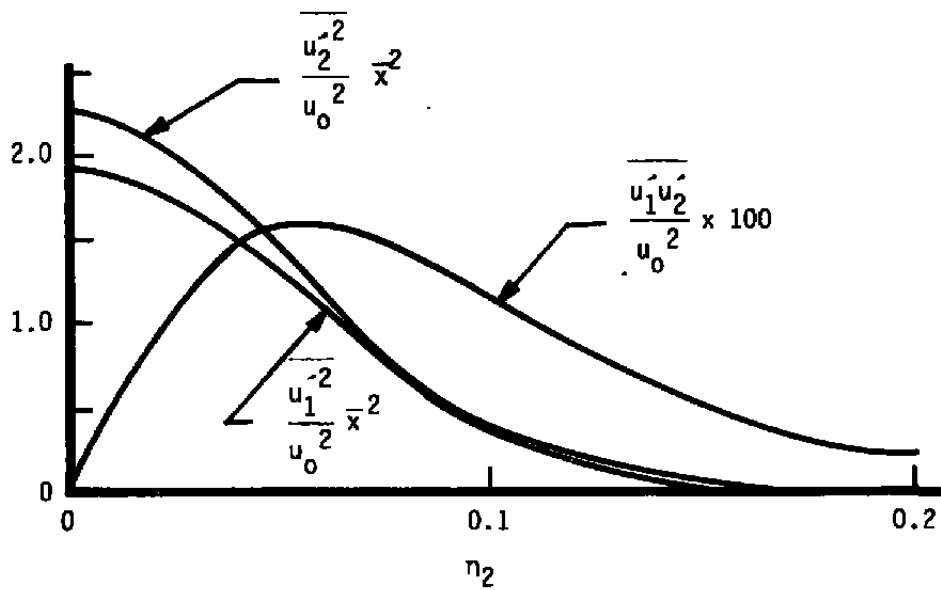


b. Main region

Figure 31. Radial distribution of radial velocity.



a. Mixing region



b. Main region

Figure 32. Radial distribution of turbulent stresses.

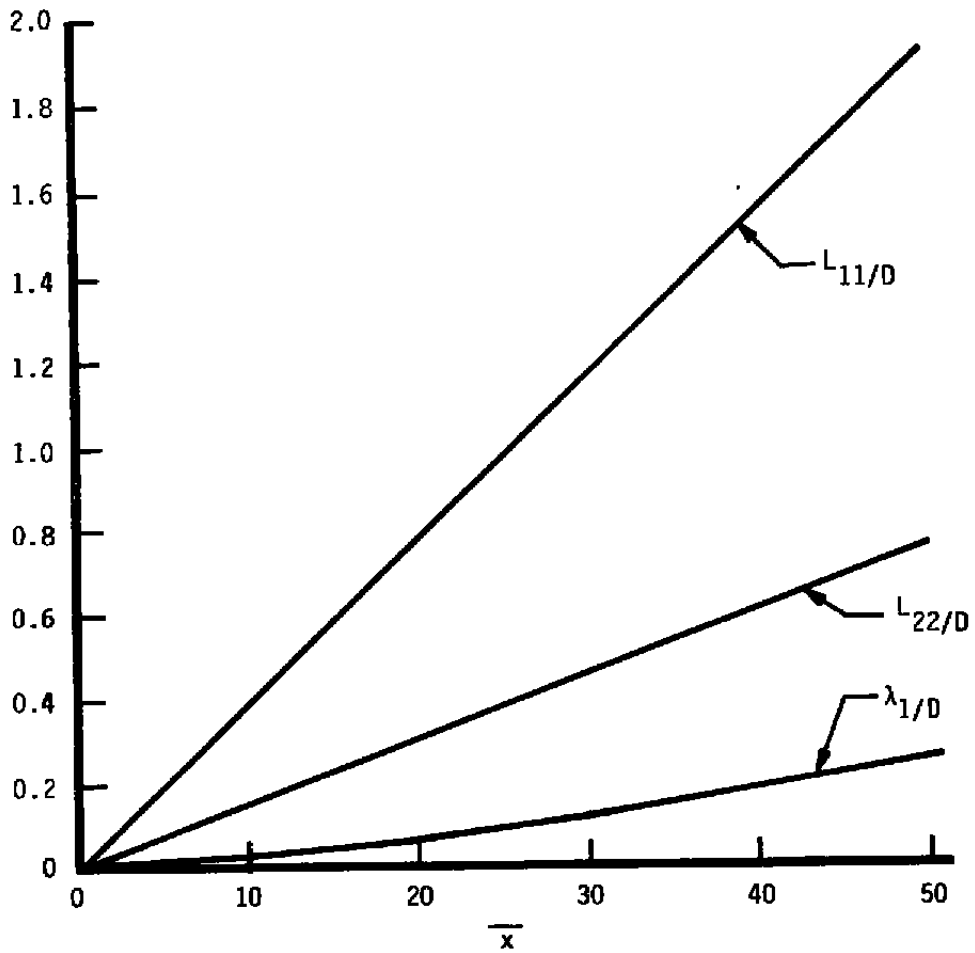


Figure 33. Centerline distribution of jet turbulence length scales.

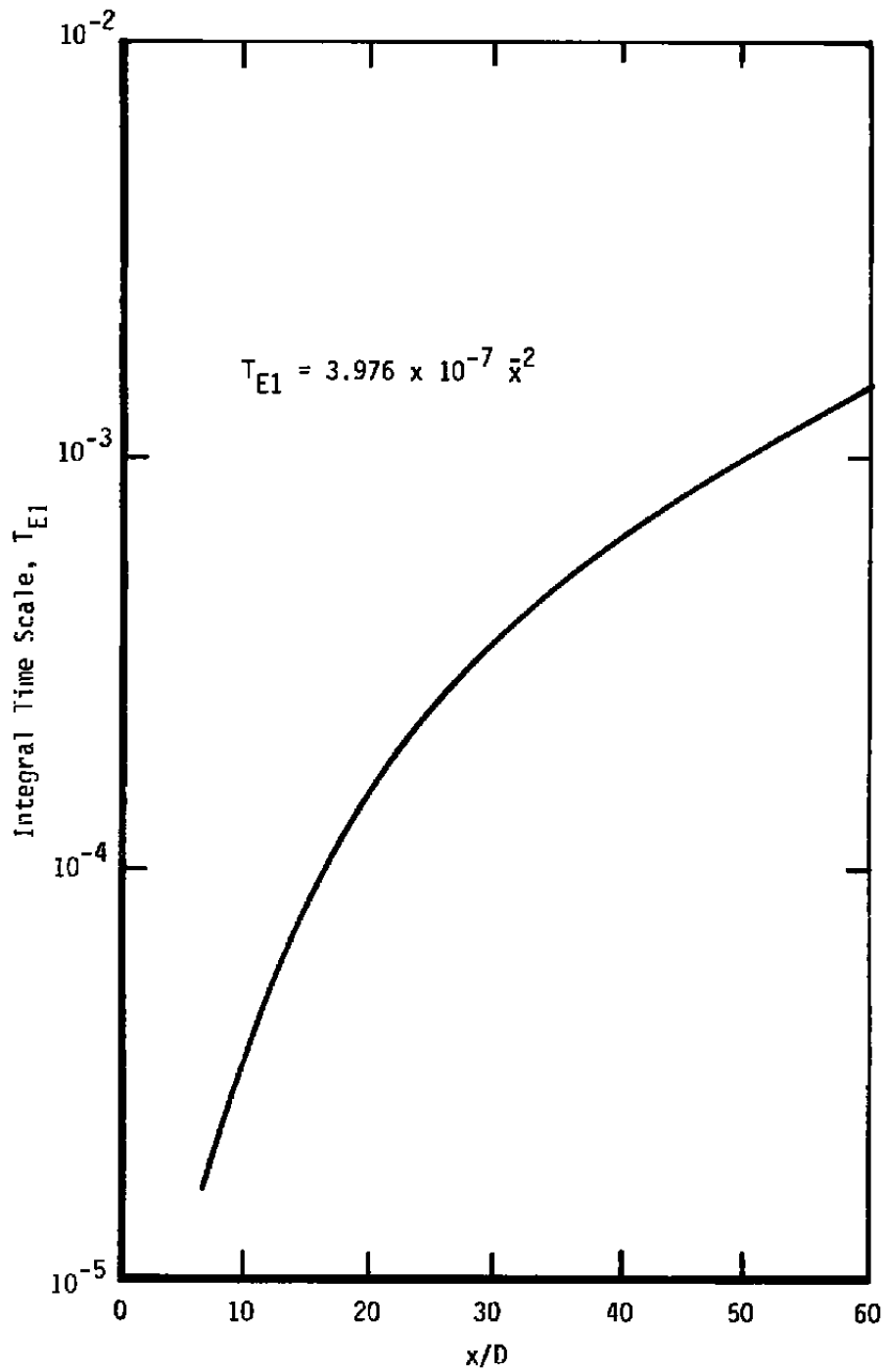


Figure 34. Centerline distribution of jet turbulence integral time scale.

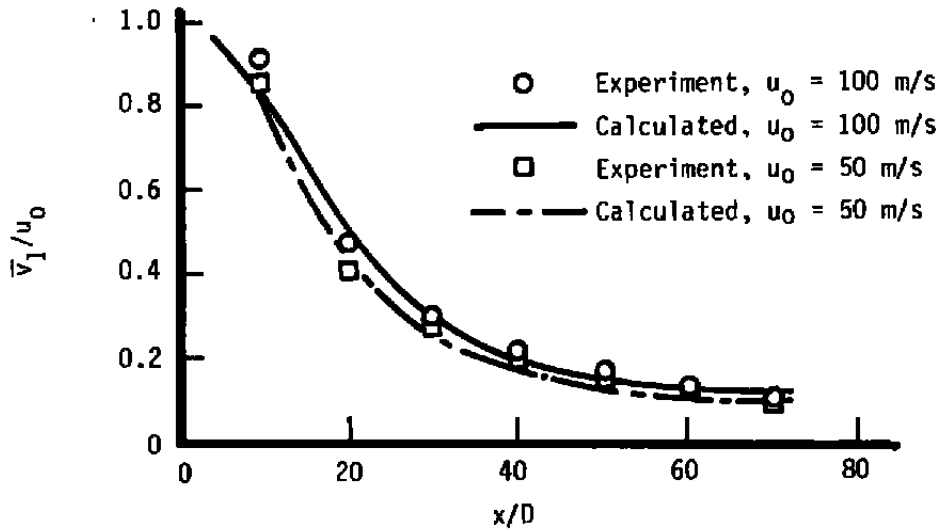


Figure 35. Measured and predicted particle velocities on the jet centerline for 20- μ m fly-ash particles.

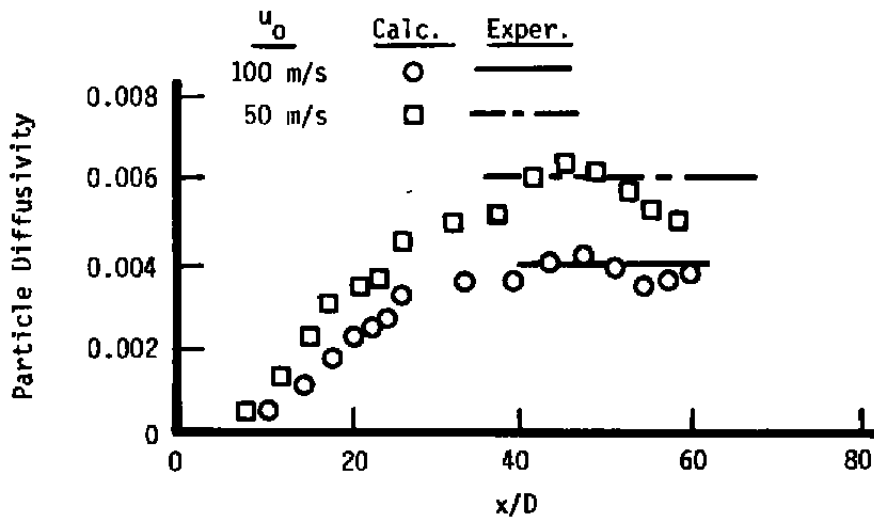
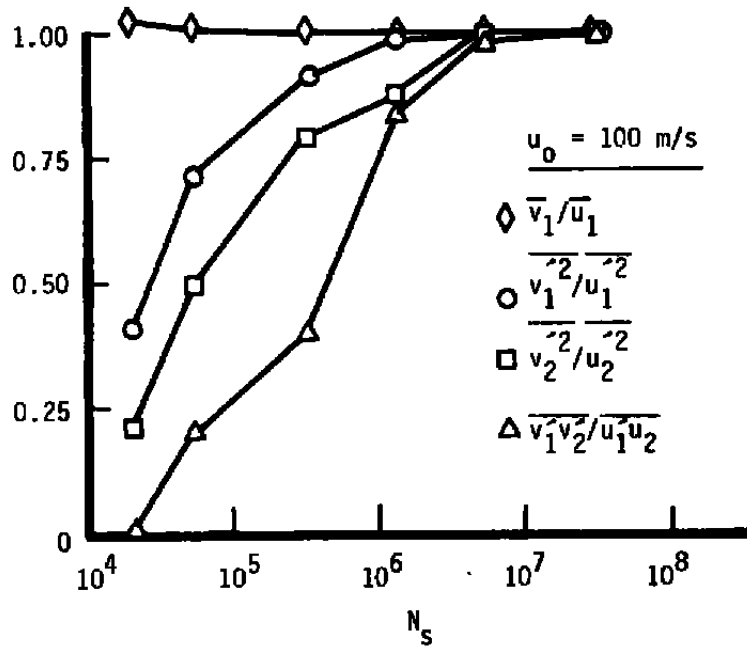
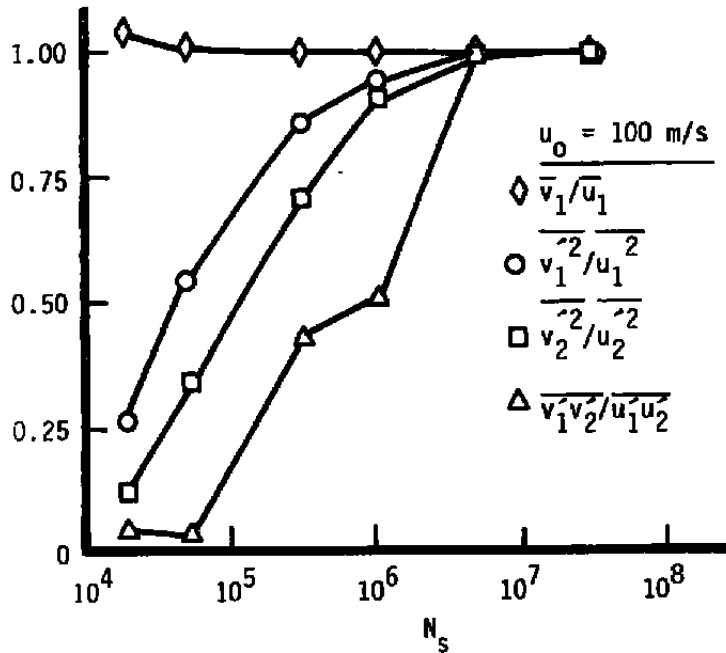


Figure 36. Measured and predicted particle diffusivity on the jet centerline for 20- μ m fly-ash particles



a. $x/D = 12, r/D = 0.38$



b. $x/D = 8.57, r/D = 0.34$

Figure 37. Predicted particle response to turbulence in a subsonic axisymmetric jet.

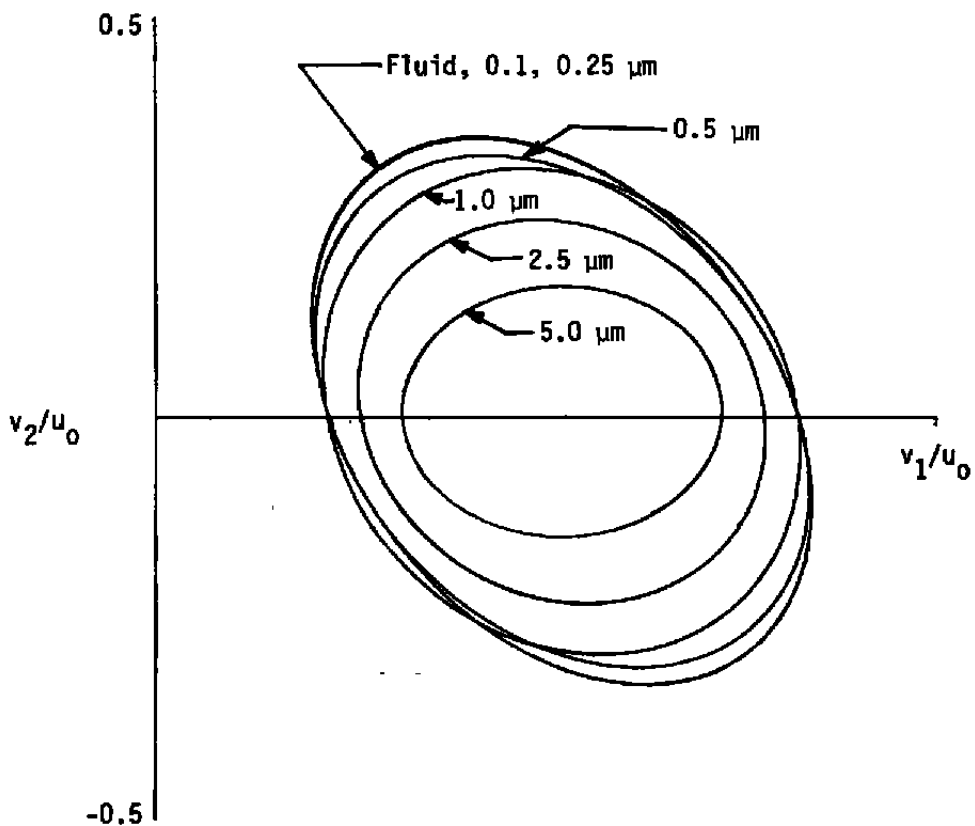


Figure 38. Velocity correlograms for water particles in a subsonic axisymmetric jet at $x/D = 12.0$, $r/D = 0.375$.

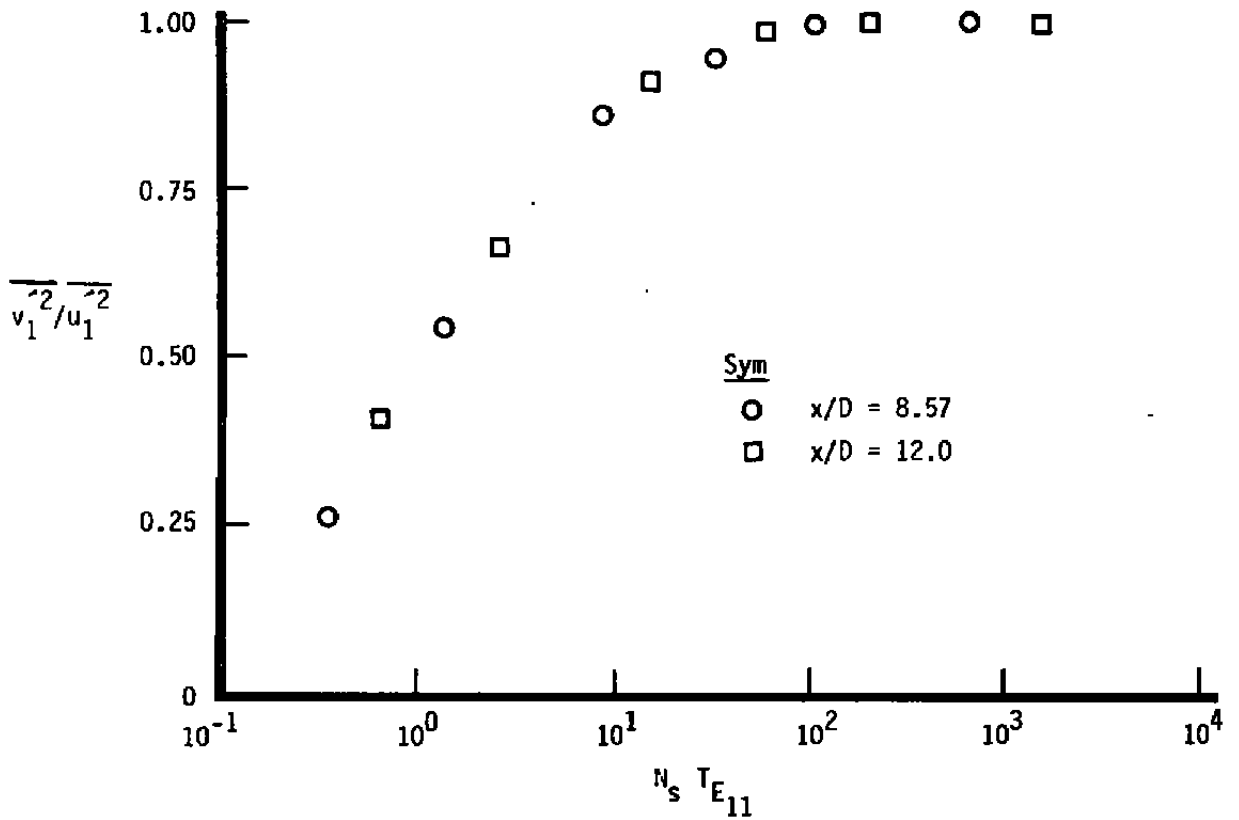
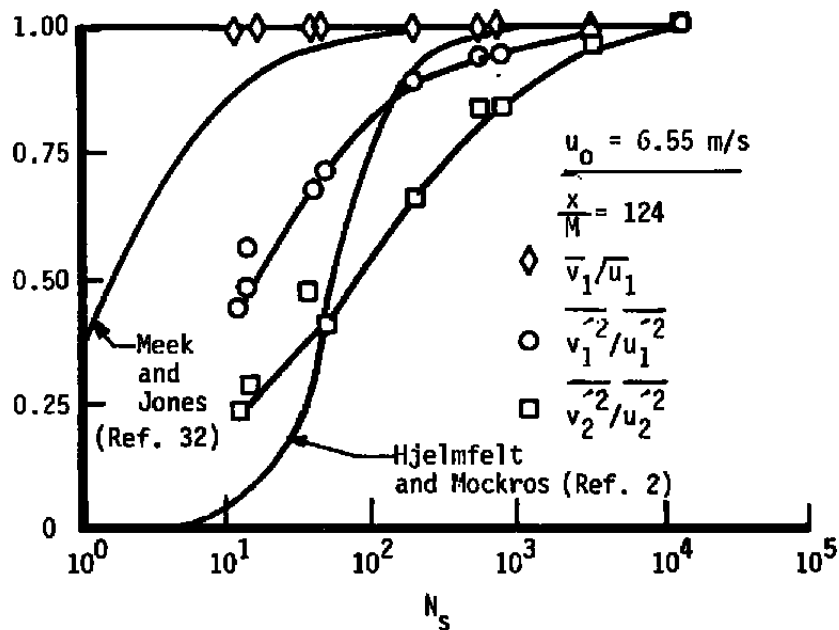
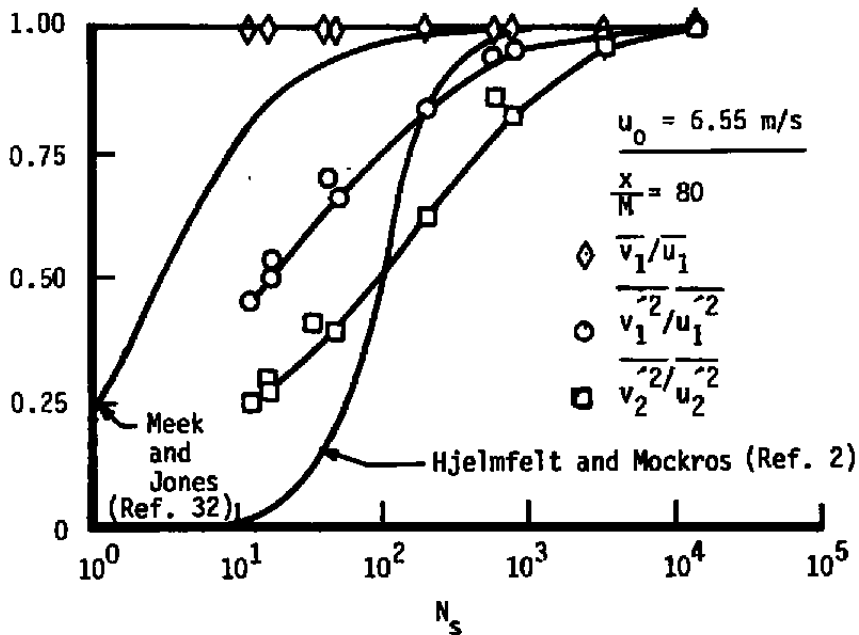


Figure 39. Product of the Stokes number and the turbulence time scale for a subsonic axisymmetric jet for x/D of 8.57 and 12.0.

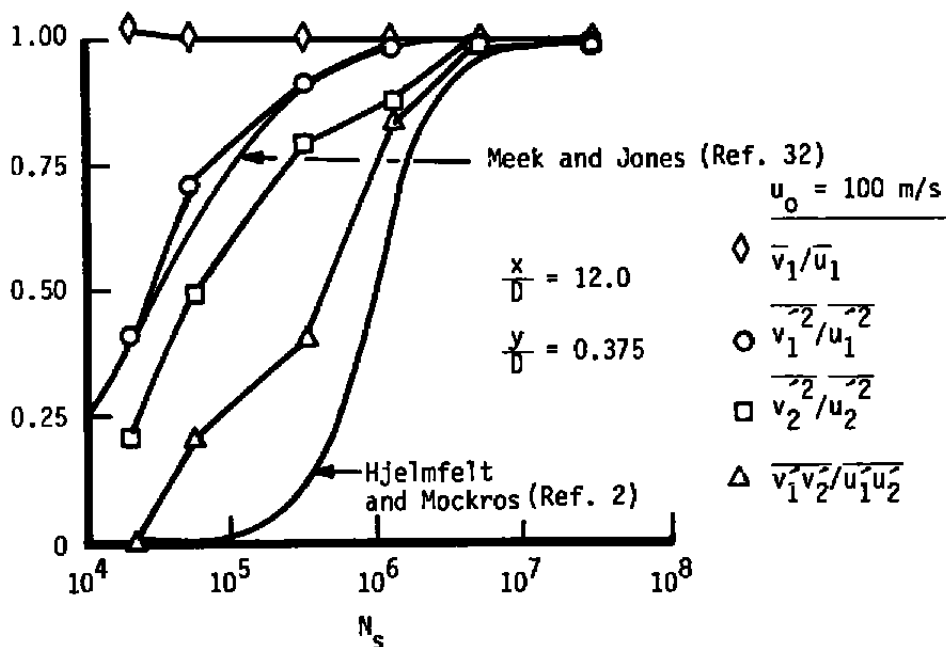


a. $x/M = 124$

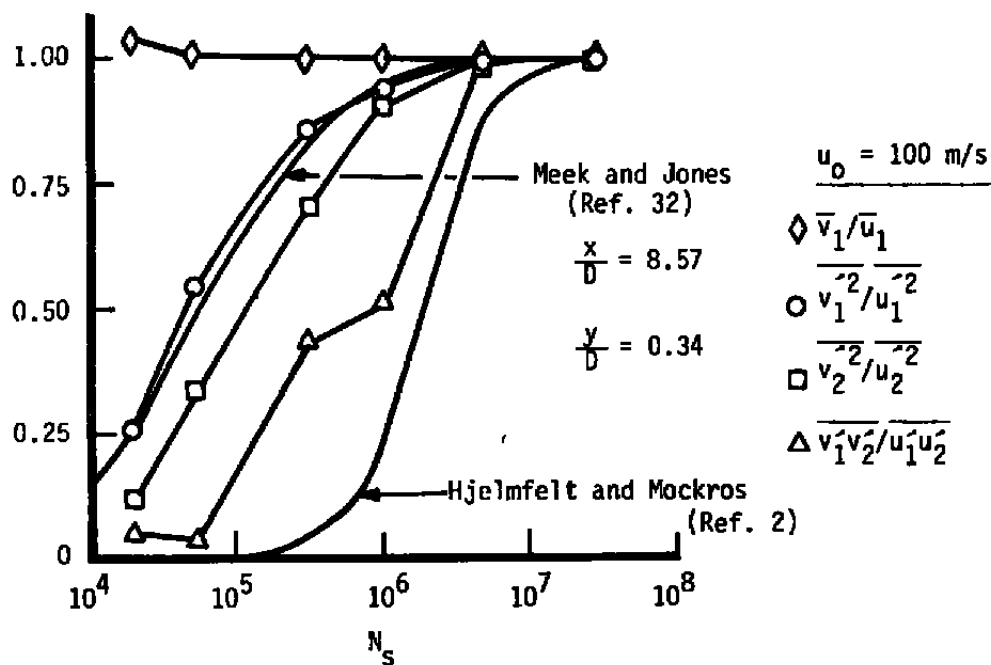


b. $x/M = 80$

Figure 40. Approximations and theoretical particle response for grid-generated turbulence.



a. $x/D = 12.0, r/D = 0.375$



b. $x/D = 8.57, r/D = 0.34$

Figure 41. Approximations and theoretical particle response for a subsonic jet.

Table 1. Particle Characteristics for the Experiment of Snyder and Lumley (Ref. 25)

Particle	Diameter, m	Density, g/cc	Stokes No.
Hollow Glass	46.5 ± 3.5	0.26	579.0
Solid Glass	87.0 ± 5.0	2.50	17.24
Corn Pollen	87.0 ± 5.0	1.00	43.08
Copper	46.5 ± 3.5	8.90	16.95

NOMENCLATURE

A	Coefficient in Eq. (34)
A_n	Particle acceleration number
A_p	Particle surface area
B	Coefficient in Eq. (34)
C_d	Particle drag coefficient
C_{do}	Stokes drag coefficient
C_{ij}	Coefficients defined in Eq. (67)
D	Jet diameter
d	Particle diameter
F₁	Inertia correction for Stokes drag
F₂	Compressibility correction for Stokes drag
F₃	Rarefaction correction for Stokes drag
F₄	Shape correction for Stokes drag
F_L	Particle lift force
f₁	Defined by Eqs. (15), (19), (23)
f₂	Defined by Eqs. (16), (20), (24)
G	Defined by Eq. (40)
g	Gravitational acceleration
h	Defined by Eq. (41)

J	Jacobian
K	Defined by Eq. (9)
$K\pi$	Particle Knudsen number
L_{i1}	Turbulence integral length scale
L_m	Defined by Eq. (93)
ℓ	Prandtl's mixing length
M_R	Particle relative Mach number
m	Grid mesh spacing
m_f	Displaced fluid particle mass
m_p	Particle mass
N_f	Stokes frequency number
N_s	Stokes number
Re_2	Particle relative Reynolds number evaluated with conditions behind a normal shock
Re_R	Particle relative Reynolds number
R_{zi}	Random variate
r	Radial direction
\tilde{r}	r/D
S	Density ratio, ρ_p/ρ_f
T	Temperature
T_{E1}	Turbulence integral time scale

t	Time
u	Fluid velocity
U	$\sum_i \overline{u_i' u_i'}$
v	Particle velocity
x_p	Particle volume
w	Particle relative velocity
x	Axial direction
x_i	Spatial coordinate
\bar{x}	x/D
x_m	Distance normal to oblique shock
$\bar{Y}(t)$	Particle position at time t
α	Defined by Eq. (10)
β	Defined by Eq. (11)
γ	Ratio of specific heats
Δ_H	Basset term correction coefficient
ϵ	Turbulent dissipation
ϵ_{pr}	Particle diffusivity
η	Kolmogorov length scale
η_1	$(\bar{r}-0.5)/\bar{x}$
η_2	\bar{r}/\bar{x}
θ	Defined by Eq. (53)

λ	Taylor microscale
μ	Absolute viscosity
ν	Kinematic viscosity
ϵ_{11}	Defined by Eq. (14)
ρ_f	Fluid density
ρ_p	Particle density
τ	Time
ϕ	Defined by Eq. (14)
ψ	Particle shape parameter
ω	Defined by Eq. (8)

Subscripts

i	Spatial location
c	Fluid particle location
f	Fluid
p	Particle
x	Particle position
o	Reference condition

Superscript

i	Iteration number
-----	------------------